DEUTSCHES ELEKTRONEN – SYNCHROTRON DESY

DESY 87-064
July 1987


# ON THE THEORETICAL UNDERSTANDING AND CALCULATION OF SAMPLING CALORIMETERS

by

H. Brückmann, B. Anders, U. Behrens,
P. Cloth, D. Filges

*I. Institut f. Experimentalphysik, Universität Hamburg*
*Deutsches Elektronen-Synchrotron DESY, Hamburg*
*Kernforschungsanlage Jülich GmbH, Jülich*

ISSN 0418-9833

NOTKESTRASSE 85 · 2 HAMBURG 52

To be sure that your preprints are promptly included in the
HIGH ENERGY PHYSICS INDEX,
send them to the following address (if possible by air mail):

**DESY**
**Bibliothek**
**Notkestrasse 85**
**2 Hamburg 52**
**Germany**

DESY 87-064
July 1987

ISSN 0418-9833

# ON THE THEORETICAL UNDERSTANDING AND CALCULATION OF SAMPLING CALORIMETERS

invited talk presented by

Hanno Brückmann

at the XVIth Winter Meeting on Fundamental Physics, Sevilla, Spain, 23-27 Feb., 1987

Coauthors:

Bernd Anders[+], Ulf Behrens,

Peter Cloth* and Detlev Filges*

I. Institut für Experimentalphysik der Universität Hamburg,

D-2000 Hamburg 50, F.R.G.

(supported by the Bundesministerium für Forschung und Technologie, BMFT, Bonn, F.R.G.)

---

[+] DESY, Hamburg, F.R.G.

* Kernforschungsanlage Jülich GmbH, IRE, Jülich, F.R.G.

## Abstract

The physics in hadron sampling calorimetry covers an energy range from TeV down to eV. High energy physics, medium energy physics, nuclear physics as well as atomic physics are needed to understand the complexity of processes, which govern the energy depositions into absorber and detector layers.

In this paper we give a detailed description of our calculational procedure (including several big sized computer program codes), which we have applied to several depleted uranium/scintillator calorimeter structures, in connection with the development of the ZEUS detector at HERA/DESY. Within this scheme, the mean response to muons, electrons and hadrons can be calculated with non-parameterized methods as well as the hadronic resolution on an event-by-event basis. The predictive power of the method is proofed by comparing calculated results with recently obtained experimental data.

## Introduction

Two multipurpose detectors, H1 and ZEUS, are in preparation to exploit the physics of HERA. Fig. 1 shows a schematic view of the ZEUS detector [1]. The high resolution calorimeter CAL is designed to achieve:

(i) hermeticity for energy measurement over the entire solid angle, excluding only a small region around the beam pipe;

(ii) best achievable energy resolution for hadrons and jets independent of the jet fragmentation;

(iii) signals shorter than the HERA bunch crossing time of 96 nsec;

(iv) good electron hadron separation.

The technical solution for ZEUS is a sampling calorimeter using plates of depleted uranium (DU) as absorber and plastic scintillator, read out via plastic wave length shifter bars, as detector.

In this report we give a complete and detailed overview of the (state-of-the-art) computational methods to achieve non-parameterized predictions for the mean response to muons (I.2), electrons (I.3) and hadrons (I.4). Most of the calculations were done for a particle energy of 10 GeV, for which new experimental results will become available soon. A first comparison for e/h ratios is made in II.1, whereas in II.2 a complete simulation is presented to calculate the energy resolution for 5 GeV hadrons. We restrict ourselves here to DU as absorber material. This is the most challenging calculation, since DU is a multiplying medium with respect to neutron production.

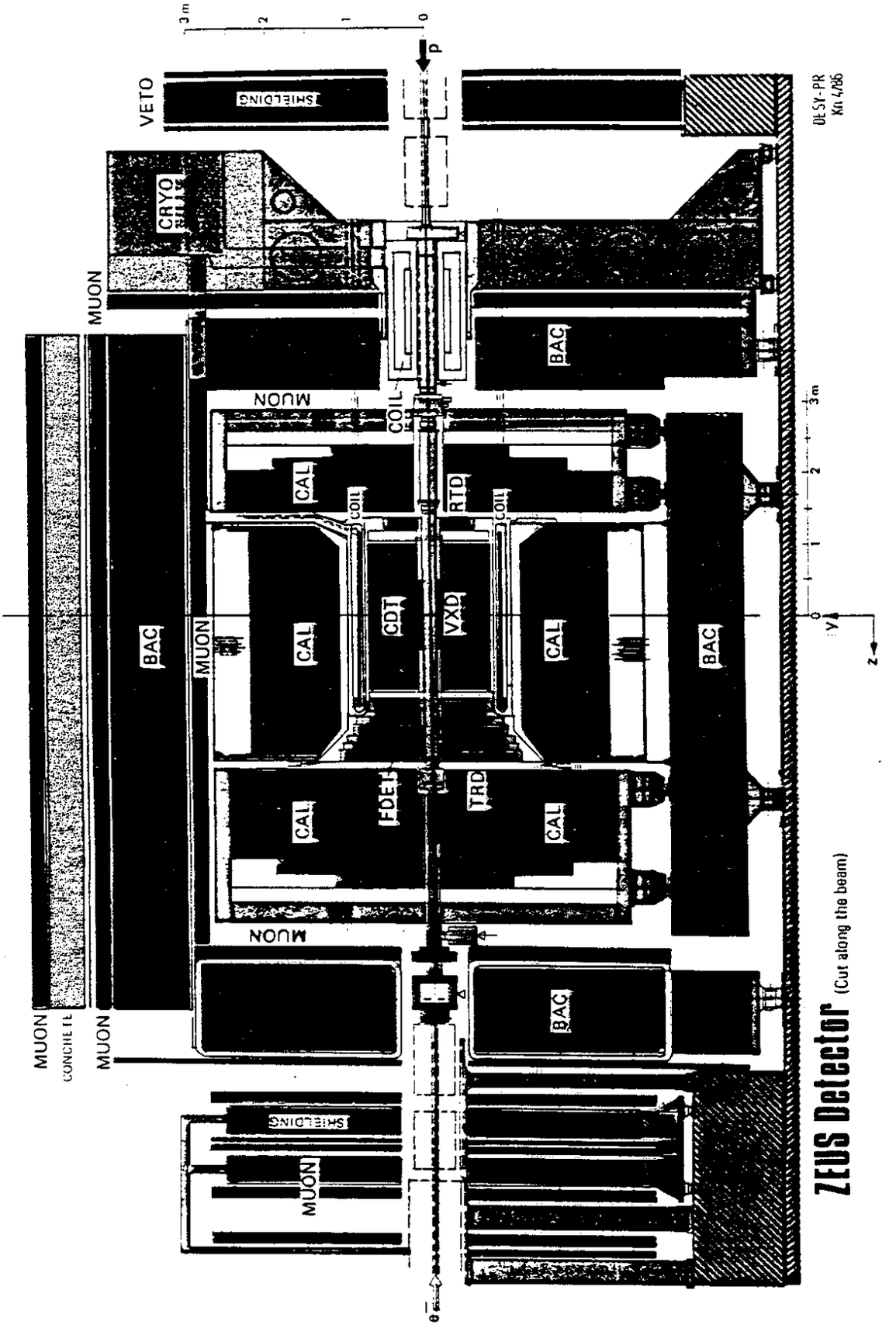


Fig. 1: General layout of the ZEUS detector, cut along the beam.

# I. The Physics of Hadron Sampling Calorimetry (Calculational Methods)

## I.1. The Sampling Procedure

In case of a high energetic hadronic cascade, the incident energy $E_o$ is carried by a variety of particles like $e^{\pm}, \mu^{\pm}, \pi^{\pm}$, $\pi^{\circ}, n, K, p, n$, etc., which deposit different fractions of their energy in the detector layers. How much of the energies released in the detector can actually be read out (made "visible", $E_{vis}$), depends strongly on the detector material (gaseous, liquid or solid) and other parameters such as geometry, saturation, electric and magnetic field vectors.

Some fraction of $E_o$ is completely lost via nuclear binding energy, neutrinos, or by energy leakage due to gaps, dead material in addition to the absorber layers and to the finite size of the calorimeter.

In discussing the performance of (high resolution) hadron sampling calorimeters, it is convenient to define sampling fractions $R_i$ by

$$R_i := \frac{E_{vis,i}}{E_{invis,i} + E_{vis,i}} = \frac{E_{vis,i}}{E_{abs,i}} \qquad (1)$$

where the index i refers to different components in a hadronic shower (see above). $E_{vis,i}$ is the sum of the measured energy in all the detector layers (Fig. 2). $E_{invis,i}$ is the energy deposited in all absorber sheets. If the quantity $E_{abs} = E_{invis} + E_{vis}$ is equal to an incident hadronic energy $E_o$, the calorimeter is called hermetic.

$$\sum \Delta E_{invis} + \sum \Delta E_{vis} = E_{invis} + E_{vis} = E_{absorbed}$$

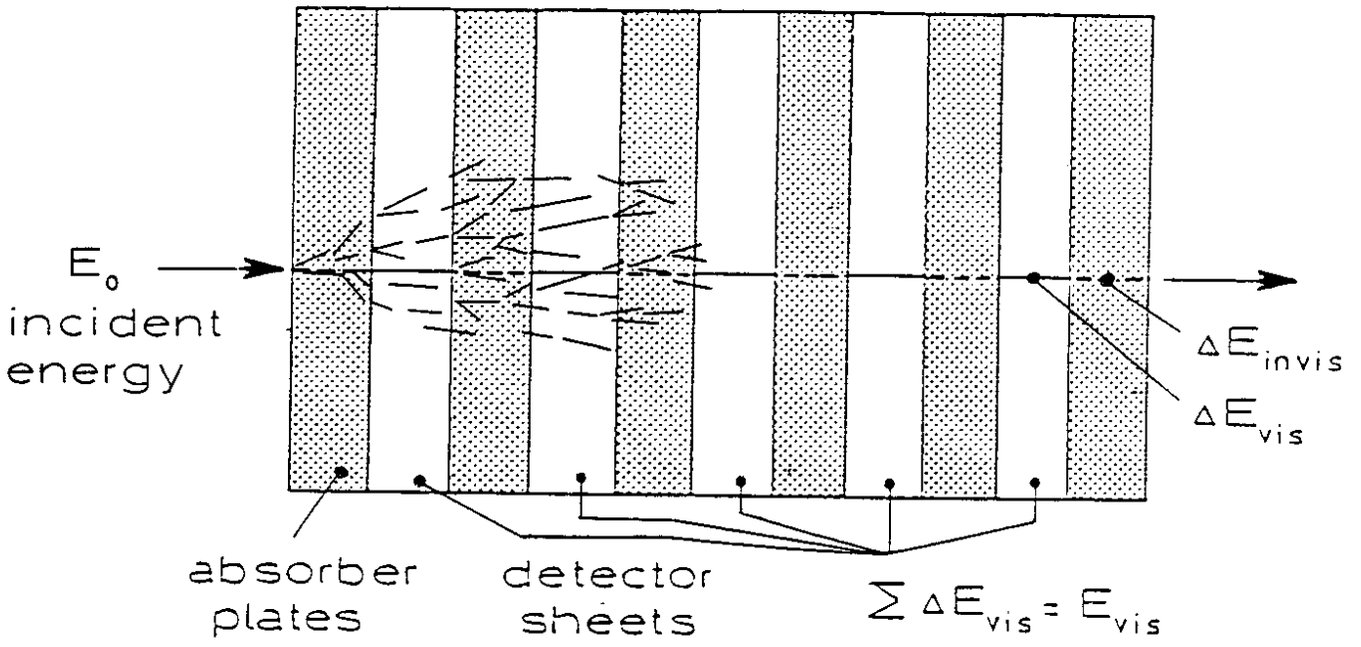


Fig. 2: A shower, induced by a high energetic particle with incoming energy $E_o$, dissipates this energy between the absorber and detector layers. The energy "seen" by the detector material is called $E_{vis}$, the other part of the energy absorbed is called $E_{invis}$. The energy absorbed in the whole calorimeter stack $E_{abs}$ might be less than the incident energy $E_o$ due to front, side and back leaks.

Because the sampling fractions $R_i$ depend strongly on the particle type i and because this subdivision of energy into different shower components can fluctuate widely from event to event, it is customary to normalize the sampling fractions to the sampling fraction $R_{mip}$ of a minimum ionizing particle, mip [2]. (Because muons have ionization losses different from those of a mip, one has to distinguish between μ's and mip's).

| shower components into which energy might divide | normalized sampling fractions $R_i/R_{mip}$ |
|---|---|
| ionizing high energetic heavy particle tracks: ion | 1 |
| electromagnetic energy from $\pi^0$ decay: e | $\approx 0.6$ |
| $\gamma$'s from fission deexcitation and n-capture: $\gamma$ | $\approx 0.3$ |
| neutron kinetic energy: scintillator (including saturation) $n_{E_{kin}}$ | up to 2 |
| liquid argon | $\approx 0$ |
| nuclear binding energy | 0 |
| fission fragments (recoil of heavies) | $\approx 0$ |

Tab. 1: Typical sampling fractions in calorimeters containing high Z absorbers (f.i. uranium).

As an example we abbreviate for an electromagnetic shower $\frac{e}{mip} := \frac{R_e}{R_{mip}}$ and $\frac{\mu}{mip} := \frac{R_\mu}{R_{mip}}$ for a muon (see next paragraph). Tab. 1 illustrates the variations of normalized sampling fractions that are typical for sampling calorimetry [3].

Because the fluctuations of the hadronic shower components are sampled differently, standard calorimeters have e ≠ h (or e/h ≠ 1), where h denotes the average over all contributions within the hadronic shower.

In order to be able to calculate the different contributions to h for various calorimeter setup's quantitatively, a new scale, the C-scale, was introduced [7], which was lateron slightly redefined [1,3]. According to Fig. 3, the mean contribution of the hadronic shower to the measured signal can be written as:

$$h = h_i + C(e-h_i) \tag{2}$$

or

$$\frac{e}{h} = \frac{e}{h_i + C(e-h_i)} \tag{3}$$

$$= \frac{e/mip}{\frac{h_i}{mip} + C\left(\frac{e-h_i}{mip}\right)} \tag{4}$$

C is called the degree of compensation, with C = 1 for full compensation and C = 0 for no compensation; $h_i$ denotes the sampling fraction of the ionizing part of the hadronic shower, which contains the ionizing high energetic heavy particle tracks (this contribution,was called $h_{intr}$ in [7] and is called "purely hadronic" in [5] as well as the electromagnetic energy from the $\pi^\circ$ decay, thus $h_i > h_{intr}$.

Obviously $h_i$ is a function of the incoming energy $E_o$ (this includes the energy dependence of $\pi^\circ$-production: the fraction of energy carried by $\pi^\circ$'s in a shower is approximately equal to 0.1 ln $E_o$ (GeV) [8]) and of e itself: $h_i = h_i(E_o,e)$. Since $h_i$ cannot be measured, it had to be calculated by Monte Carlo (MC) shower codes [9]. For high-Z absorbers (f.i. depleted

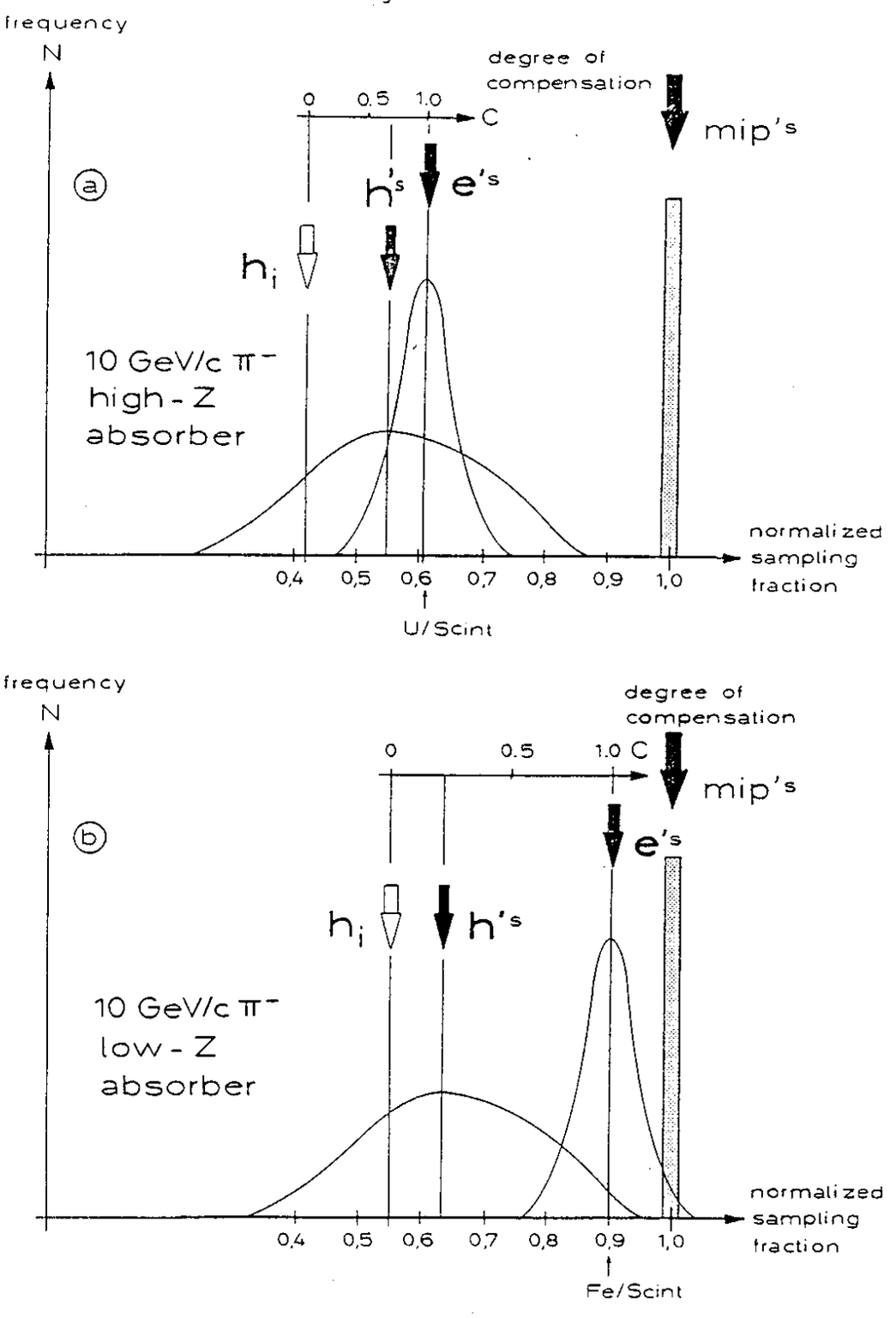


Fig. 3: The definition of the C-scale (degree of compensation) is shown for two hadron sampling calorimeters;
(a) for high-Z absorber layers (f.i. depleted uranium), e/h = 1.1,
(b) for low-Z absorber layers (f.i. iron), e/h = 1.4.
The values given for $h_i$/mip were calculated using the HET-KFA M.C. code for a 10 GeV $\pi^-$ beam, together with results from the EGS code, also shown in the figure.

uranium or lead) $h_i$/mip is about 0.4 (for an incident $\pi^-$ with 10 GeV) and e/mip around 0.6, whereas for low-Z absorbers (f.i. iron or copper), these values are higher: $h_i$/mip $\approx$ 0.55 and e/mip $\approx$ 0.9. These results were obtained from HET-KFA/EGS calculations and are illustrated in Fig. 3a,b. The experimentally measured hadronic signal h (or h/mip) is larger than $h_i$, because of additional contributions, that result from prompt neutrons and nuclear $\gamma$ transport (see chap. I.4). If e/h $\neq$ 1, then h is a nonlinear function of energy and as a consequence, the resolution $\sigma(E)/E$ does not scale with $1/\sqrt{E}$.

One sees that the optimization of the resolution for hadronic calorimeters is much more complicated than for electromagnetic calorimeters [3-8], see chap. II.

## I.2. Calibration with Muons

Since the fictitious mip-particles, introduced in the previous paragraph, cannot be used in practice to calibrate an existing calorimeter, one uses muons for absolute calibration and calculates from the muon signal the signal for a mip. At low energies (several hundred MeV's), the muon signal is close to that of a mip. At higher $\mu$ energies the relativistic rise becomes important. By further increasing the energy bremsstrahlung, pair production and nuclear interactions become dominating. Fig. 4 illustrates the energy losses in bulk material of polystyrene and uranium [10]. Sandwich structures like sampling calorimeters require an even more sophisticated treatment than bulk material. This situation is sketched in Fig. 5, where the passage of a muon travelling through many interleaved layers of absorber (high Z) and detector (low Z) sheets, is shown.

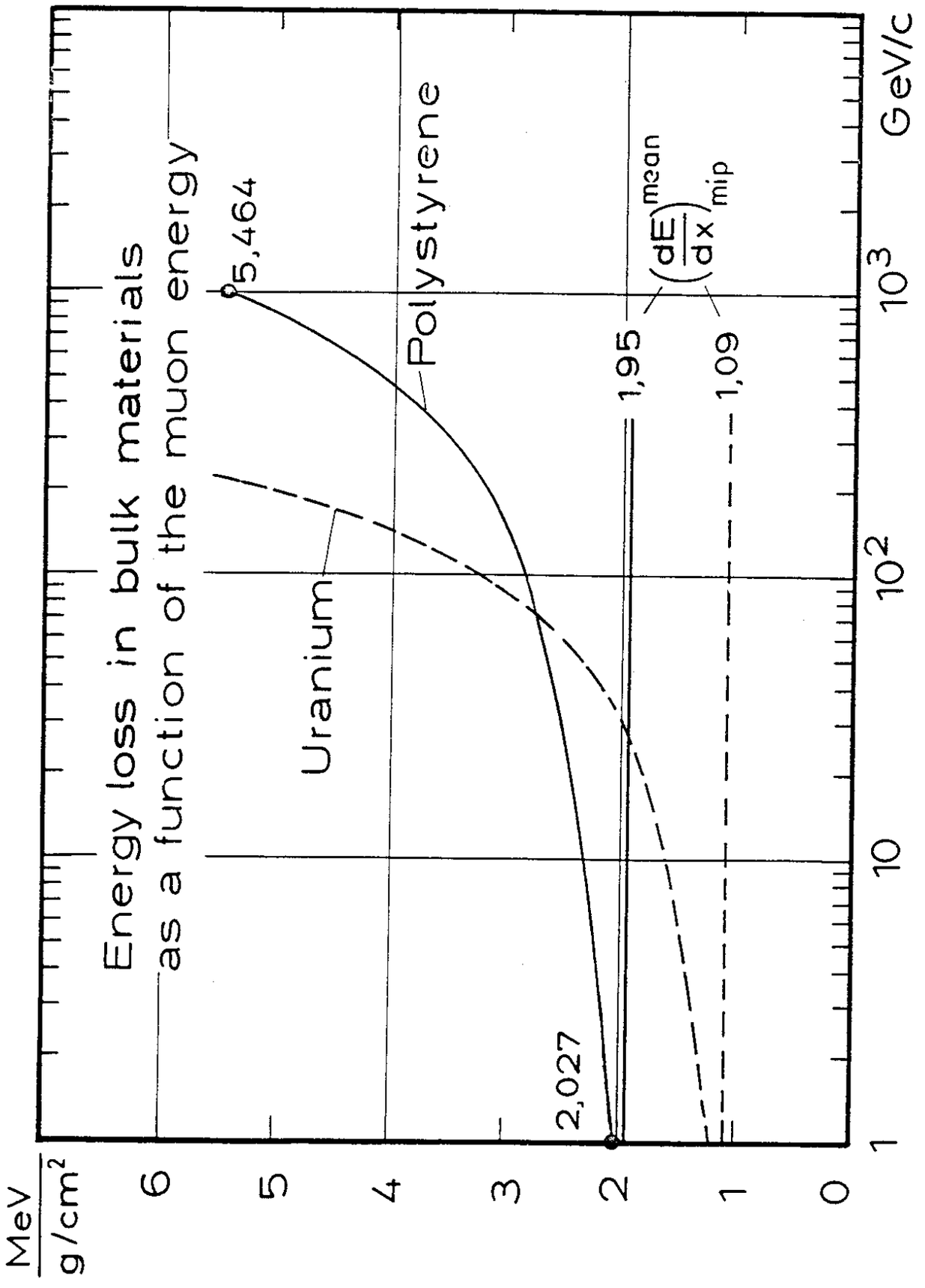


Fig. 4: The mean energy loss of muons in bulk material of polystyrene and uranium as a function of energy. The corresponding energy losses for minimal ionizing particles (mip's) are given for comparison.

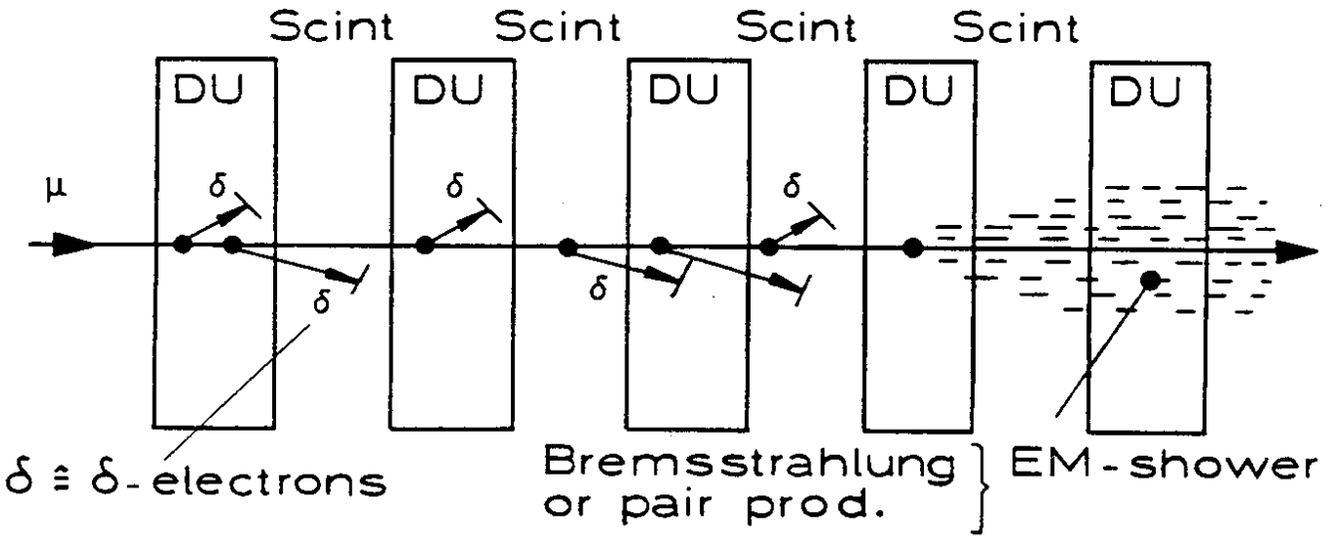


Fig. 5: When a muon is travelling through many interleaved layers of absorber and detector sheets, the effects of the production of δ-electrons, bremsstrahlung and $e^+e^-$-pairs become increasingly important with higher energies.

The effects of δ-ray production, bremsstrahlung and $e^+e^-$ pair production are energy- and material dependent and can be quite different for the absorber and detector layers. Thus $E_{vis}$ and $E_{invis}$ will scale differently with energy.

The quantity $E_{vis}$ is best be calculated by a Monte Carlo procedure rather than by analytical means since δ-electrons created in the absorber might deposit, part of their energy in the detector material, and vice versa. δ-electrons created in the detector might deposit part of their energy in the absorber material. In addition, bremsstrahlung and pair production give rise to an electromagnetic shower, which will not be located in only one sheet.

The MC transport code used here for the primary muon is called MUDEX and was released by Lohmann, Kopp and Voss [12]. This program produces randomly δ-electrons, bremsstrahlung gammas and electron/positron pairs according to the probabilities

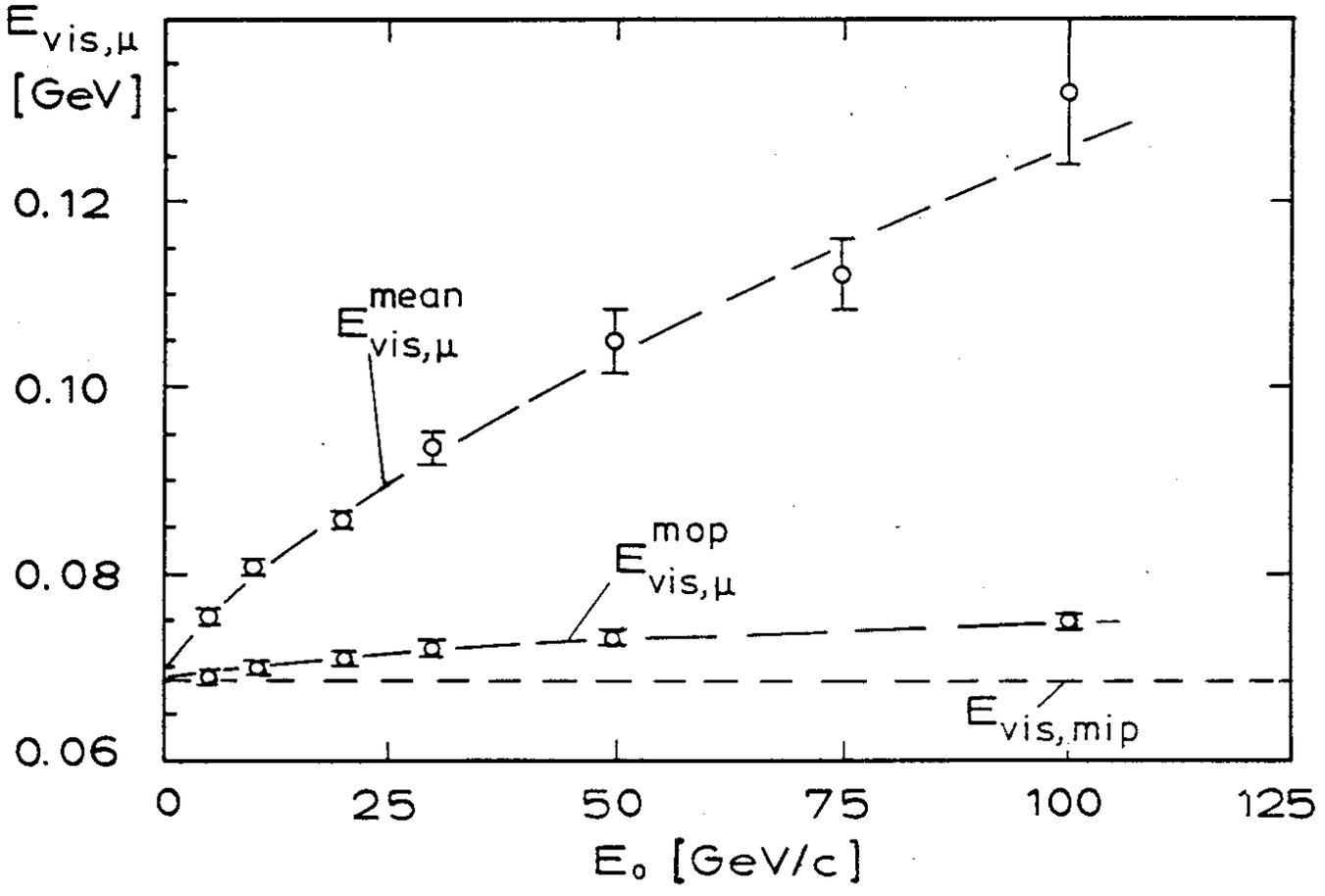


Fig. 6: The visible energy in a test calorimeter containing 134 scintillator-absorber layers [11] has been calculated by the M.C. program MEGS as a function of the muon energy. The mean and the most probable (mop) values are given. The latter is more convenient for calibrational purposes, because the long high energetic tail of the μ-spectrum mixes with hadronic events in an experimental test.

calculated by Bhabha [13], Petrukhin and Shestakov [14] as well as Kokoulin and Petrukhin [15].

Interactions with energy transfer below a given threshold are taken into account by calculating a mean value for this part of the energy loss. They are assumed to be deposited locally, but each of the produced higher energetic δ-rays, bremssstrahlung and particle pairs has to be transported

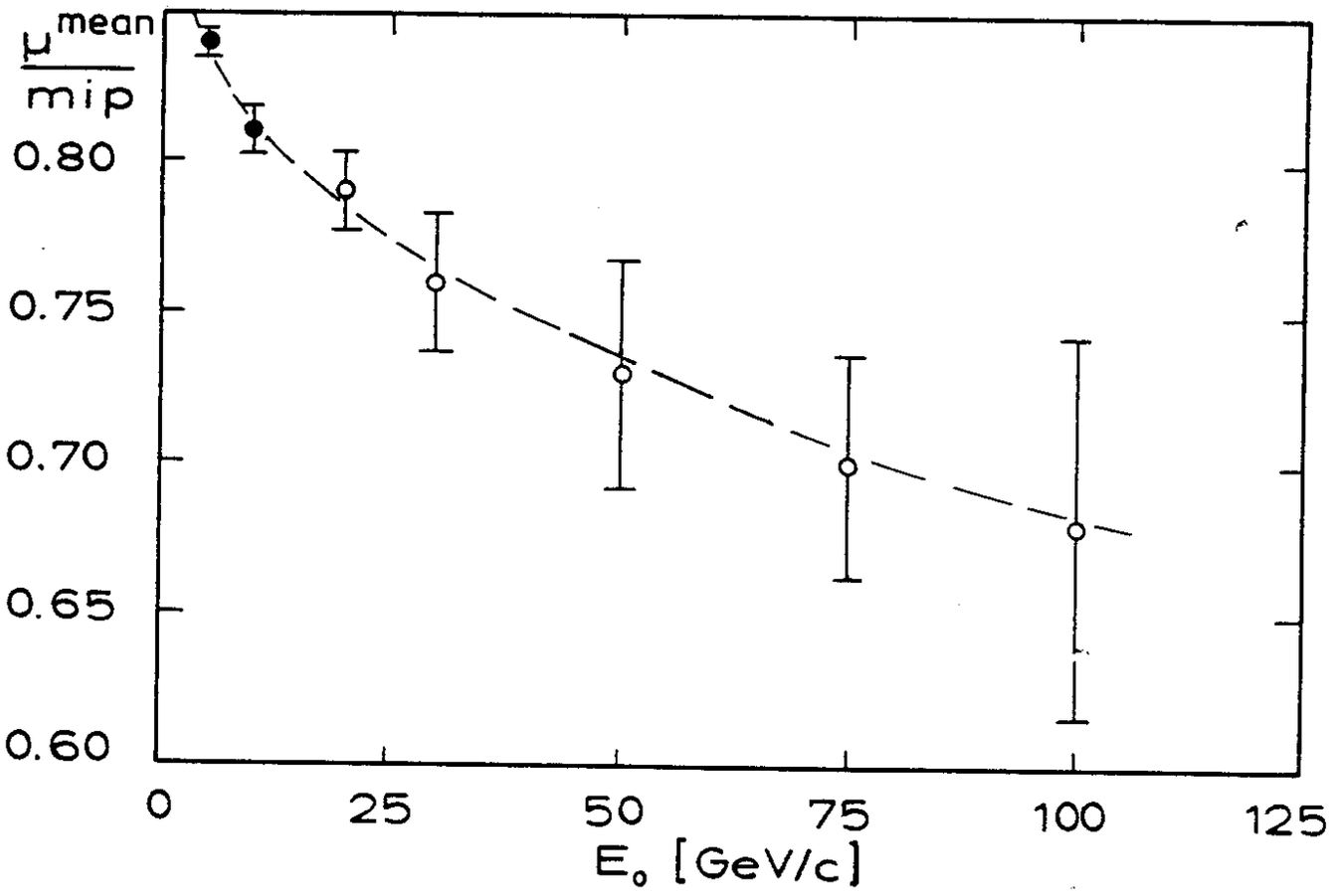


Fig. 7: The calculated normalized sampling fractions of muons are shown as a function of muon energy $E_0$ for a uranium/scintillator calorimeter. The black dots correspond to measured values [11].

within the calorimeter structure. We have done this with the help of the EGS code. Thus the complete code for muon transport requires the coupling of MUDEX with EGS. We will release the combined program with the name MEGS. First results are shown in Fig. 6 for a uranium/scintillator test calorimeter (T35) with 134 layers of 3 mm thick plates and 2.5 mm thick scintillator (SCSN 38) plates [11]. The visible energy for a mip, $E_{vis,mip}$ = 68 MeV, is also shown.

The normalized sampling fraction for muons is decreasing from 1 with increasing energy (Fig. 7).

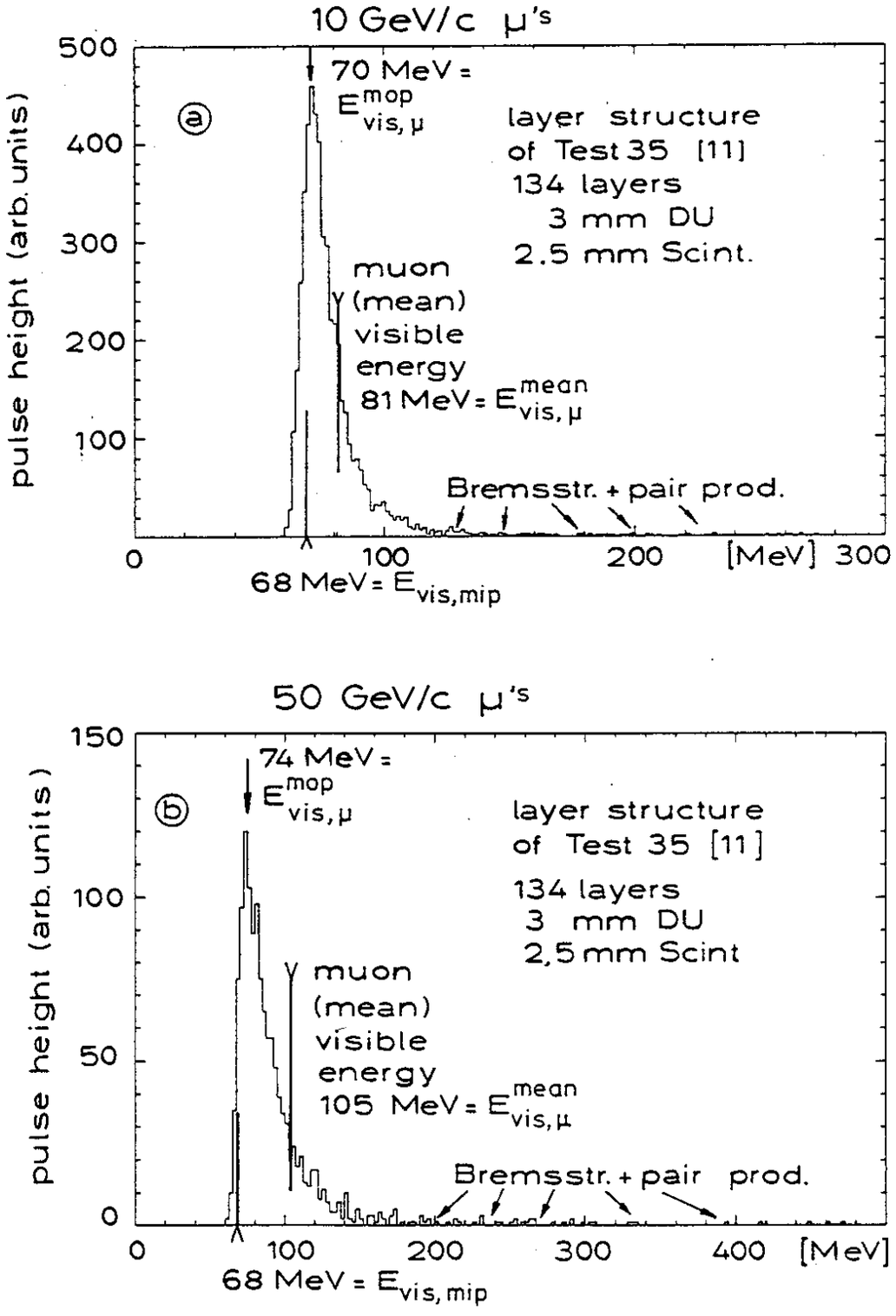


Fig. 8: The muon signal spectrum from MEGS calculations described in the text is "calibrated" with the help of the most probable (mop) value. Then also the corresponding mip-signal can be evaluated.

a) 10 GeV/c $\mu^-$ incident.

b) 50 GeV/c $\mu^-$ incident.

For the test calorimeter T35, a value of $\mu/mip = 0.81 \pm 0.008$ at $E_o = 10$ GeV was calculated with MEGS (with mip = 7.6%, $E^{mean}_{vis,\mu} = 80.7$ GeV, $E^{mean}_{abs,\mu} = 1307$ GeV).

Obviously the muon sampling fraction is not only dependent on the various layer thicknesses, but also on the length of the calorimeter. In practice a calorimeter is a "thin target" for high energetic muons, i.e. $E_{abs,\mu} << E_o$. These facts have to be considered when $\frac{\mu}{e}$-ratios are used from literature for different calorimeter geometries.

The result from the MC calculation for the muon signal (Fig. 8a,b) can now be used to calibrate the experimental signal, which usually is measured in some arbitrary pulse height units. Also shown in Fig. 8 is the visible energy for a mip. For practical reasons, the calibration should be done starting for muons from the most probable deposited energy, since this quantity can in general be determined more accurately than e.g. the average energy loss of muons.

## I.3. The Sampling Fraction for Electromagnetic (EM)-Showers and the Migration of γ-Energy

EM-showers dissipate in general their whole energy $E_o$ in the calorimeter. The energy is carried by an electron (visible) and a photon (invisible) component. Therefore the visible energy can be deposited by the electron component only. As already mentioned in paragraph I.1, the sampling fraction for an electromagnetic shower is slightly smaller than the mip signal for low-Z absorber sheets (f.i. iron or copper), but is significantly smaller for high-Z absorber materials (f.i. uranium or lead). This experimentally well established fact was thought in the past to be due to the socalled "Transition Effect" [16,17]. The Transition Effect states that after crossing the boundary between two different materials, a new equilibrium of the shower is approached adiabatically since a boundary, which separates materials with very different critical energies, modifies the shower development with depth*.

But this effect, though reducing the sampling fraction of the EM-shower, is only important, if the detector layer thickness is in the range of several centimeters, see Fig. 9 (which was taken from Beck's paper [18]). For calorimeter structures with layer thicknesses in the few mm range, the Transition Effect (as discussed above) was shown to play no role by using the EGS shower simulation program [19]. A first hint for the

* The result will be that the build up of the electron flux at a given depth will be larger in the absorber material (low critical energy ≈ 7 MeV; higher bremsstrahlung and pair production cross sections) compared to the detector material (higher critical energy ≈ 30-90 MeV) [18].

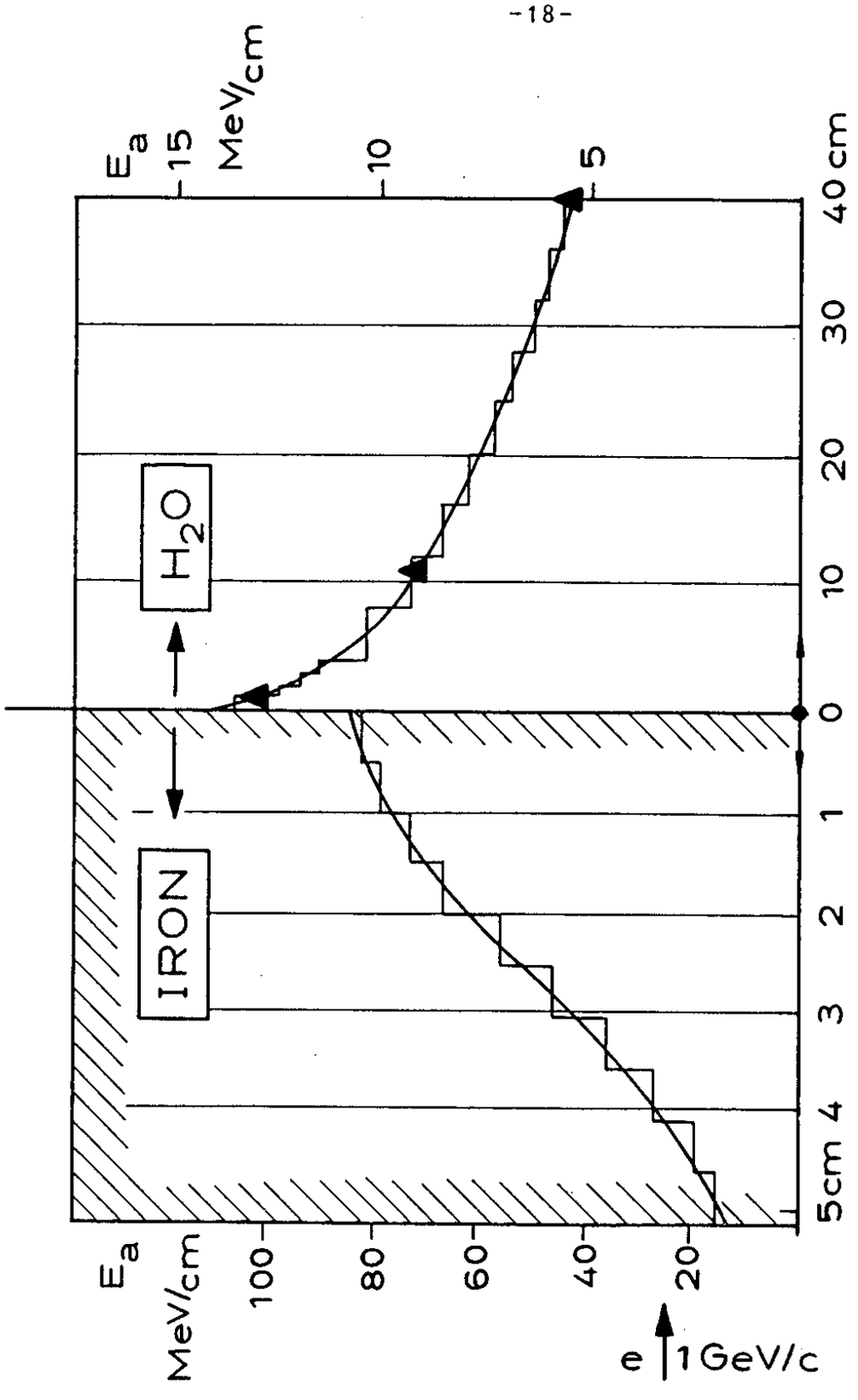


Fig. 9: Energy deposition due to a 1 GeV electron incident on 40 g/cm² of iron followed by 40 g/cm² of water. The histogram shows Monte Carlo calculated results from H.L. Beck [18]. The solid curve is a freehand fit to the data, and the triangles are the experimental data of Crannell et al. [16], normalized at ≈ 11 g/cm² of water. The numbers have been taken from [18]. The normalization of the scales has been changed from g/cm² to cm.

physical reason, why such a big reduction of the EM-response observed in high-Z sampling structures (both experimentally [20] and theoretically [19,21]) takes place, can be found in Beck's paper, too [18]. From MC calculations he found that in the complete development of a 1 GeV EM-shower (in air), there are about 10 times as many photons (greater than 100 keV) as electrons (greater than 1.0 MeV) in the shower. Though no spectral decomposition of the photon component was given, it is clear (at least in the late stage of the shower) that the low-energy ($\leq$ 1 MeV) $\gamma$'s will constitute the major contribution to the photon component in the shower. Since these low-energy $\gamma$'s still have a range of several cm in low-Z material, they can migrate out of the detector layers very easily and are preferentially absorbed in the high-Z absorber material. This is mainly due to the photoeffect, which is proportional to the 4-5th power of Z (as compared to Compton scattering ($\propto$ Z) or pair production ($\propto Z^2$). Thus the total energy contained in the electron spectrum is changed due to the layer structure of different Z materials, because the mass attenuation coefficients for (especially low energy) gamma interactions in matter are very different for the detector and the absorber material [22,23]. Consequently a different name - Migration Effect of $\gamma$-energy - was proposed [7] to characterize this behaviour of an EM-shower in sampling calorimetry [19,21,24]. This effect has been now also nicely calculated for a range of values Z [5], using EGS4 shower simulations.

The result of this migration can be understood better, when one considers the sampling fraction $\gamma$ of the low energetic gammas independent of an EM-shower. This can be done by calculating $\gamma$ from a flow chart of the total gamma-energy around a low energy gamma source, assumed to be localized in

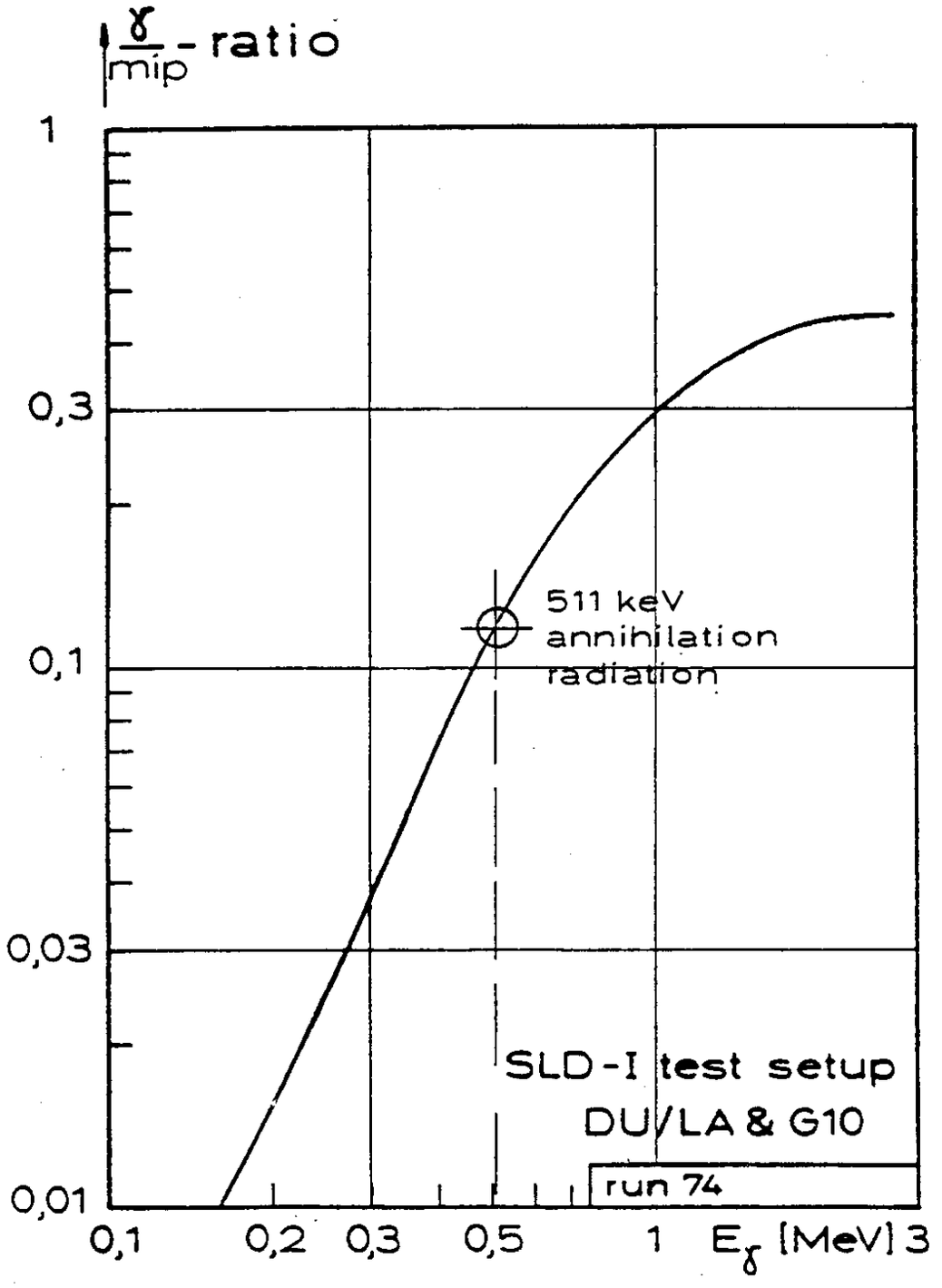


Fig. 10: The normalized sampling fractions γ/mip are shown as an example for monoenergetic gamma sources, homogeneously distributed over one uranium sheet. In the calculation, four uranium layers were used, in the z-direction 6.6 mm thickness each and infinite size in the x-y directions. In between the uranium two LA filled gaps (2×2.4 mm) are situated; they are separated by a G10-sheet (1.8 mm).

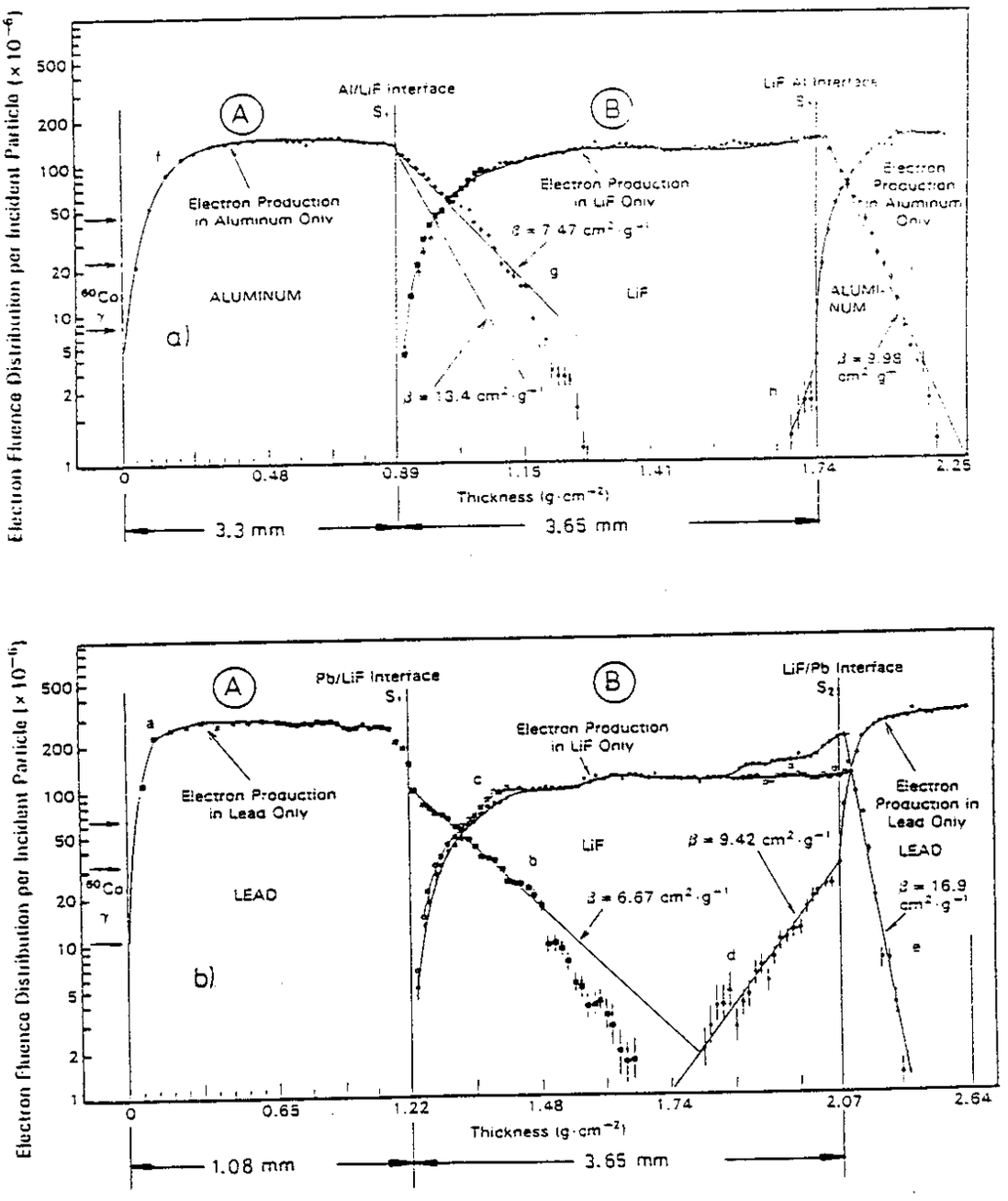


Fig. 11: The electron fluence $\left\{\frac{\#\ \text{electrons}}{\text{cm}^2}\right\}$ distributions (results shown are from literature [27]) as a function of material thickness for Al/LiF/Al (a) and Pb/LiF/Pb (b). The radiator is a $^{60}$Co-source, emitting two gamma lines at $E_\gamma$ = 1.2 and 1.3 MeV with equal intensities. The electron production in the high-Z layer (b) is considerably enhanced (compare curves labelled A), whereas the production in the low-Z layer is nearly the same (see B). For detailed explanation see [27].

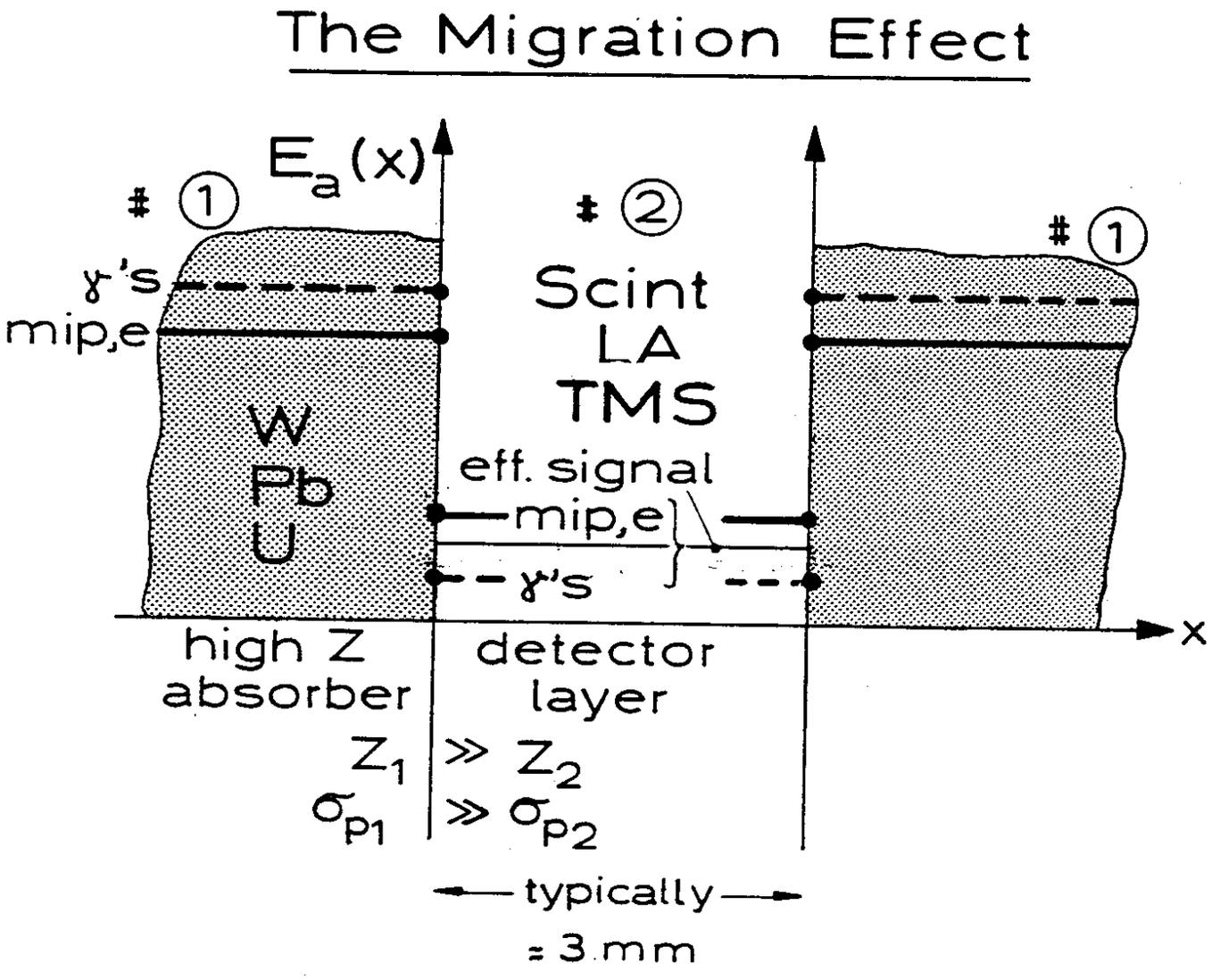


Fig. 12: The migration effect of γ-energy is shown schematically for an EM-shower, passing through a sampling structure (#1 absorber, #2 detector and $E_a(x)$ energy absorbed per unit of length). For high-Z absorbers the effective signal is reduced considerably because the γ-energy is mostly migrating into the absorber sheets.

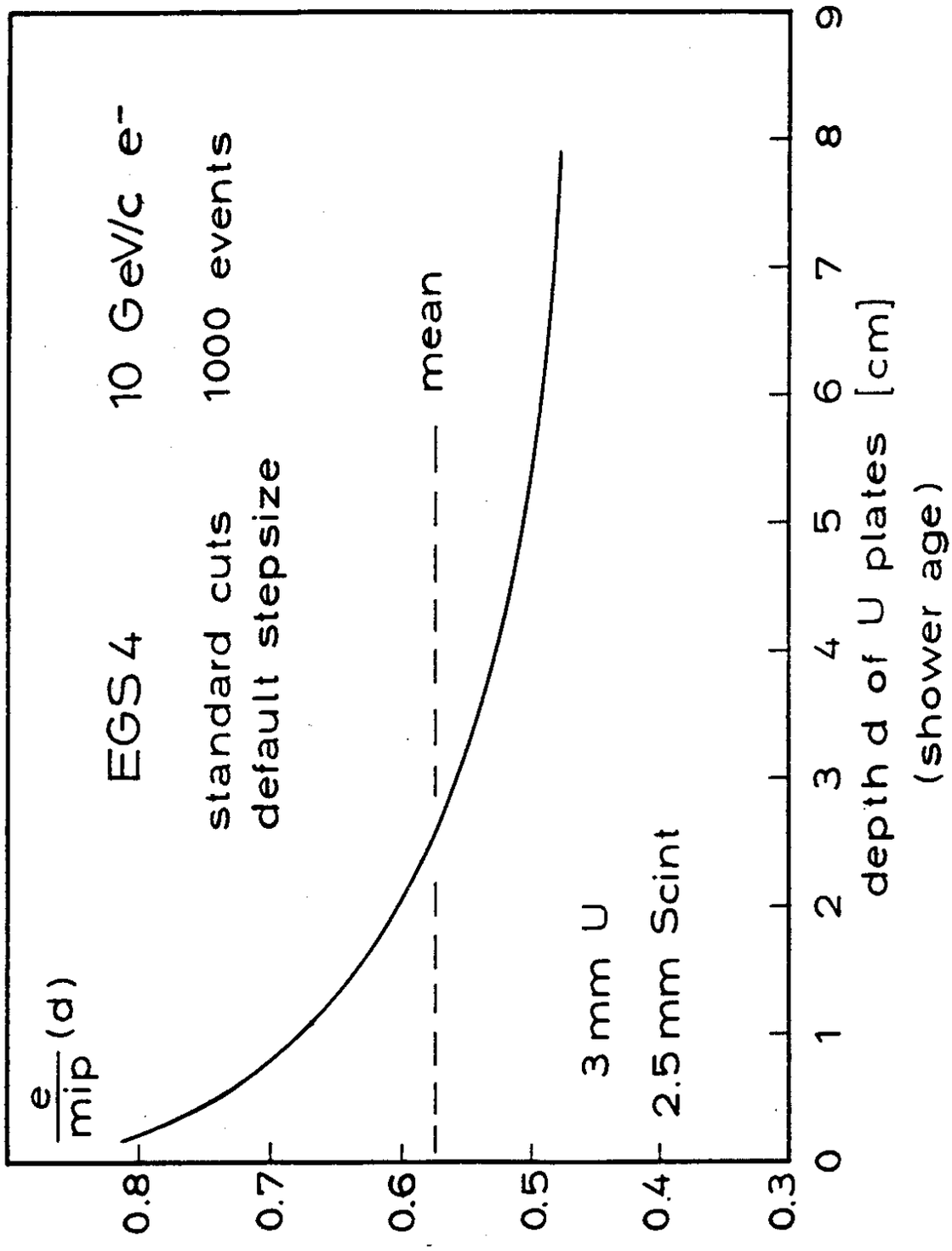


Fig. 13: e/mip as a function of the calorimeter depth d (shower age). The e-signal was sampled from a detector layer using the energy absorption from the preceding and the following absorber plate and then calculating the mean. The thickness of the U plates is indicated.

one of the absorber layers [ 7,25]. Fig. 10 shows these normalized fractions for monoenergetic gamma-sources $E_\gamma$, assumed to be located in one uranium layer of a DU/LA test setup.

As expected these fractions are considerably smaller than one and are strongly dependent on $E_\gamma$. These calculations were carried out using the one-dimensional nuclear gamma transport code ANISN [ 25,26 ] with the restriction that no secondary electron transport can be calculated. Thus the application of this code is somewhat limited in $E_\gamma$, but the continuation of $\gamma$/mip to higher gamma energies can be found now in [5 ], using the EGS4 code.

The enhancement of electron production by low energy gammas in high-Z materials was demonstrated by electron Monte Carlo calculations of Horowitz et al. [27]. In Fig. 11 their results for a Al/LiF/Al and a Pb/LiF/Pb-configuration are given for a $^{60}$Co gamma radiator. The significant reduction in the electron fluence in lead is illustrated as one approaches the Pb/LiF interface.

In Fig. 12 the Migration Effect of $\gamma$-energy within an EM-shower is summarized. The dashed lines indicate the amount of energy released by photons. The effective detectable EM-signal is a mixture of photon and electron energy dissipation.

The influence of the composition of the EM-shower on the e/mip-value is shown in Fig. 13. As expected, an e/mip from a young shower is considerable higher than the mean, whereas an old shower (far away from the shower maximum and consisting of more low energy photons) has a considerable lower e/mip, more in the $\gamma$/mip regime. This might be of great importance when using a very finely segmented read-out.

Because the Migration Effect favours energy deposition in the high-Z material (usually the absorber), calorimeters show an EM-response e/mip smaller than one. This is shown in Fig. 14 for scintillators with U, Pb, Fe and Cu absorber layers*.

The experimentally determined e/μ-ratios need a careful analysis to convert the energy dependent μ-values to the mip-sampling fraction (see chap. I.2). For this reason experimental points are not shown in Fig. 14.

Practical calorimeters might have a metallic cladding layer on the absorber sheets [1,3], see Fig. 15, which may decrease the e/mip ratio by up to 10% as shown in Fig. 14 by the open circles.

---

* As indicated in the figure, these results were obtained by using standard cuts (ECUT = AE = 1.5 MeV and PCUT = AP = 0.1 MeV) and the default stepsize algorithm from the EGS3 code. It has been pointed out by D.W.O. Rogers [28] that for precise calculations with EGS, lower cut-off energies and a properly adjusted stepsize has to be used in the calculations. Otherwise, in case of many thin layers, interface artefacts can spoil the accuracy of the calculation considerably [29]. Using EGS3 with the option of D.W.O. Rogers [28](simulating more precise the intrusion of energy in the scintillator sheets on the cost of an enormous increase in CPU-time) results in steadily increasing e/mip ratios (see the Δ symbol in Fig. 14). This option is now available within the standard EGS4 release [30], correcting also some old errors, which had affected the transport of electrons below 10 MeV in EGS3 [28]. To speed up this "tuning", also for the inexperienced user, a new electron transport algorithm has been proposed for use with EGS4, called PRESTA (Parameter Reduced Electron-Step Transport Algorithm, [31]). This new version has not been applied to calorimetry up to now; the results calculated with the standard options (Fig. 14) are mainly used in this paper.

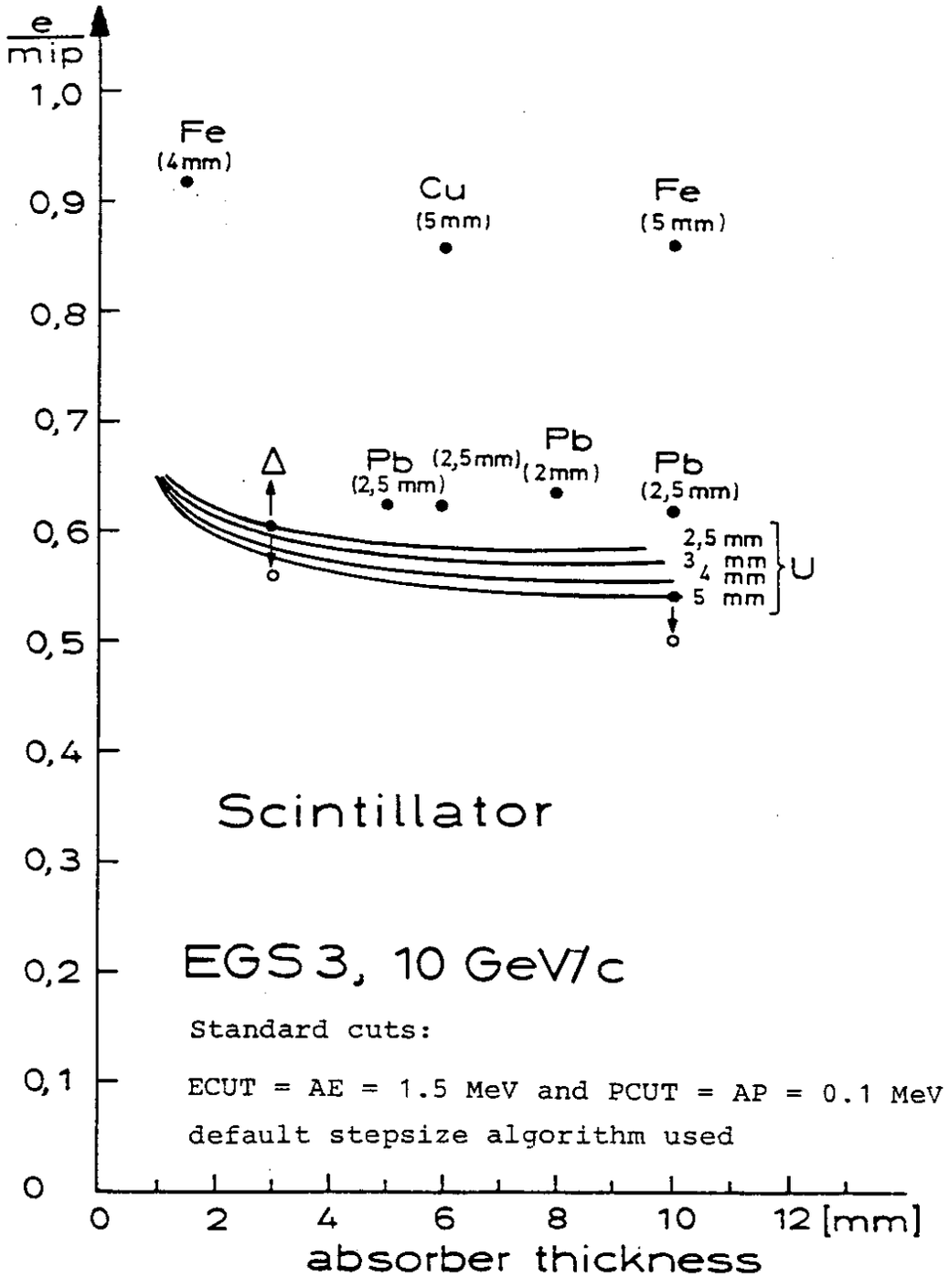


Fig. 14: e/mip ratios for various absorber- and scintillator-thicknesses, each 100 layers deep and ±∞ size in x-y directions. A slight dependence of e/mip with the scintillator thickness is seen. The open circles give the result for clad absorber sheets (2×0.4 mm Cu for the 3 mm U-sheet and 2×1 mm Fe for the 10 mm U-sheet). The Δ symbol belongs to an EGS calculation using reduced cuts (ECUT = 0.711 MeV, AE = 0.700 MeV and PCUT = AP = 0.1 MeV) and smaller step sizes (ESTEPE = 0.5%).

Detail of HAD - Section for Model Calculations

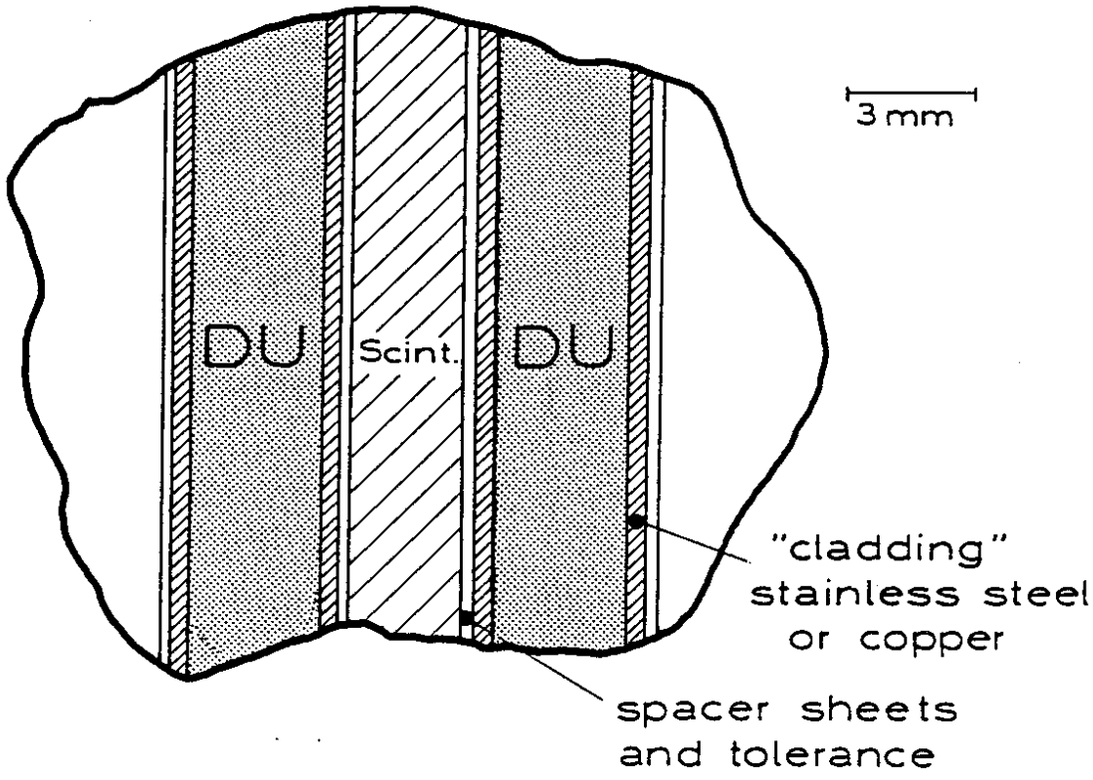


Fig. 15: A sampling structure with cladding, used for the model calculations.

The fine tuning of the e/mip ratio is shown in Fig. 16 for T35 [11]as a function of the cladding thickness in more detail. Only if the cladding thickness is bigger than 2 mm on each side, the e/mip is increasing and, as expected from Fig. 14, is approaching the upper curve, where the absorber is purely copper (with a thickness of two times the cladding thickness scale). Only then the e/h-ratio could be increased due to the cladding, too [6].

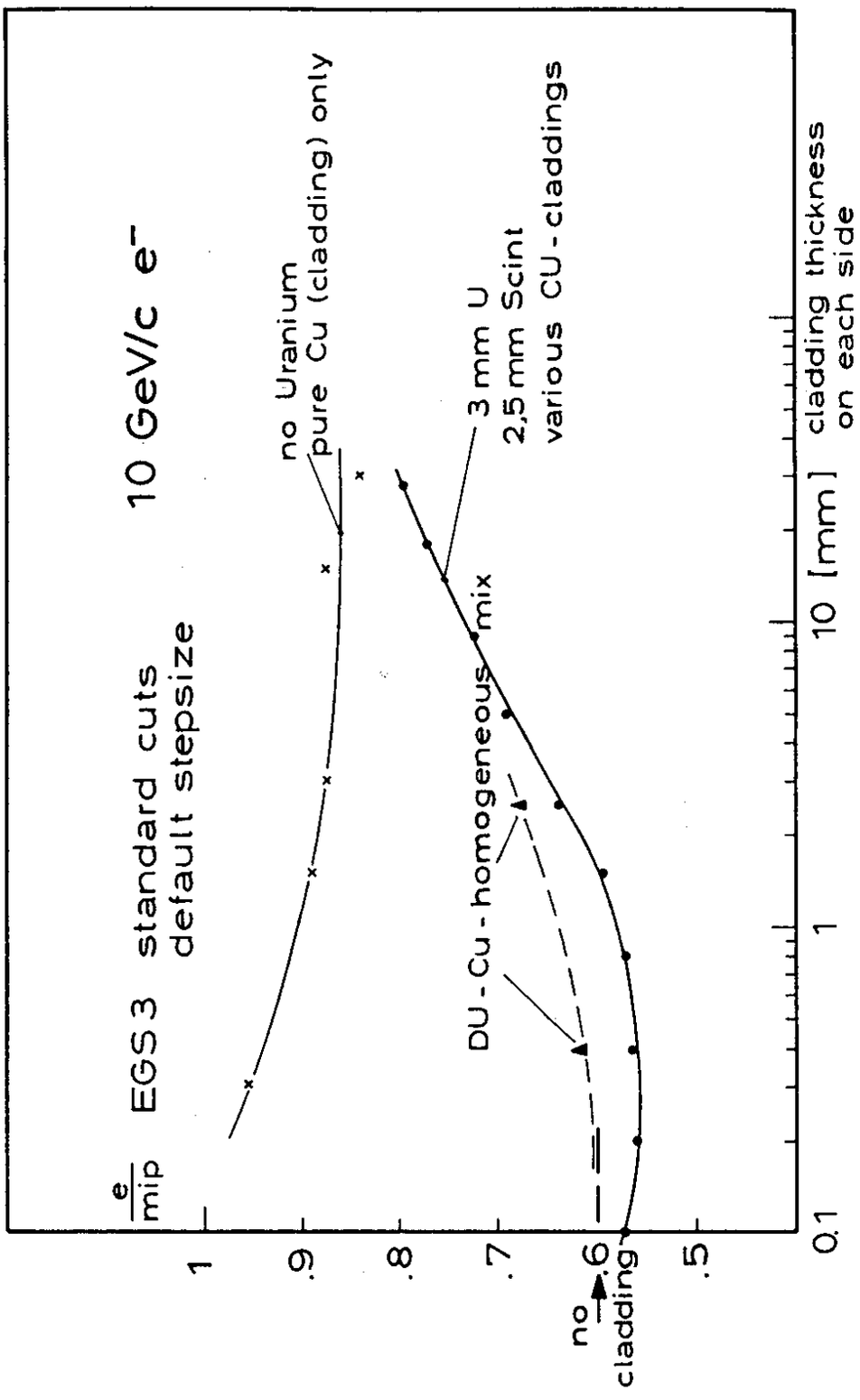


Fig. 16: The variation of the e/mip ratio with increasing thickness of the Cu-cladding is illustrated for a uranium/scintillator calorimeter stack. Together the corresponding pure copper/scintillator e/mip ratios are given. The two ▲ symbols indicate the e/mip values for a homogeneously U-Cu mix, using the same amount of copper as for the cladding to eliminate the surface effect (see text). In this case, no minimum is observed.

The reduction, f.i. for a 2×0.4 mm Cu-cladding, comes from the combined effect of an even bigger reduction in the electron sampling fraction e ($\sim$ 23%) and a smaller increase of the mip-fraction ($\sim$ 15%) due to the increased contribution to $E_{invis,mip}$ from the cladding. This combines to a 6.5% effect in reducing the e/mip at this point. The 23% decrease in e itself is a combined effect from low energy electron and photon transport (surface effect). An estimate, using the gamma transport code ANISN [26], gives a 9% reduction of the photon component due to the cladding. Thus the main effect could be understood mainly in terms of shielding electrons on their way between the high-Z absorber (acting as an electron "source", see Fig.11b) and the detector layer. If the same amount of Cu is not located as a cladding at the surface of the absorber plate, but is mixed homogeneously with the uranium, the reduction effect disappears supporting the explanation just given (see Fig. 16).

## I.4. The Mean Response to Hadrons

The energy losses of high energy particles (> 1 GeV) travelling through matter are mainly determined by production of secondary particles. The main feature of the cascades generated in matter is an initial (in depth) increase of particle intensity as a result of secondary particle production. If the energy of the produced secondary particles is high enough, they in turn will produce additional particles. This process is very similar to the chain reaction which is well known from nuclear fission. But in contrast to the chain reaction of nuclear fission, there exists a physical limit for the development of the cascade, because the initial energy of the primary particles is distributed over all particles produced. Therefore, the multiplicities decrease during the cascade process and fade away, because the average energy of the cascade particles decreases and a greater fraction of the individual particle energy is dissipated by ionization losses. During the cascade process subsequent production of many low energy particles, mainly neutrons, takes place, known as evaporation process.

The term intranuclear cascade is used to describe the process creating a particle "cascade" inside one nucleus (see Fig. 17). In matter, namely in a socalled "thick" target, such nuclear collision products can proceed to produce further collisions with other nuclei to form an internuclear cascade. To analyze the particle shower and its distribution in energy and space, one has to determine the multiplicities, energy and angular distributions of the particles produced.

The incident particle interacts with a single nucleon inside the nucleus, such as if each nucleon would be in free space. The collision is not exactly analogous to one in free space, because the Pauli principle will exclude encounters with

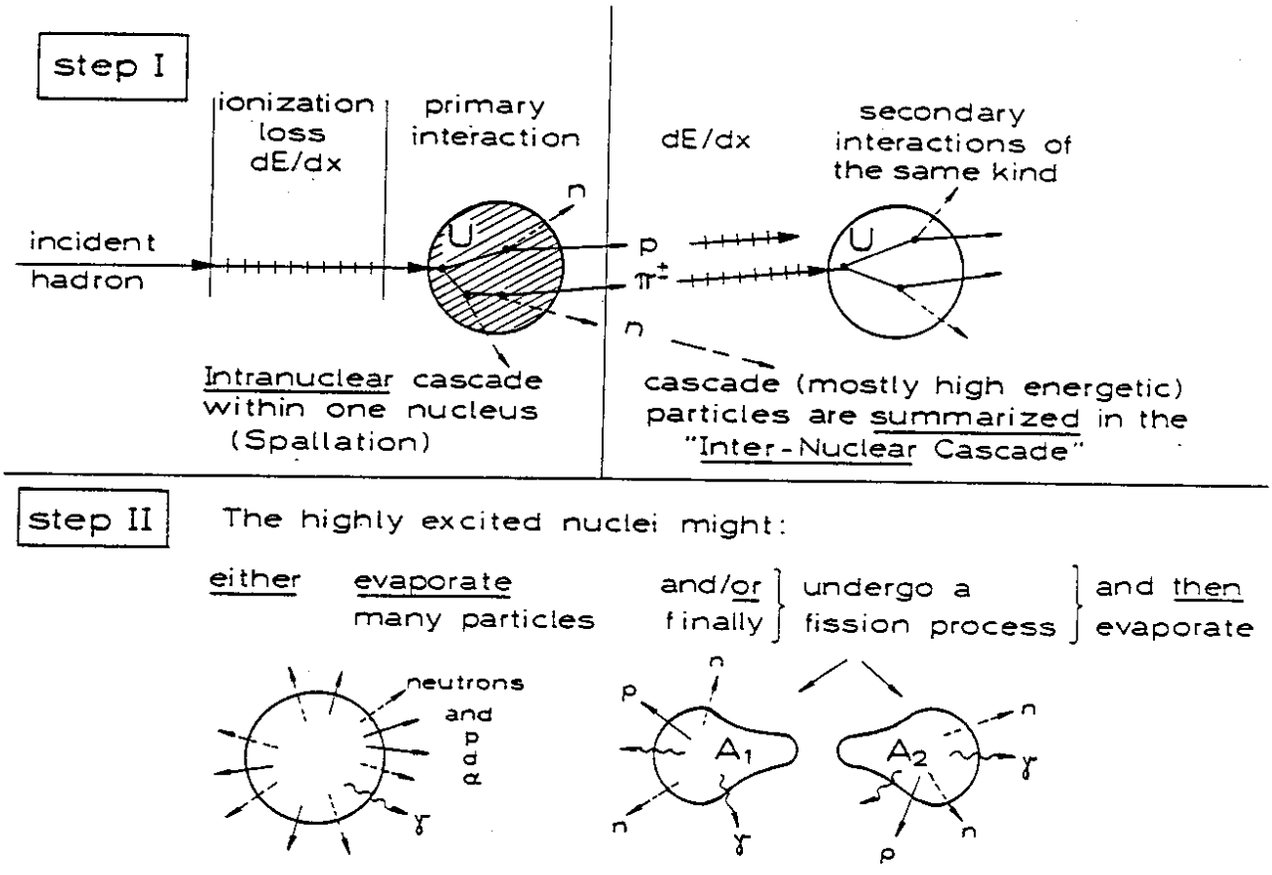


Fig. 17: Step I: Development of an "Internuclear cascade". From one nucleus an intranuclear cascade releases a few (mostly) high energetic particles, which are able to initiate further intranuclear cascade processes.

Step II: The highly excited nuclei remaining from each intranuclear cascade deexcitate.

certain momentum transfers. Also, at high energies, the bombarding particle can traverse the nucleus without experiencing an interaction, resulting in "nuclear transparency".

The number and the kinetic energies for each kind of particle appearing in the internuclear cascade are summarized in the cascade-yield and the cascade-spectrum (Step I in Fig. 17, the time scale is $\approx 10^{-22}$ sec). The deexcitation and associated

particle emission of the highly excited nucleus remaining after the intranuclear cascade is determined by applying the statistical theory of evaporation. The probability of emission of a particular particle type (neutron, proton or clusters - such as deuterons, tritons, $^3$He or alpha particles) can thus be formulated (Step II in Fig. 17, the time scale is $\approx 10^{-18}$ sec).

For very heavy nuclei, there is competition between evaporation and fission at each step of the deexcitation sequence. The probability of fission at some step during deexcitation in high-energy ($\gtrsim$ 100 MeV) collisions is proportional to $Z^2/A$ of the target nucleus. For example, $\sigma_f/\sigma_t \sim 0.05$ for lead and $\sigma_f/\sigma_t \sim 0.8$ for uranium [32]. The number and the kinetic energies of the evaporation particles (either from heavy nuclei evaporation or fission product evaporation) are summarized in the evaporation-yield and the evaporation-spectrum.

To study the relevant physics associated with the interaction of high-energy hadrons with matter, computer simulations via Monte Carlo methods are very suitable. A very potent theoretical model, the intra-nuclear-cascade-evaporation model (INCE) treating mainly the nonelastic interaction of high-energy hadrons with nuclei is used in the HETC (High Energy Transport Code) Monte Carlo system. This code system and its basic features is described in [33].

The advantages of the method are briefly summarized:

- The model is parameter free and provides results with absolute normalization.
- The model requires mainly only particle-particle cross section data, which are relatively well known.
- The model has been shown to be in reasonably good agreement with a wide range of experimental data.

- The model has rather general applicability to:
  a) all target nuclei with A > 5;
  b) different projectile particles (neutrons, protons and charged pions).

  The valid energy range is not well defined. The lower energy limit is ∿ 15-100 MeV. The Bertini implementation of the model is limited to energies below ∿ 3 GeV, because only single and double pion production are included. Rather ad hoc extensions to tens, even hundreds, of GeV have been made by using approximate scaling relations [34]. Barashenkov et al. [35] and recently Bertini et al. [36] have made modifications to the basic model (e.g. to incorporate nuclear depletion, which takes into account the time dependence of the changing nucleon density in the path of the developing cascade) to extend the upper energy limit to ∿ 1000 GeV.

- The model is capable of providing very detailed output results, including
  a) type, energy and direction of each emitted particle;
  b) type and recoil energy of residual nuclei;
  c) the photon source from $\pi^\circ$ decay and nuclear deexcitation;
  d) the low-energy (< 20 MeV) neutron production, which is of considerable interest in particle problems related to sampling calorimetry [7,37]. This last point makes the HET-code superior to other hadronic cascade MC codes such as GHEISHA [38,39] or FLUKA [40].

The neutron yields for $E_n \leq 20$ MeV for $\pi^-$ or p incident on a block (60×60×300) cm or a cylinder (ø 300×300) cm of depleted uranium (99.8% U-238, 0.2% U-235) and of natural lead are given in Tab. 2 from HET-KFA calculations [9]. Compared to the block calculations, the n-yield for the lateral bigger sized cylinder gives an estimate for the transverse leakage of

| n-yield per 10 (2.5) GeV/c $\pi^-$ incident | |
|---|---|
| | $E_{n,kin} \leq 20$ MeV |
| DU-Block | 326 (89) |
| DU-Cyl. | 337 |
| Pb-Block | 222 (61) |
| Pb-Cyl. | 245 |
| n-yield per 10 GeV/c p incident | |
| DU-Block | 360 |
| Pb-Block | 236 |

Stat. error better than 1%.

Tab. 2: The neutron yield from HET-KFA calculations for blocks (60×60×300) cm and cylindrical (ø 300×300) cm geometries.

neutron energy which is for DU: ∿ 3%; for Pb: ∿ 10% at 10 GeV. The spectral distribution of the low-energy neutron production for a $\pi^-$ with 10 GeV incident on a DU- or a Pb-block is shown in Fig. 18.

In Fig. 18 the ordinate is the quantity $E[d\Phi(E)/dE]$, where $d\Phi(E)/dE = Y(n,E)$ is the distribution of the neutron yield with respect to the neutron energy $E_n$. The area under a curve of $d\Phi(E)/dE$ versus E between two energies $E_1$ and $E_2$ equals the yield in this energy range. Similarly, the area under a curve of $E[d\Phi(E)/dE]$ versus the logarithm of E, (i.e. the neutron

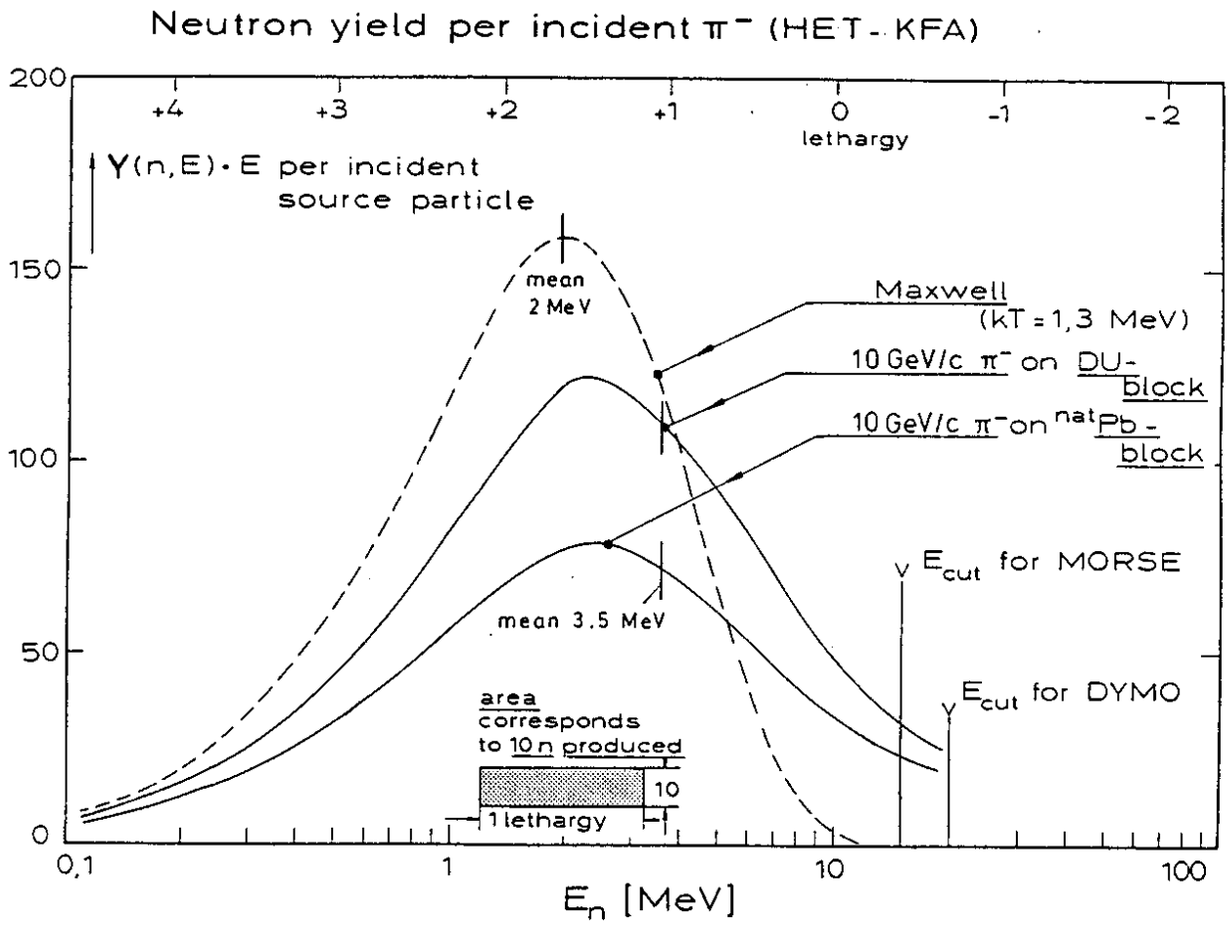


Fig. 18: The energy dependent neutron yields Y(n,E) per MeV and per incident 10 GeV/c $\pi^-$ bombarding a uranium or a lead block, respectively. Plotted is the product Y(n,E)·E versus the lethargy of the neutron energy (upper scale). The 3-dimensional HET-KFA M.C. code was used. The block-sizes were 60×60×300 cm each. The spectra shown are used as input for the low-energy neutron transport calculations with separate programs.

energy expressed in units of lethargy = $\ln \frac{10}{E\,[MeV]}$) between the same two energies, also equals this part of the yield. Thus, plotting $E[d\Phi(E)/dE]$ versus the logarithm of E allows the spectrum to be displayed over a larger range of energies in a way that preserves area representation and gives a clear indi-

cation of the relative contributions of "slow" and "fast" neutrons. For comparison, a Maxwell spectrum is shown with kT = 1.33 MeV (mean energy = 3/2 kT = 2 MeV), normalized to the same number of neutrons, produced in the DU-block (dashed line). The Maxwell spectrum describes the neutron distribution from secondary or tertiary fissions (induced by the low-energy neutrons shown (solid line), usually called "fast-fission" (to distinguish the fission of U-238 from the fission of U-235, which takes place mainly in the eV (thermal fission) regime). It is clearly visible that the $\pi^-$ initiated spectrum (solid line) is shifted to higher energies with a mean of 3.5 MeV. In lead the nuclear cascade, as described earlier, produces a neutron spectrum, which is very similar in shape compared to the neutron production from DU, but the number of neutrons produced is considerable less (see Tab. 2).

A closer analysis of the numbers given in Tab. 2 shows that the contribution of cascade neutrons (Step I) to the low-energy yield is nearly the same for the DU and for the lead target, but there is a difference due to the evaporation neutrons (Step II), see Tab. 3. The determination of this neutron yield and its dependence upon target material mass number and beam energy has been the objective of several experimental and theoretical studies. Most of the available data are summarized in [41].

So far, the creation of neutrons within a "thick target", like a hadron calorimeter, has been discussed without considering the interleaved layers of low-Z detector material. These layers have only a minor effect on the neutron yield, as shown by simulating the real structure of a sampling calorimeter [42]. But the transport of the neutrons created can be affected

| n-yield ($\leq$ 20 MeV) per 10 GeV/c $\pi^-$ incident | | | | | |
|---|---|---|---|---|---|
| Target | Low-energy yield y. | = | casc. y. | + | evapo. y. |
| DU-cyl. | 337 | = | 49 | + | 288 |
| Pb-cyl. | 245 | = | 46 | + | 199 |

Tab. 3: The composition of the low-energy neutron yield for 10 GeV/c $\pi^-$ on the cylindrical geometry. (In the case of Pb no other elements have been added. Usually Pb is used together with 4-10% antimony in spite of an enhanced mechanical strength. This would affect the n-production.

considerably by detector materials containing hydrogen (f.i. scintillator or TMS), since the (n,p) scattering cross section is a strongly increasing function with decreasing neutron energy, see Fig. 19.

To cope with this phenomena, the low-energy neutron source ($E_n \leq 20$ MeV, Fig. 18) is not transported by the HET-code, but is submitted (as a source) to specialized programs like DYMO [43], a 0-dim. (deterministic) transport code with time dependence, or ANISN [26], a 1-dim. (deterministic) transport code or MORSE [44], a 3-dim. (MC) transport code. For all three codes energy spectra for neutrons (and gammas as well) are properly binned into energy groups. Group-to-group transfer probabilities are extracted usually from evaluated nuclear data libraries for nearly all nuclei and each energy group. This library is based on experimental data [45] and contains

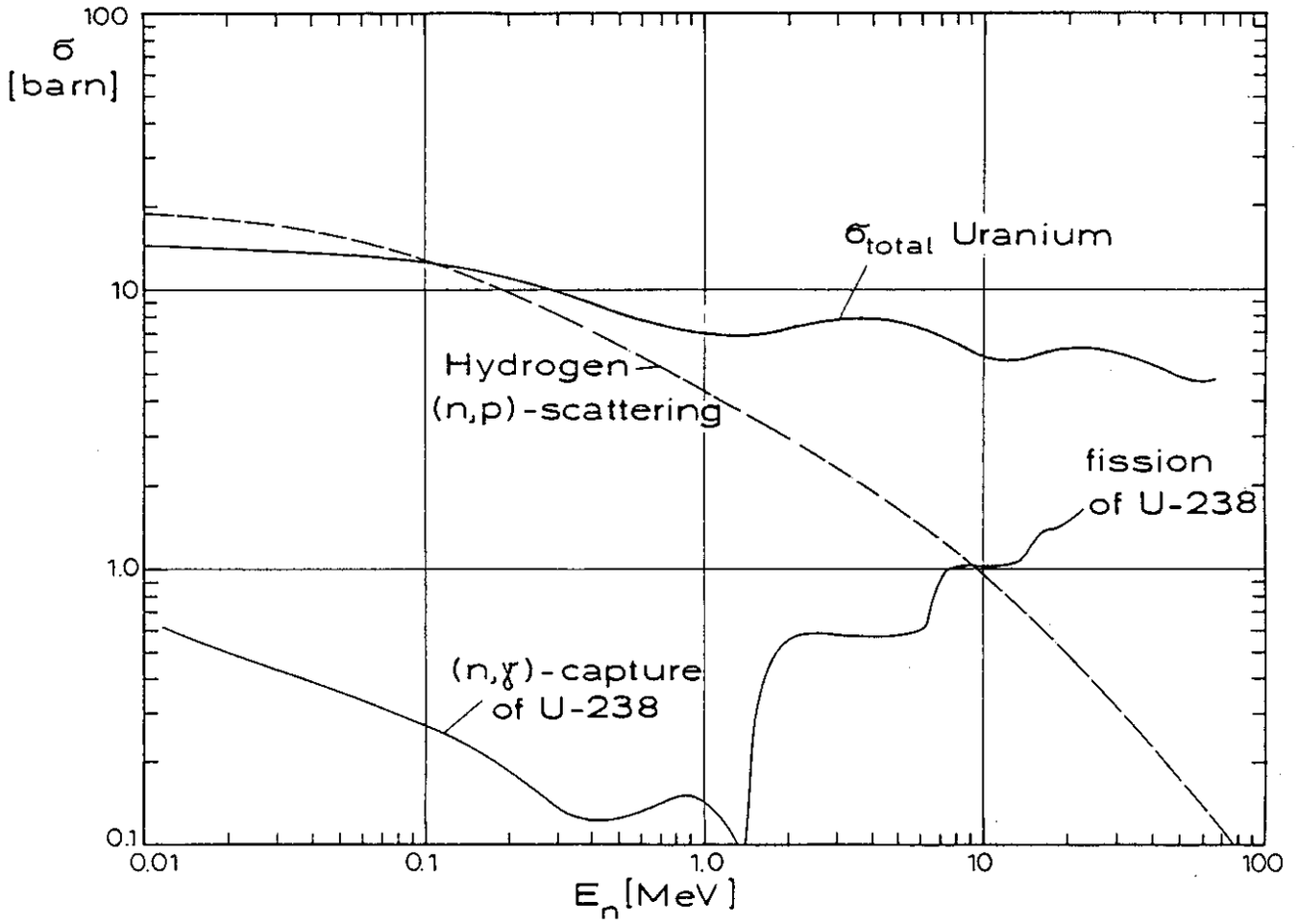


Fig. 19: Some cross sections for neutron induced reactions on uranium-238 and hydrogen which are important for the interactions of the low-energy neutron component in the hadronic shower.

the relevant neutron (Fig. 19) and/or gamma reactions. The DLC 31 (or FEWG 1) library [46], which covers 37 neutron groups ($10^{-5}$ eV $\leq E_n \leq$ 20 MeV) and 21 gamma groups (10 keV $\leq E_\gamma \leq$ 14 MeV), has been used so far for DYMO or ANISN and the EPR-Lib [47] with 100 neutron groups ($10^{-4}$ eV $\leq E_n \leq$ 15 MeV) and the 21 gamma groups, too, for MORSE. Reliable data material concerning nuclear reactions with neutrons is known only up to 20 MeV. There are experimental attempts to increase this limit up to 50 MeV or/even higher [48].

Due to the well known moderation of several MeV neutrons by hydrogeneous materials [49], the time scale is also changed from $10^{-18}$ sec (Step II in Fig. 17) to $10^{-9}$-$10^{-6}$ sec. This justifies to consider the spectrum, shown in Fig. 18,as being build up "promptly". Though the 3-dim. (MC) MORSE-code can be operated in a time-dependent mode, too (which is more CPU-time consuming), a separate code, DYMO [43], was developed which operates in the homogeneous (and infinite) material mixture of the calorimeter considered. The simplified use of a homogeneous (0-dim.) mixture (material mix - expressed in # atoms/cm$^3$, corresponding to the thicknesses used -) is clearly justified by Fig. 20, where the mean free path for neutrons (for a 3 mm DU/2.5 mm scintillator sampling structure) is shown. It is in the range of 10 to 50 mm. The graph does not change very much for other (typical) geometries.

DYMO uses small steps of time (f.i. 0.1 nsec) to evaluate the number of neutrons being affected either in their energy or lost to fission or capture. After each step in time all the 37 neutron energy groups are updated in content. This includes the gain of neutrons by fast fissions (secondary or tertiary fission - the primary fission was the high-energy fission, calculated with HETC). For the fast-fission spectrum the Maxwellian, shown in Fig. 17 with kT = 1.33 MeV, is used (neglecting the small dependence of this spectrum with $E_n$, but taking into account that the multiplicity of the neutron production $\bar{\nu}$ is a function of $E_n$:

$$\bar{\nu}(E_n) = 2.358 + (0.156\ E_n) \text{ for U-238} \qquad (5)$$

$$\bar{\nu}(E_n) = 2.430 + (0.106\ E_n) \text{ for U-235} \qquad (6)$$

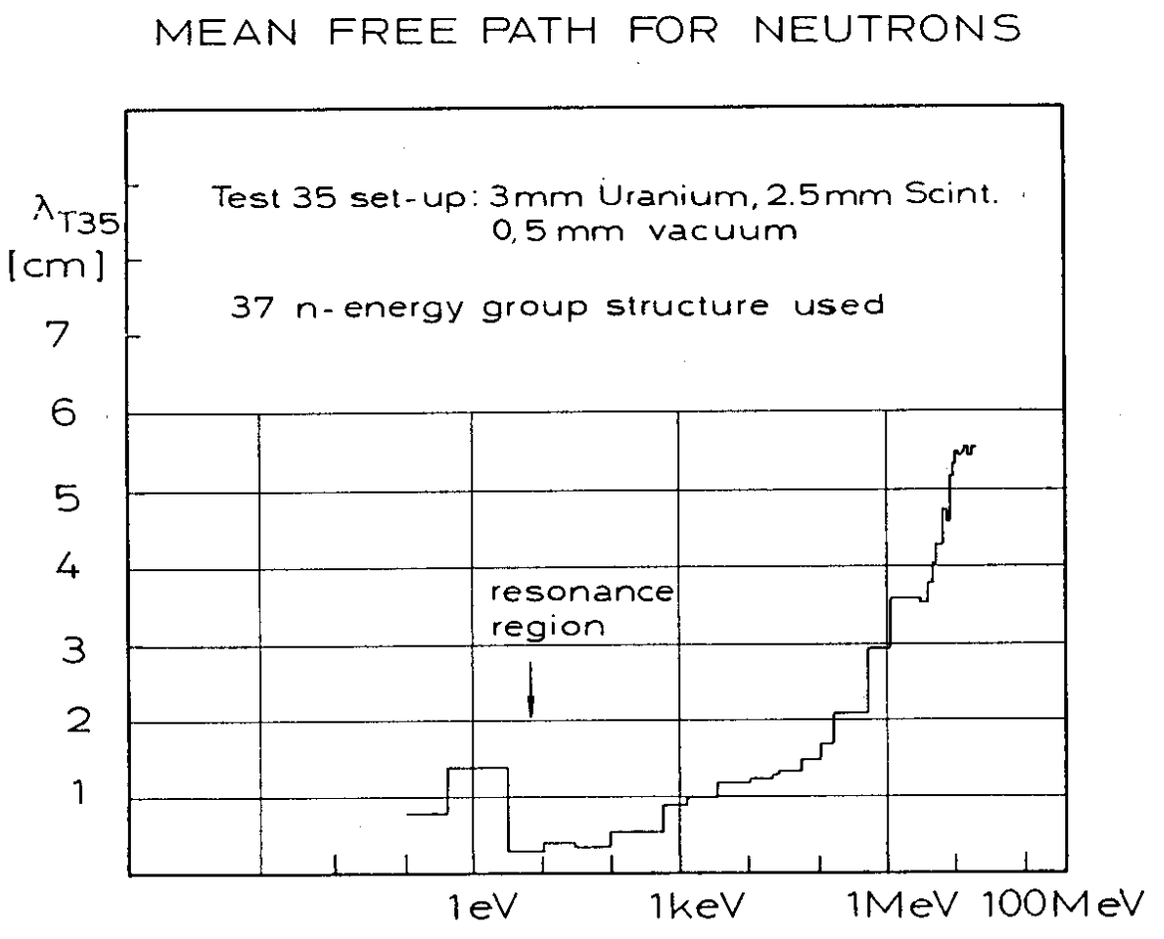


Fig. 20: The mean free path $\lambda$ for neutrons is displayed for a sampling structure. $\lambda(E_n)$ is defined as $\left[\sum_K N_K \sigma_K(E_n)\right]^{-1}$ with $N_K$ = # atoms of kind K per cm³ and $\sigma_K$ = total cross section at $E_n$. The plot is shown in the 37-neutrons energy group structure of the DLC31-data library, described in the text.

DYMO keeps continuously track of the neutron spectra versus time (with the help of computer graphics this can be viewed like a movie) and calculates explicitely the transition rates to specified reactions like hydrogen scattering, neutron capture on U-238 or the cladding material, fast-fission of U-238 or thermal fission of U-235.

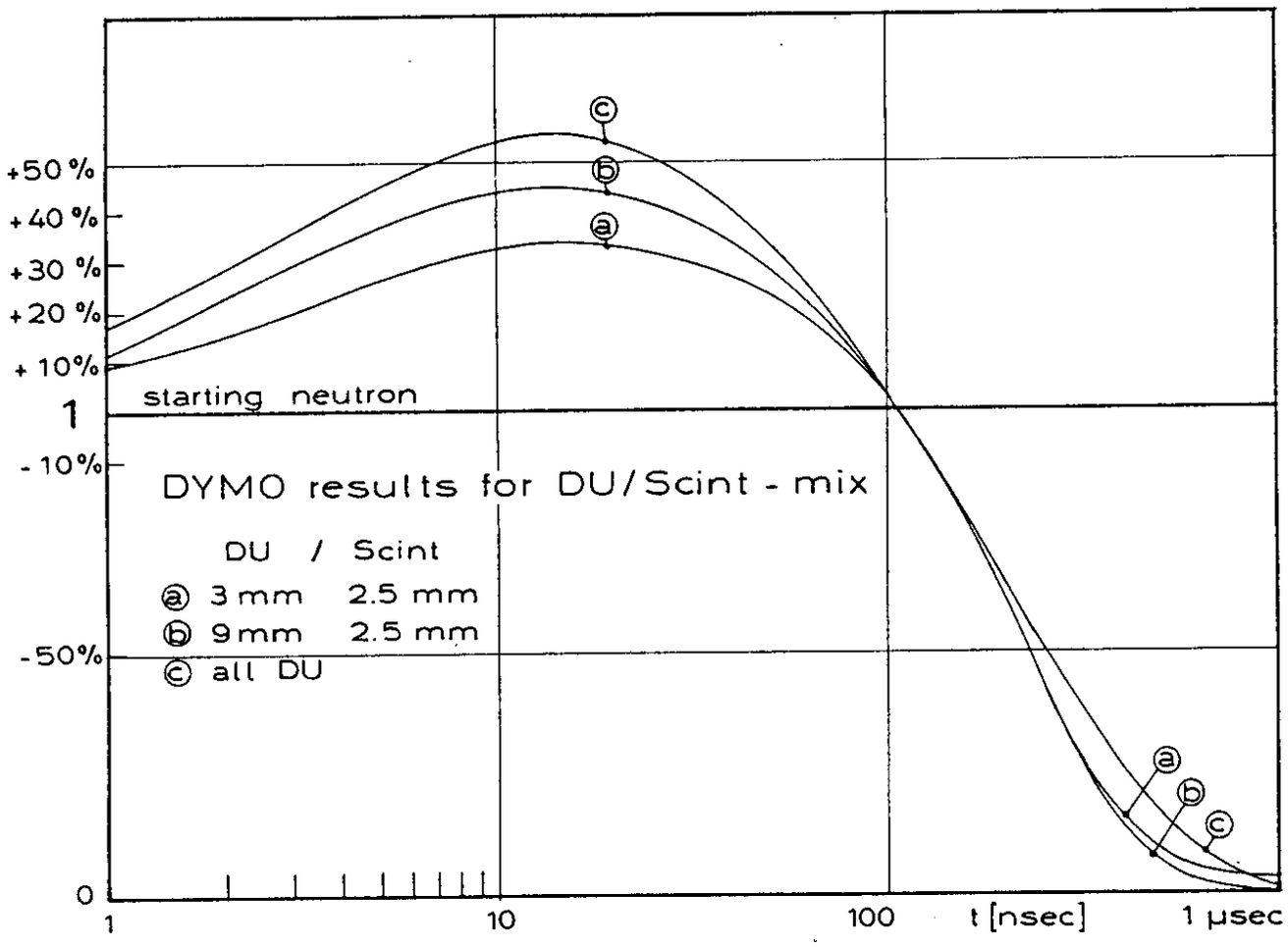


Fig. 21: The sampling calorimeters using DU as absorber material are shown to be multiplicative devices with respect to the number of neutrons produced versus time. But due to the absorption processes, this number drops quickly below 1.

In Fig. 21, the resulting number of neutrons, integrated over all energy groups, is shown versus time. DYMO has been started with 1 neutron at t=0 sec according to the spectrum shown in Fig. 18. This neutron becomes 1.3-1.5 neutrons due to fast fission, (n,2n) and (n,3n) reactions, but in competition with neutron absorption (that is neutron capture in DU). As

expected, the number of neutrons depends on the hydrogeneous content (= scintillator thickness) of the calorimeter compared to the amount of DU. Fortunately, neutron multiplication lasts 20 nsec only, because the neutrons are moderated below the fission threshold of U-238 (Fig. 19) and are captured mostly with decreasing energy. Since also the numbers of Tab. 2 are finite, a hadron sampling calorimeter, build from DU, will never be a "critical" device ($k_{eff} > 1$) in the language of reactor power plants [49].

As an example for the neutron dynamics in a DU/Scintillator stack, the number of fast-fissions, $N_f(t)$, and of neutron captures in U-238, $N_c(t)$, are given in Fig. 22.

The energy dependence of the capture cross section (Fig. 19) is reflected in $N_c(t)$, since the slowing down of neutrons will take some time. The adding of a metallic (copper) cladding will decrease these numbers somewhat, because of absorption processes of neutrons in the copper nuclei.

A small (air-filled) gap between the absorber and the detector layer (tolerance) can be simulated to a certain extent with DYMO by an appropriate reduction factor for the mean density of the whole material mix.

The results of various calculations with DYMO for different calorimeter geometries (that means different material mixes) are shown in Fig. 23 versus the ratio of absorber thickness to scintillator thickness [3,7] on a logarithmic scale.

A linear dependence of the neutron producing and absorbing processes is observed in the range typical for hadron sampling calorimeters ($d_{DU}/d_{Sci}$ = 0.5-2.0). The ratio infinity means a

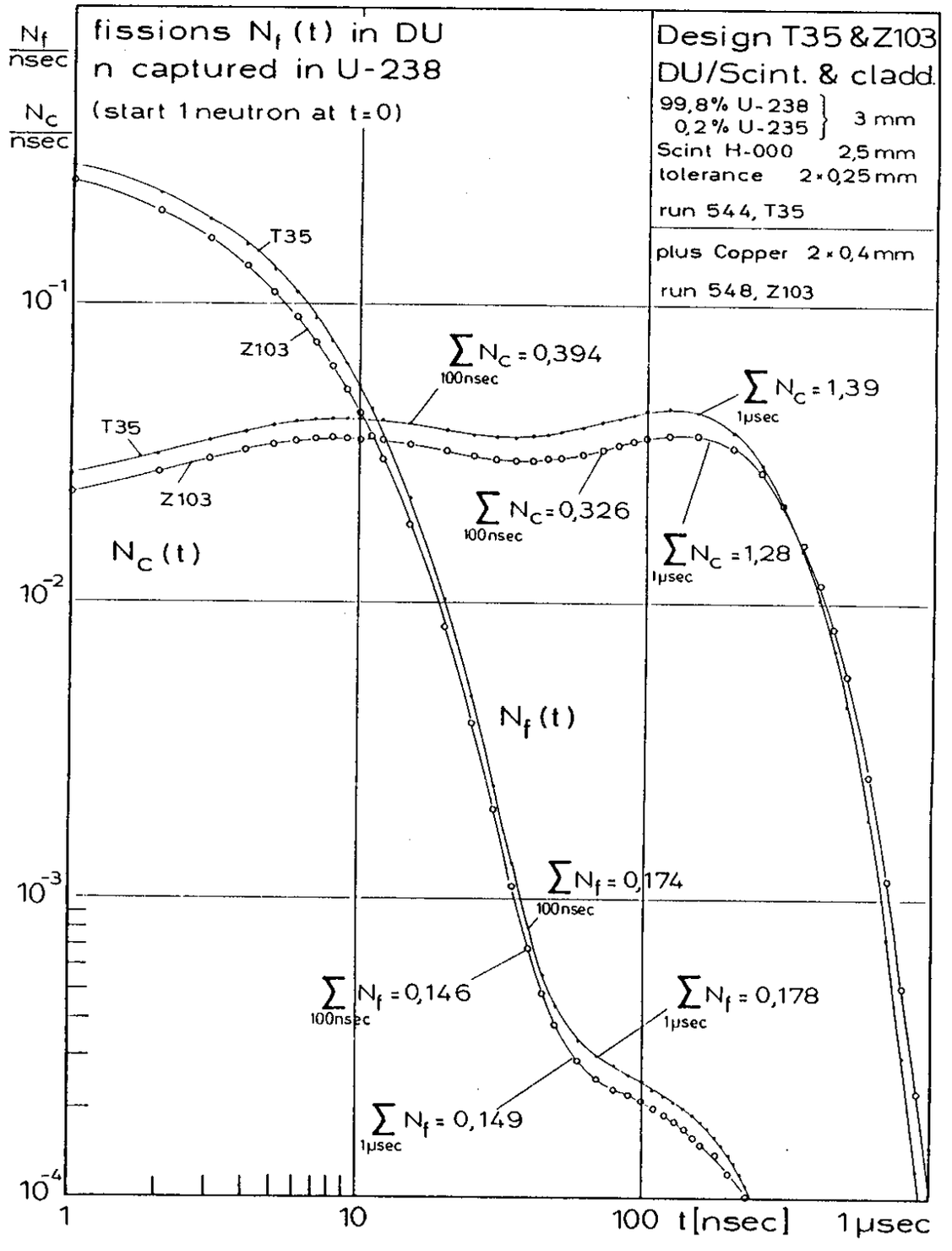


Fig. 22: The number of secondary and tertiary fissions $N_f(t)$ and the U-238 neutron captures $N_c(t)$ versus a logarithmic time scale. Integral numbers after 100 nsec and 1 μsec elapse of time are given for numerical comparison. These numbers are affected by the metallic cladding, due to absorption processes in the copper. The properties of the hypothetical scintillator H-000 are similar to the conventional ones on Polystyrene basis. The C:H ratio is 1:1.

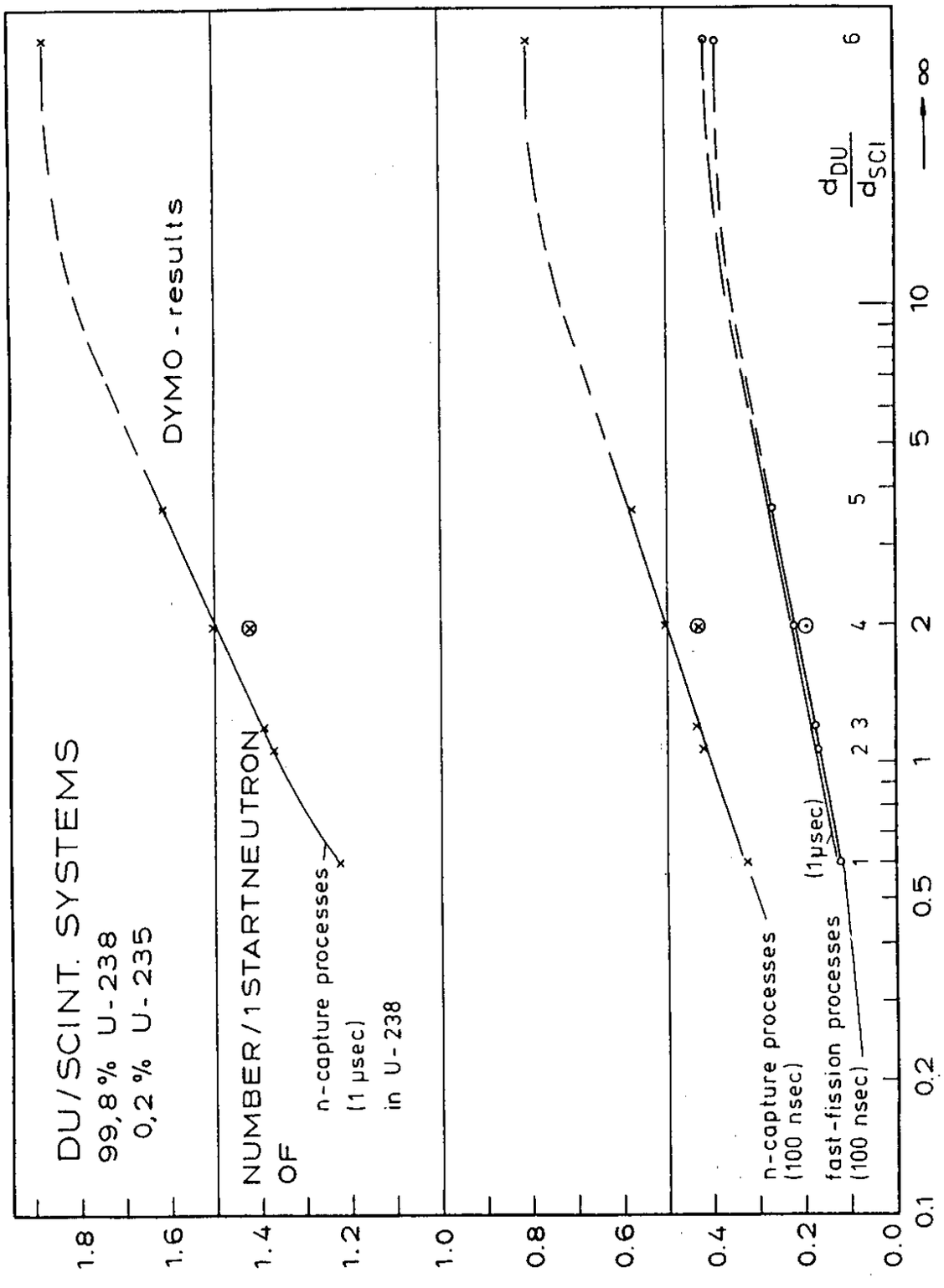


Fig. 23: The number of neutrons captured in U-238 and the fast-fission processes in DU for 100 nsec and 1 µsec after the high-energy cascade has produced the neutron spectrum from Fig. 18. No cladding was used. The circled points at ratio 2 (point number 4) are calculated with a 2×0.5 mm Fe-cladding, included in the material mix. Point number 6 is for pure DU.

purely DU-mix without any scintillator. Due to the large mean free path for neutrons in the mix, the number of processes shown is only a weakly increasing function with increasing thickness ratio (e.g. the number of fast-fissions is only increasing from 0.16 to 0.23 when increasing $d_{DU}/d_{Sci}$ from 1 to 2, i.e. doubling the DU layer thickness for a fixed $d_{Sci}$). Since all calculations with DYMO are normalized to one starting neutron, the resulting number of neutrons for the geometry considered depends on the yield numbers given in Tab. 2.

For the geometries corresponding to points number 3 and 5 in Fig. 23 detailed results are given in Tab. 4a. There has been made an attempt to measure these numbers [37]. A first comparison of the measured values with the calculated ones is given in Tab. 4b. Assuming linear scaling with energy, the agreement is very good within the experimental errors. Because the primary neutron spectrum (used in DYMO for calculating the numbers given in Tab. 4a) is not very dependent on either the energy (2.5 GeV, 10 GeV) or the incident particle ($\pi^-$,p) [9], one can also use the other yields given in Tab. 2 for comparison.

The gamma energy which is released during the fission process and the neutron capture reaction is converted to visible energy only with a small efficiency [7]. This can be calculated by MC methods, using EGS [5], or even simpler by utilizing the ORNL multigroup one-dimensional discrete ordinates neutron/gamma transport code ANISN [26]. A prompt $\gamma$-fission source for U-238, resulting from fast-fission processes [25], is shown in Fig. 24 (curve a), using the 21 gamma-energy group structure. One observes that although the number of gammas is rather high below 0.7 MeV (above group 12, curve a), the energy contribution (with a maximum around 1 MeV, curve b)

10 GeV/c $\pi^-$ on DU-Block (60×60×300) cm

ⓐ

| | 3 mm DU 2.5 mm Scint. 0.5 mm air gap | | 9 mm DU 2.5 mm Scint. | |
|---|---|---|---|---|
| casc.+ evap. n-yield (≤ 20 MeV) (prim.prod.) | 326 | | 326 | |
| fast fission prod. neutrons (sec.+tert. product.) | 0.365×326 = 119 | | 0.535×326 = 175 | |
| prim. fission processes (n(> 20 MeV) and charg.part. induced) | 14 | | 14 | |
| fast (sec.+tert.) fission proc. gate 1 µsec | 0.178×326 = 58 | | 0.271×326 = 88 | |
| total # fissions | 72 | | 102 | |
| n-capture processes in U-238 gate 100 nsec | 0.394×326 = 128 | | 0.574×326 = 187 | |
| n-capture processes in U-238 gate 1 µsec | 1.394×326 = 454 | | 1.612×326 = 526 | |

Tab. 4a: For 10 GeV/c $\pi^-$ incident the calculated (HET-KFA/DYMO) particle production, fission and n-capture in U-238.

ⓑ

| | normalized per GeV | Exp.* per GeV | normalized per GeV | Exp.* per GeV |
|---|---|---|---|---|
| total # fissions | 7.2 | 8.0±1.1 | 10.2 | 8.9±1.2 |
| n-capture processes in U-238 gate 1 µsec | 45.4 | 47±8 | 52.6 | 51±13 |

* Experimental numbers generated per 591 MeV proton and extrapolated per GeV [37].

Tab. 4b: Comparison of calculated results for 10 GeV/c $\pi^-$ with recently published experimental data [37]. The calculated numbers have been normalized per GeV assuming to first order linearity between numbers and energy incident.

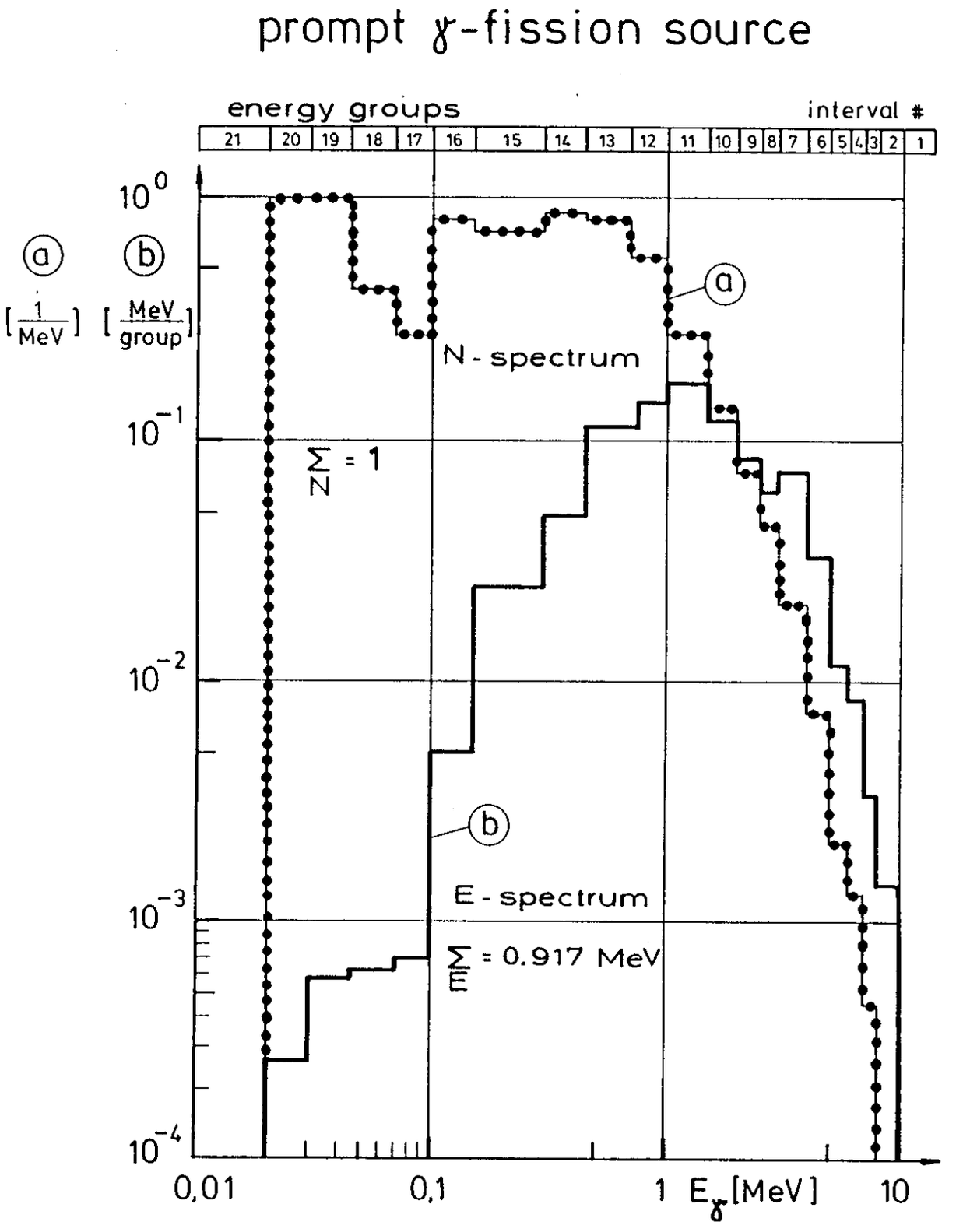


Fig. 24: Prompt gamma fission source. A double logarithmic scale is used.

a) Number of γ's per MeV, $N(E_\gamma)$, normalized to one.

b) γ-energy, $E(E_\gamma) = N_g \cdot \overline{E_g}$ in MeV per group; the sum is 0.9165 MeV for the spectrum.

falls steeply by more than two orders of magnitude to zero at 20 keV.

With the properly weighted material cross sections for photo-, Compton- and pair reactions, ANISN is able to solve the Boltzmann transport equation for the gamma flux by a numerical iteration method without transporting the secondary produced charged particles, of course. Since the fission gamma source carries its maximum energy by 1 MeV photons mostly (thus the Compton effect dominates the Kinetic Energy Released to Matter, KERMA), the energy absorbed (or deposited) in the scintillator was calculated by multiplying the resulting flux distribution with the appropriate mean-energy per group. Fig. 25 gives a result for a 3 mm DU/2.5 mm scintillator sampling structure, using a CU-cladding or an air gap between the layers. As mentioned already in the context of Fig. 10, a homogeneously distributed fission-source (normalized to one gamma per $cm^2$ and sec) was assumed to be located in one uranium sheet (dashed area in Fig. 25).

Setting the energy content equal to 100% (= 0.9165 MeV for the fission source used, Fig. 24), the migration of $\gamma$-energy (as discussed above) into the absorber layers is clearly visible. Most of the energy released by fission processes is absorbed in the source layer itself (37%) and can thus not contribute to the detector signal [7]. The summed fraction of deposited and visible fission energy (the gamma sampling fraction $\gamma_{fiss}$) for the structure shown in Fig. 25 is only 2.2% and 2.0% (with the Cu-cladding) resulting in $\gamma_{fiss}$/mip = 0.29 and 0.30, respectively. Since the total number of fissions is known (column 2 in Tab. 4a), one can calculate the total amount of released fission energy. Knowing that on average 7

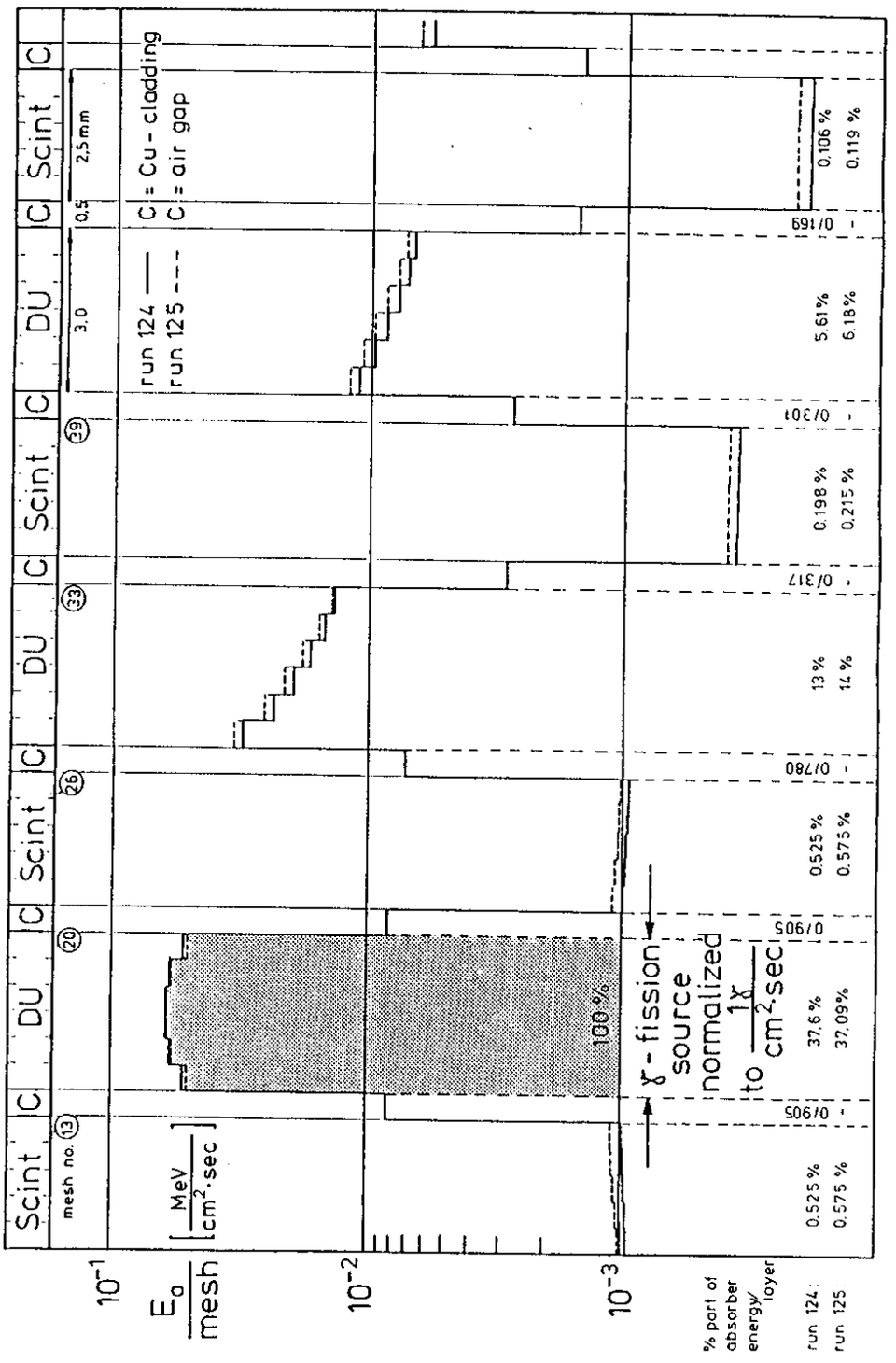


Fig. 25: The absorbed energy per mesh (mesh size = 0.5 mm) in a DU/Scintillator (SCSN 38) structure. Two calculations were made, run 125 without any cladding (dashed curve) and run 124 with a Cu-cladding (solid curve). The corresponding mip value is 7.6% and 6.6%, respectively. The accuracy for balancing the iteratice code ANISN was $10^{-4}$. The fraction of absorbed energy per layer is indicated in the lowest two rows.

prompt $\gamma$'s are released per fission [49], one finds: $7 \times 0.917$ MeV $\times$ 72 = 462 MeV in 1 µsec gate time, from which only $462 \times 0.022$ = 10 MeV are "visible" in the detector layers.

The same calculation can be performed for the gamma energy released by neutron capture in U-238. Assuming the sampling fraction $\gamma_{capt} = \gamma_{fiss}$ (since all the gamma spectra originates from nuclear deexcitation) and knowing that no more than the binding energy of a neutron in U-238 can be released (that is 4.8 MeV), one finds (see Tab. 4a): 4.8 MeV $\times$ 128 (454) = 614 (2179) MeV in 100 nsec (1 µsec) or, more importantly, 14 (48) MeV "visible" for the T35 structure considered.

These numbers are only slightly higher for a LA-detector [3]. This makes it impossible to build DU/pure LA compensated sampling calorimeters [7], as already discussed in [3] and [5].

There is a third source of gamma energy not considered so far. Its physical origin lies in the gamma-ray spectra following nuclear reactions, other than fission or neutron capture. If the evaporation of hadrons (as discussed in I.4) is no longer possible for the excited residual nuclei (for which at least around 7 MeV binding energy has to be provided), the nucleus will deexcite further by gamma emission. The amount of $\gamma$-energy, which can be made visible for those nuclei remaining in the cascade without undergoing a fission process, was estimated to be 1 MeV, which should be added to the 10 MeV, calculated before for the fission contribution. A non-elastic nuclear reaction, induced by the low energy neutrons released during the high energy cascade, can also produce deexcitation gamma energy [53]. Though it is possible with DYMO (used so far for the low-energy neutron transport) to couple the 21 gamma energy groups from the DLC31-Data Library with the 37 neutron

energy groups (thus gaining a neutron induced gamma source, which had to be transported with the geometry dependent ANISN code, analog to the prompt fission gamma source), such an elaborate calculation has not been performed until now. It would be more reliable to get this information from a coupled neutron/gamma transport calculation with the 3-dim. MORSE code. A discussion of this point can be found in [42].

As shown also in [3] and [5], the major contribution to the compensation signal for hydrogeneous detector materials like scintillator or TMS/TMP comes from the neutron kinetic energy transfered in recoiling protons. In Fig. 26 the results from DYMO, which are calculated using a homogeneous mix out of the T35 calorimeter material, are compared with a 3-dim. MC calculation, taking the sampling structure explicit into account. The MORSE-CG version KFA-IRE [50] was used to calculate the recoil energy for 3 (out of the 37) n-energy groups, thus simulating "monoenergetic" neutron sources (broken lines in Fig. 26, labelled "het"). Also a MORSE calculation was performed using the DYMO material mix (extra solid lines labelled "mix"). As expected from the large mean free path of the neutrons (Fig. 20), there is only a small difference between these results, when only isotropic scattering data are used in MORSE (set labelled $P_o$), as is the case for DYMO, too. These results coincide very well with the upper DYMO curve, calculated for 5 separate groups. The MORSE code can take anisotropic scattering cross section data up to the 8th order of a Legendre expansion into account. This anisotropy shows up only at the highest neutron energies in Fig. 26, lowering the isotropic results somehow (set labelled $P_5$ for a 5th order Legendre expansion). For DYMO, a surface loss correction can be taken into considera-

tion, accounting for the fractional loss of those recoil protons, which receive enough recoil energy to escape from the scintillator layer into the absorber. Since there are no real layers in DYMO, this correction applies only for the mean (lower curve). From Fig. 26 also the neutron sampling fraction $n_{Ekin}$ (due to visible proton recoil energy) can be read off. A line for $n_{Ekin}$ = 10% is shown for illustration. This is more than the mip sampling fraction of 7.6% and therefore can help substantially to achieve full compensation (see next chapter).

The saturation effect of the scintillator was included in the evaluation of the visible proton recoil energy $E_{vis,p}$. In case of organic scintillator, the saturation is described by the kB-parameter in the Birks formula [51], Fig. 27. The kB values from [52] are given in Fig. 27 and had been used for the calculations:

$$\frac{dL}{dx} = \frac{s \cdot dW/dx}{1 + kB \cdot dE/dx} \qquad (7)$$

with dE = diff. energy-loss of particle

dL = diff. light output

s = proportional constant for electrons (kB = 0).

The signal is strongly affected by saturation effects in the energy range considered.

In Fig. 28, the MORSE code with anisotropic scattering was run with different time-cuts and a starting one-neutron spectrum according to Fig. 18. Since this is very CPU time consuming, a homogeneous mix (with Cu-cladding) was used only. The agreement with DYMO (using the surface loss correction) is also very good. The difference near t=0 is not unexpected, since in DYMO the starting neutron is also homogeneously distributed in space, whereas in MORSE it starts as a point source in the middle of the block.

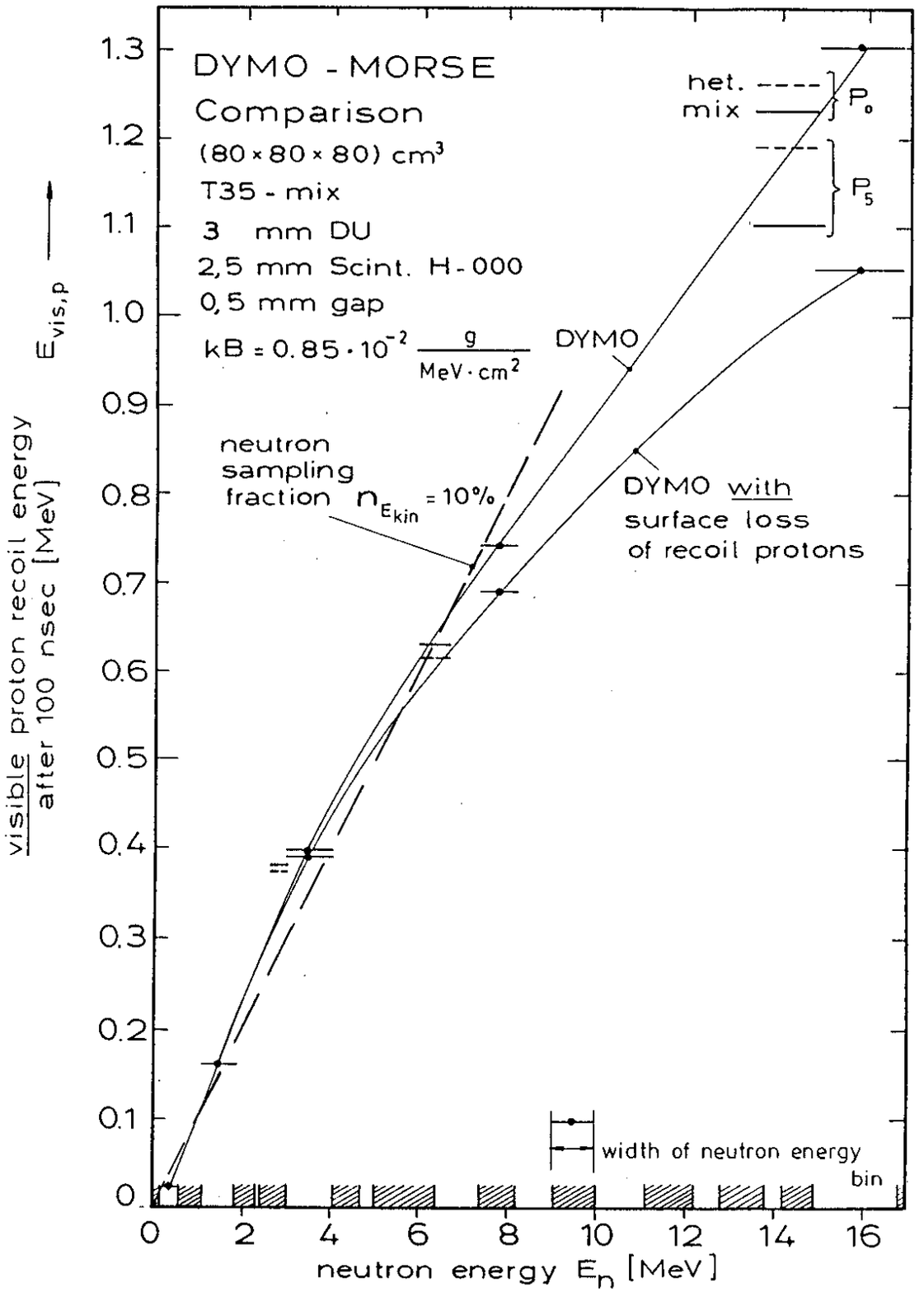


Fig. 26: A code comparison for neutron transport was made for a T35 homogeneous calorimeter material mix and a T35 real geometrical sampling structure. In separate runs, a quasi monoenergetic neutron was started for three (MORSE) or five (DYMO) neutron energy groups. The whole group structure is indicated above the neutron energy axis $E_n$. The proton recoil energy visible after 100 nsec (taking saturation into account) is compared, see text.

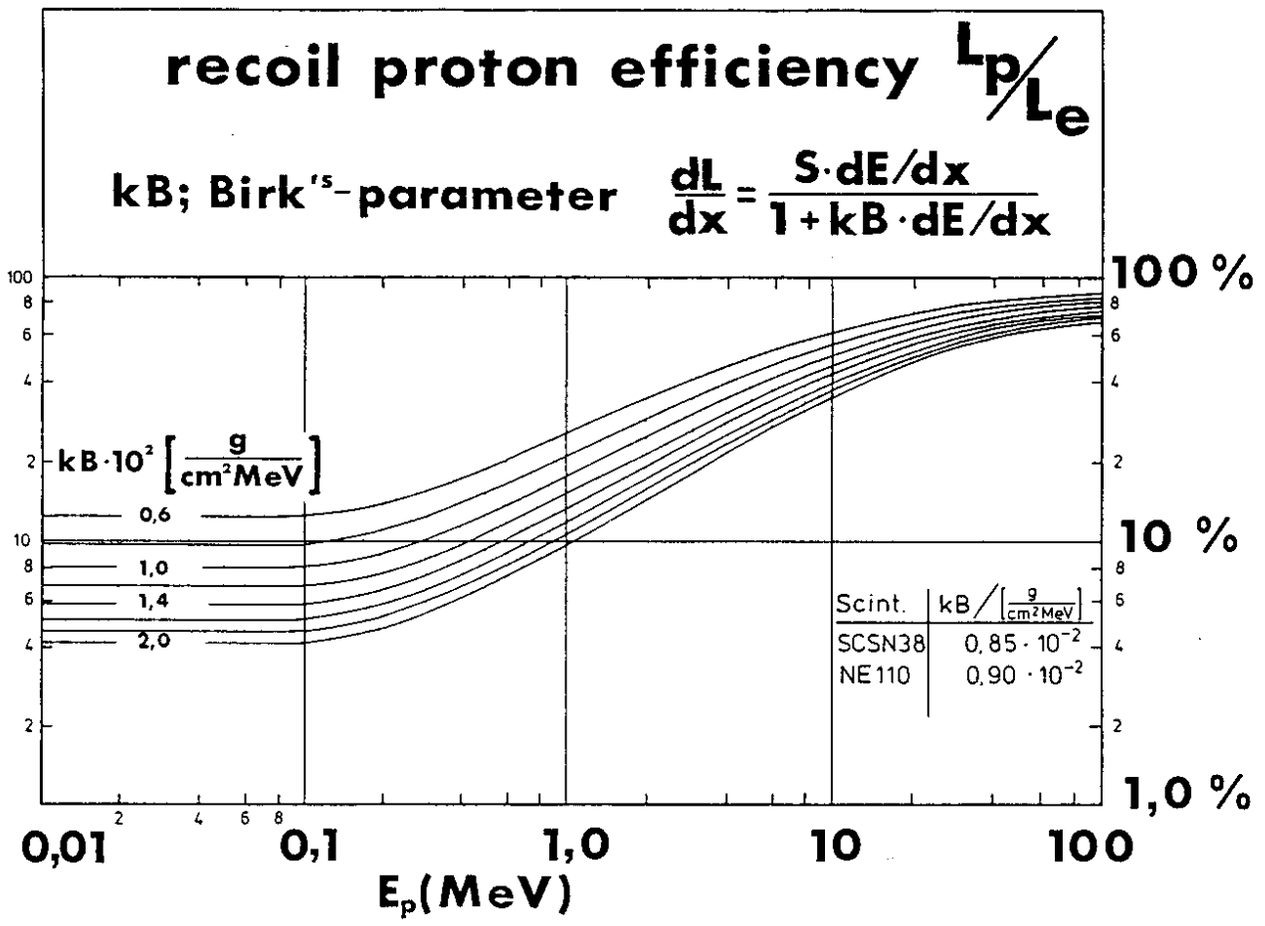


Fig. 27: The conversion efficiency of proton recoil energy to signal, as described by the kB-parameter in the Birk's formula. E stands for energy-loss of particle, L is the light output and S a (read-out specific) proportional constant between L and E, (taken as 1 in the calculations).

In order to show the contribution of the different processes (connected with low-energy neutron transport) to the visible energy, again a lethargy plot is shown in Fig. 29 for $[t \cdot E_{vis}]$. The dashed area shows the normalization of the unit area to 10 keV visible energy. Almost all contributions from the recoiling proton can be made visible within the HERA bunch crossing time of 96 nsec. The integrated area for $E_{vis,p}$ recoil is 0.280 MeV (and 0.329 MeV for the calculation without cladding).

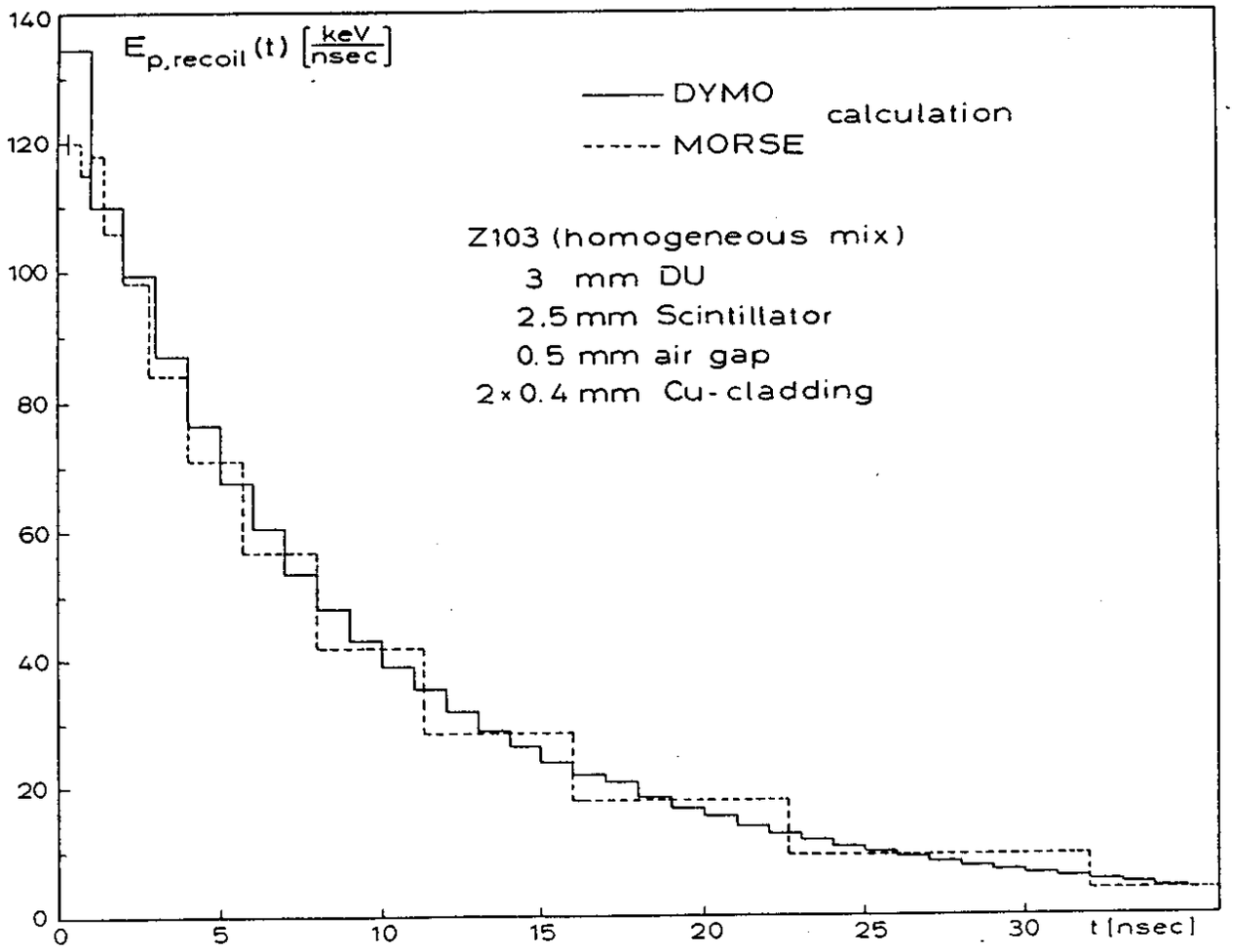


Fig. 28: A time-dependent MORSE calculation is compared to the evaluation of dynamics with DYMO. The calorimeter contains a homogeneous mix of materials and one neutron is started at t=0 with a spectrum, normalized to one, according to Fig. 18.

This is a 24% reduction compared to the deposited (KERMA-value) energy in the scintillator. The resulting n/mip is 1.19 and 1.23, respectively, since the (mean) amount of neutron energy, going into the calculation, is 3.54 MeV as indicated in Fig. 18. The $\gamma$-contribution, also smaller in area, is only important for t > 200 nsec. A similar plot for DU/LA calorimeters is given in [3] but is not discussed here again.

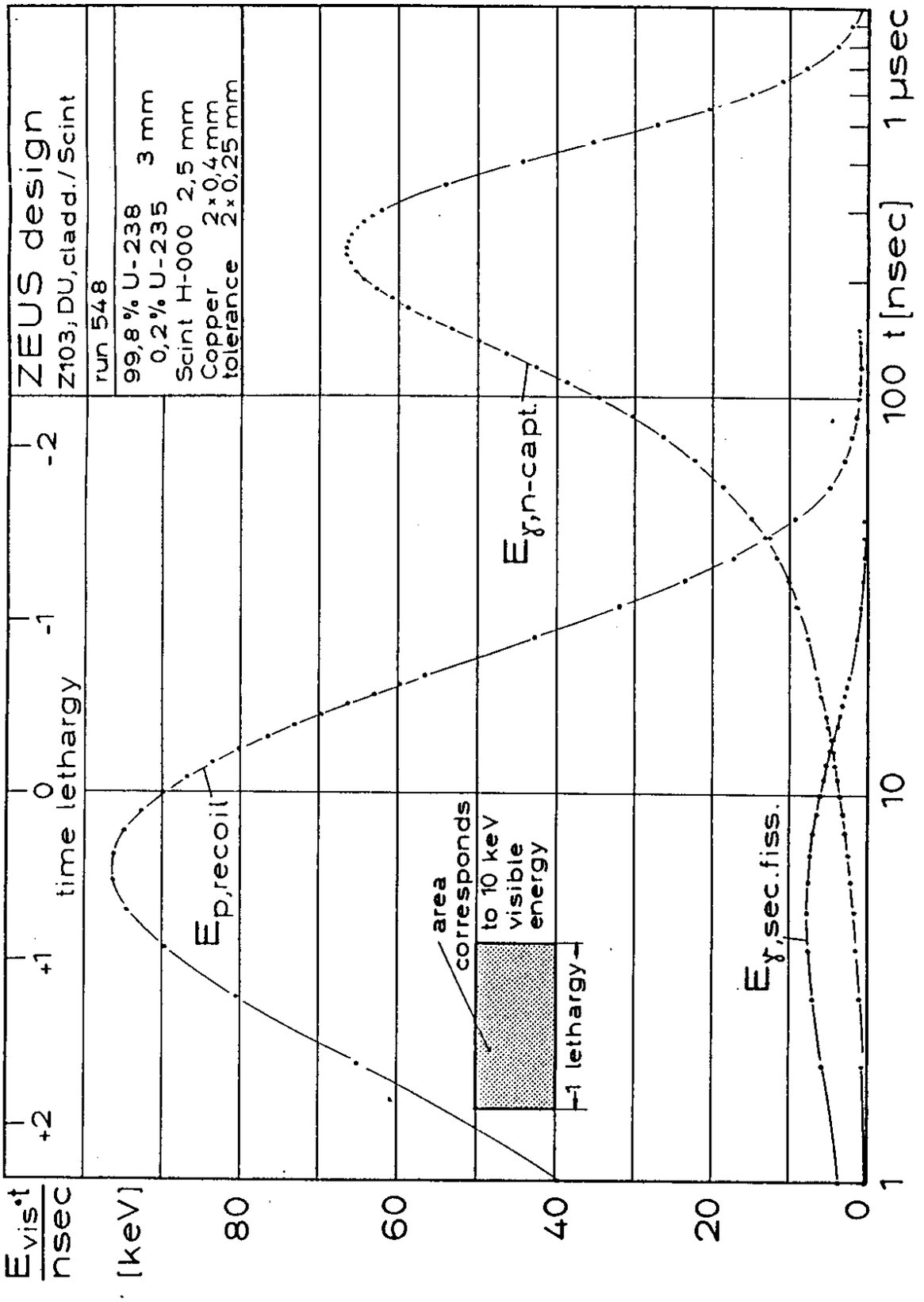


Fig. 29: The contributions to "visible" energy from proton recoils and from the nuclear processes in DU. In this lethargy-plot, the area is directly proportional to the amount of energy contributed, see text in connection to Fig. 18.

## II. Comparison with Test Results

### II.1. e/h Ratios

Up to now in comparing the MC calculations for hadronic calorimeters with experimental data, the emphasis has been on e/h-ratios, [8]. The computer code HERMES, developed by our group, is displayed in Fig. 30. SIM-KFA is an analysis code to prepare the propper input from the HETC MC histories for the other codes; this could be the low energy neutron yields (see Tab. 2 and 3) or the energy created in a HETC run either by $\pi^0$-particles ($E_{sub,\pi^0}$) or by low energy neutrons $E_{sub,n}$).
Since alle other codes have been discussed already, only a summary is given of the physics input required to predict e/h-ratios (see also Fig. 31). Five very different types of processes have to be distinguished:

1.) Incident or internally created electromagnetic particles ($\gamma, e^{\pm}, \pi^0$), which give rise to an electromagnetic shower. Due to the migration of $\gamma$-energy, e/mip can be considerably smaller than one for high-Z absorber materials.

2.) Energy deposition by $(\frac{dE}{dx})$-ionization energy loss of high-energetic charged particles like $\mu^{\pm}, \pi^{\pm}$,p etc. Both processes 1.) and 2.) are taken into account in the calculations according to the sampling fraction of the ionizing part of the hadronic shower $h_i$, introduced in chap. I.1, and further explained in the next paragraph.

3.) Fission processes of high-Z nuclei, which might be prompt, when induced by high energy hadrons (high energy fission) or delayed if induced by the low energy neutrons (fast fission).

4.) Release and possible detection of neutrons if hydrogenous detector material is present. Neutrons in the energy range of several MeV's, called low energy neutrons with an upper

energy limit of 15 or 20 MeV. Neutrons created with high energies are either leaking out of the calorimeter structure (their contribution via elastic scattering of protons to the energy deposition is included in 2. and accounted for in $h_i$, if instead of a DU-block a real calorimeter sandwich structure is calculated with HET-KFA) or are scattered below the low energy threshold. The low energy neutrons, of course, in a real calorimeter can also leak out. This can only be studied by using the geometry dependent MORSE code, whereas DYMO (by definition of the homogeneous mix) can simulate a small leakage only by reducing the mean density of the mix, corresponding to the air gap size within the calorimeter.

5.) Prompt nuclear gamma radiation emitted from the excited fission and non-fission products of the high energy cascade (after particle evaporation) as well as delayed gamma radiation from neutron induced nuclear reactions during the moderation process; most important: fast fission and neutron capture.

In a standard calorimeter the response for electrons is greater than for hadrons [8]. In order to achieve compensation, see Fig. 2, one has to enhance the hadron signal via detection of neutron- and gamma-interactions. This will depend strongly on the choice of absorber and detector materials and on the layer thicknesses. DU/Scintillator (or similar) systems offer the unique possibility to tune for full compensation, e/h = 1, [7]. The sampling fraction due to proton recoil, $n_{E_{kin}}$, does not scale with the mip sampling fraction, which has almost half the value when the ratio of thickness $d_{abs}/d_{sci}$ is doubled, whereas n is only decreased by the factor 0.8, [9]. Thus n/mip is a strongly increasing function with increasing thickness ratio, see Fig. 32, whereas e/mip and $\gamma$/mip are almost constant.

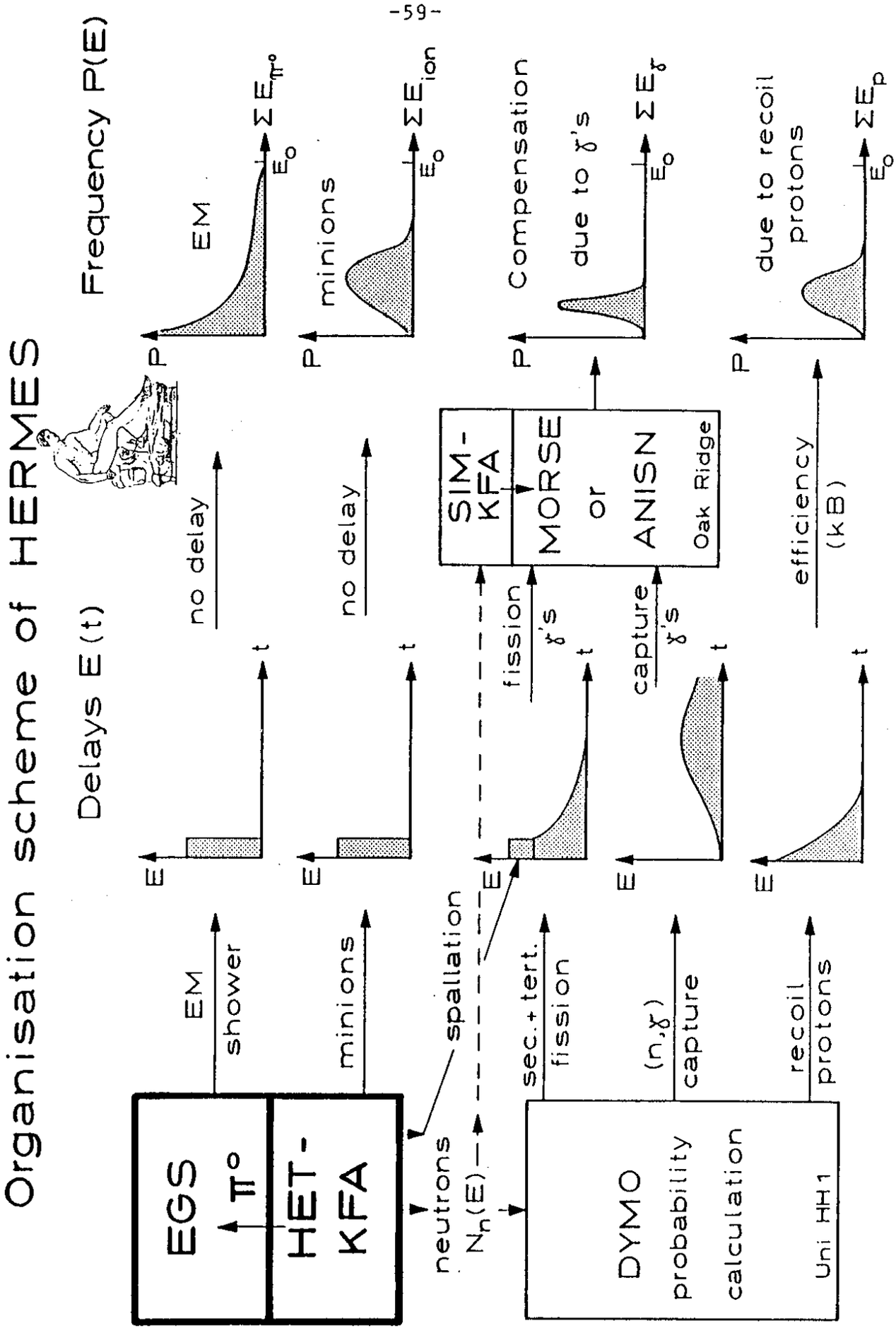


Fig. 30: The organization scheme of the HERMES (High Energy Reaction Models for Elaborate Simulations) code.

# Some Important Physics of Sampling Hadron Calorimetry

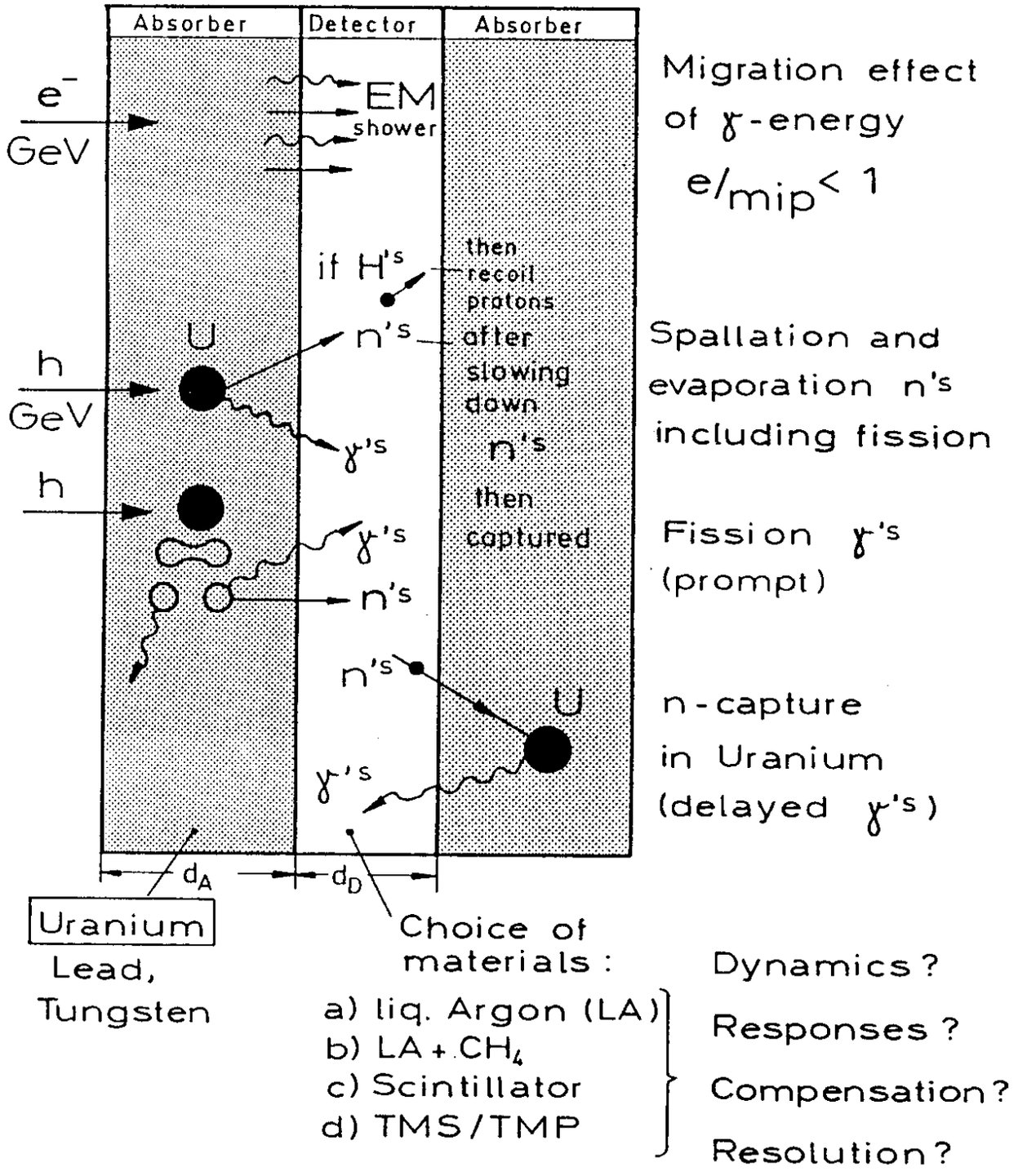


Fig. 31: The important effects, which are involved in the physics of compensating sampling calorimeters, are visualized schematically. The main emphasis lies on the production of neutrons and gammas in uranium absorber plates.

The calculations shown in Fig. 32 were performed for various experimental tests in connection with the development of the ZEUS detector, [54]. The results from the points 1-4 from Fig. 23 correspond to T60A, T60B, T35 and "WA78" (which stands for test WA78/HERA without Fe-cladding). For details on the tests, see Tab. 5 and [54].

According to relation (4), e/h-ratios can now be calculated. As an example, we write for

$$C_{T35} = \frac{E^{vis}_{recoil} + E^{vis}_{fiss.+deex.} + E^{vis}_{capt.}}{(\frac{e}{mip} - \frac{h_i}{mip}) \cdot E_o \cdot mip} \qquad (8)$$

$$= \frac{326 \times 0.329 \text{ MeV} + 11 \text{ MeV} + 14 \text{ MeV}}{(0.60-0.41) \cdot 760 \text{ MeV}}$$

$$= \frac{132}{144} = 0.917 \text{ for the } (60\times60\times300) \text{ cm block}$$

(and = 0.946 for the (ø 300×300) cm cylinder),

resulting in $\frac{e}{h} = 1.03$ and 1.02, respectively.

The results for the other tests are given in graphical form in Fig. 33 for C and in Fig. 34 for e/h. All results, together with other numbers used, are summarized in Tab. 6. Comparing the calculations (all done for a 60×60×300 cm geometry and for 100 nsec gate time) with the experimental data requires some caution, since the various test setups (all equipped with 60×60 cm² plates) differ in the total depth.

Furthermore the calculations assume that the signals are read-out uniformly, which is not the case for the raw data of the experiments. Calculations of corrections, treating the longitudinal and transversal leakage and a uniform read-out are in preparation [54]. On the other hand, also the calculations need some conformation, specially on the e/mip values (see chap. I.3). A 7% increase in these values (using non standard options in EGS) will decrease the C-value and increase

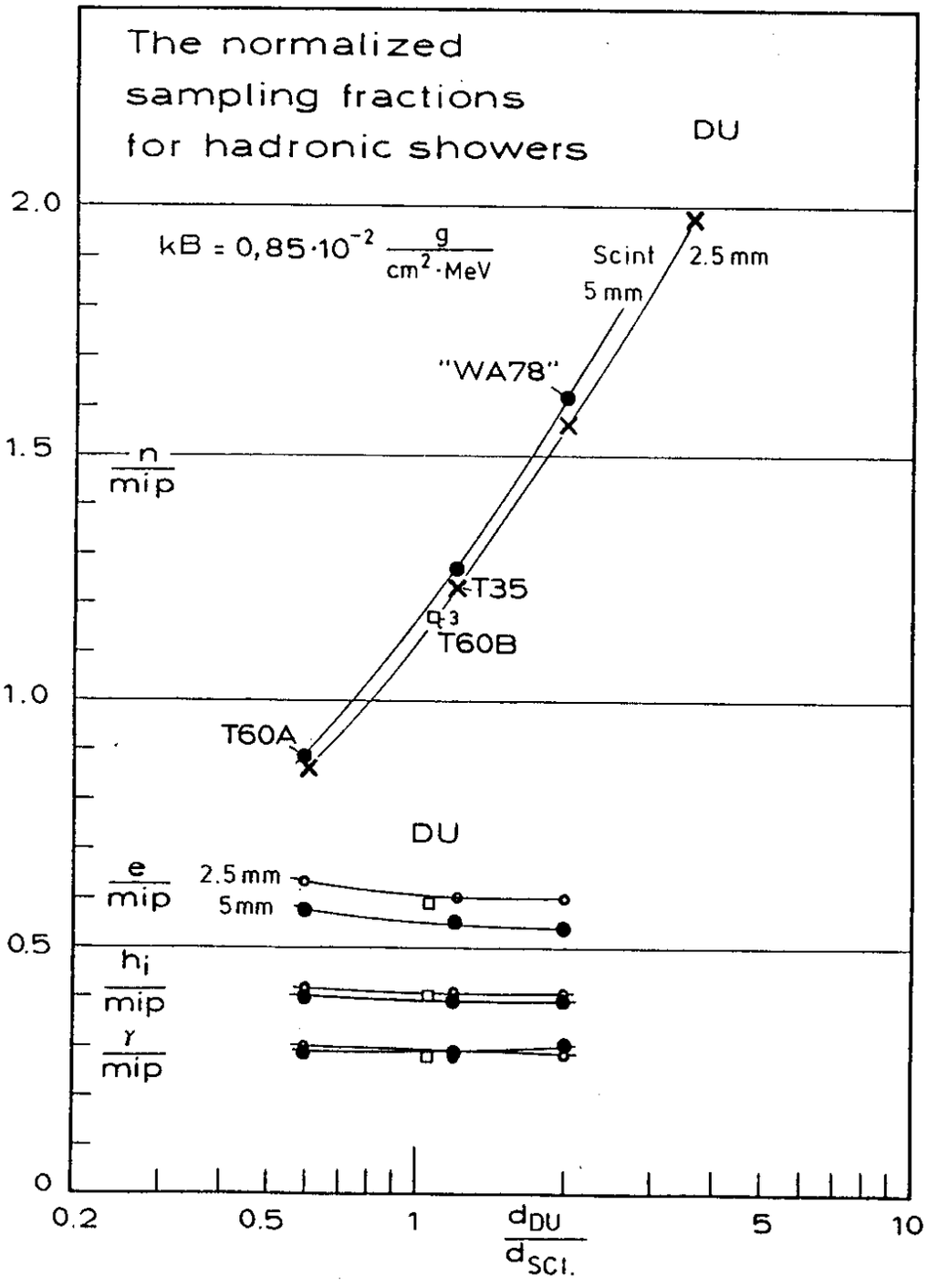


Fig. 32: The normalized sampling fractions, which determine the e/h-ratio of DU/Scintillator systems,are given for various test calorimeters, abbreviated T60A, T60B, T35 and "WA78", see text. The decreased n/mip for the smaller scintillator is due to enhanced surface losses for the high energetic recoil protons, according to DYMO.

| Name | WA 78/HERA | T35 | T60A | T60B |
|---|---|---|---|---|
| d(DU) | 10 mm | 3 mm | 3.2 mm | 3.2 mm |
| d(SCI) | 5 mm NE110 | 2.5 mm SCSN38 | 5 mm SCSN38 | 3 mm SCSN38 |
| depth | 5.5λ + back | 4.2λ | 4.4λ | 6.0λ + back |
| area | 60×60 $cm^2$ | 60×60$cm^2$ | 60×60$cm^2$ | 60×60 $cm^2$ |
| effective λ | 19.1 cm | 18.2 cm | 33.3 cm | 25.7 cm |
| trans.segmentation | 60×60 $cm^2$ | 20×20$cm^2$ | 5×60 $cm^2$ | 5×60 $cm^2$ |
| long.segmentation | 0.45 λ | 4.2 λ | 1.1 λ | 1.5 λ |
| energy range | 5-210 GeV | 3-9 GeV | 3-9 GeV | 10-100 GeV |

Table 5: Uranium Scintillator Test Calorimeters

e/h by up to 5% (see Tab. 6, column Z103*). Note also,hadronic energy, released by gamma radiation following low energy neutron induced nuclear reactions, which has been neglected so far, would help to slow down this increase.

With all these shortcomings (both in the experimental analysis and in the calculations) one can state that the experimental results are well reproduced by the calculations.

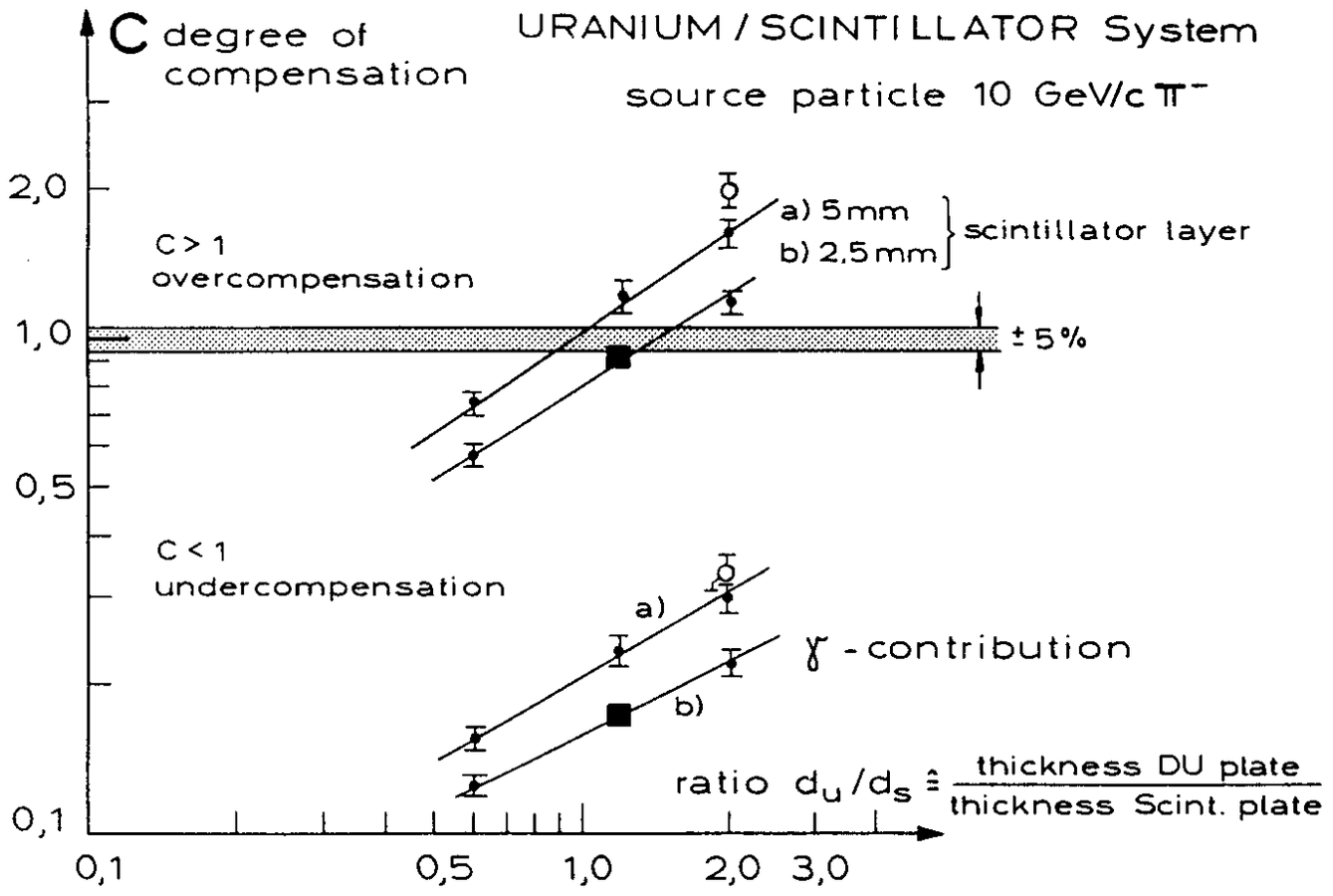


Fig. 33: The degree of compensation C for uranium/scintillator calorimeters. Tuning of C can be achieved by varying the thickness ratio. Calculations have been carried out for SCSN 38 scintillators. The open circle denote the results of a calculation with 2×1 mm Fe cladding on the uranium layers to compare with the WA78/HERA [55] experiment. In the WA78 experiment a different scintillator material (NE110) has been used and hence was also used for the calculations [58].

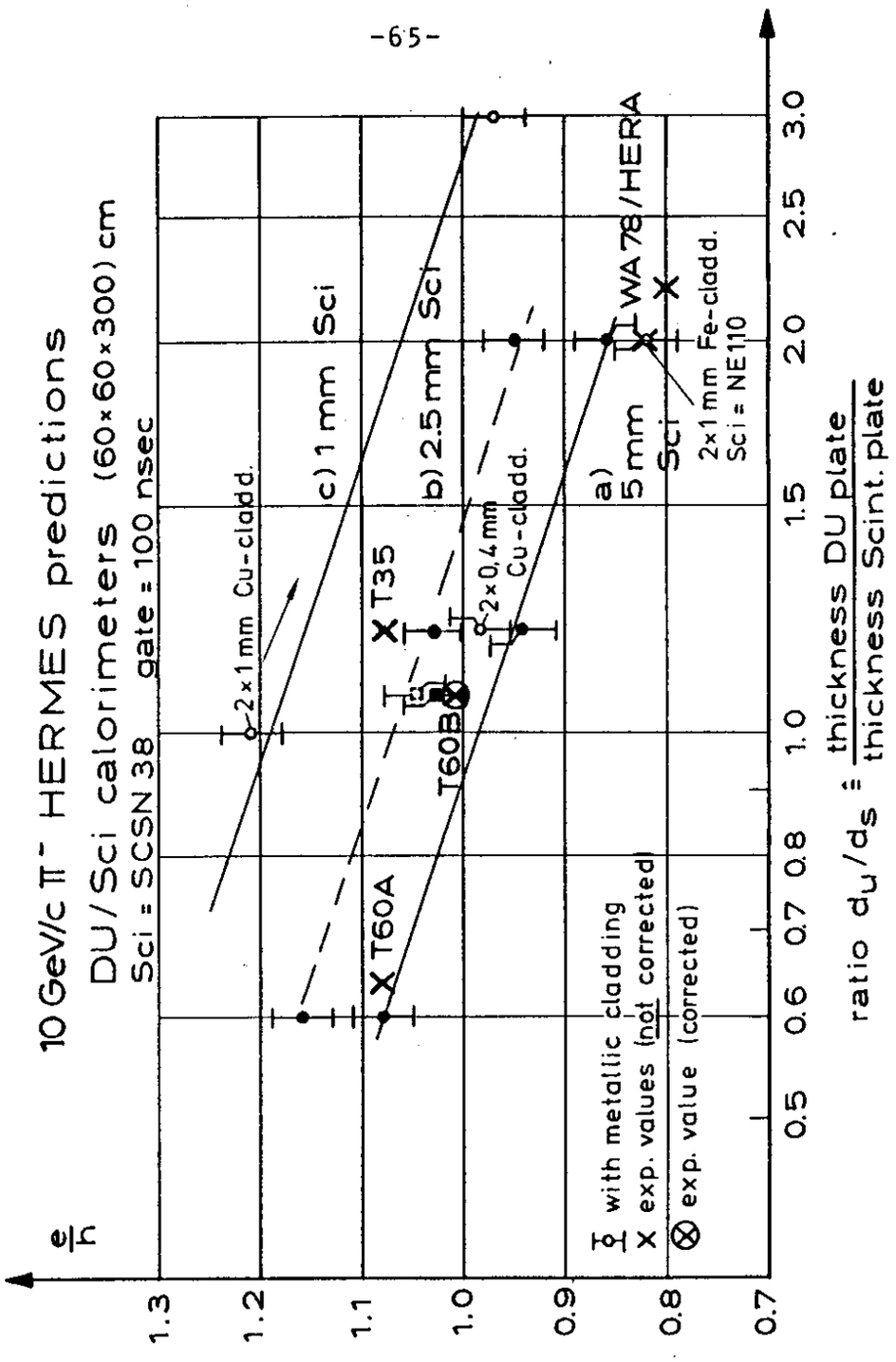


Fig. 34: The experimentally measured e/h-ratios for various test experiments are compared with HERMES predictions, based on mean value calculations. Curve a) corresponds to 5 mm, b) to 2.5 mm and c) to 1 mm scintillator thickness. The points marked by the squares are for 3 mm thick scintillators. The black square gives the "no-leakage" calculation with DYMO; the broken line square takes a reduction of the mean density due to air gaps (2×1.4 mm) into account, see Tab. 5, column T60B.

10 GeV/c $\pi^-$ HERMES Predictions for Mean Values
Absorber Block (60×60×300) cm
still side and front leak for primary produced neutrons

| ZEUS Test | T35 | Z103 | Z103* | T60A | T60B | T60B | WA78-HERA |
|---|---|---|---|---|---|---|---|
| geometry/mm | 3.0 DU<br>2×0.25 gap<br>2.5 SCSN | 3.0 DU<br>2×0.4 CU<br>2×0.25 gap<br>2.5 SCSN | 3.0 DU<br>2×0.4 CU<br>2×0.25 gap<br>2.5 SCSN | 3.0 DU<br>no gap<br>5 SCSN | 3.2 DU<br>no gap<br>3 SCSN | 3.2 DU<br>2×1.4 gap<br>3 SCSN | 10 DU<br>2×1 Fe cladd.<br>no gap<br>5 NE110 |
| mean density $\langle\rho\rangle/\frac{g}{cm^3}$ | 9.91 | 9.80 | 9.80 | 7.73 | 10.29 | 7.09 | 12.38 |
| mip | 7.6% | 6.6% | 6.6% | 14.1% | 8.5% | 8.5% | 4.2% |
| e/mip | 0.60 | 0.56 | 0.60* | 0.574 | 0.59 | 0.59 | 0.50 |
| $h_1$/mip | 0.41 | 0.40 | 0.41 | 0.40 | 0.405 | 0.405 | 0.39 |
| signal needed for full comp. $(e-h_1)E_o$ | 144 MeV | 106 MeV | 125 MeV | 246 MeV | 156MeV | 156 MeV | 46 MeV |
| $\gamma$/mip | 0.28 | 0.30 | 0.30 | 0.29 | 0.28 | 0.28 | 0.29 |
| neutron sampling fraction n | 9.32% | 7.88% | 7.88% | 12.57% | 9.89% | 9.69% | 6.72% |
| n/mip | 1.23 | 1.19 | 1.19 | 0.891 | 1.17 | 1.15 | 1.60 |
| degree of compensation C | 0.917 | 1.05 | 0.89 | 0.744 | 0.913 | 0.865 | 2.02 |
| e/h | 1.03 | 0.99 | 1.036 | 1.08 | 1.03 | 1.05 | 0.82 |

gate width: 100 nsec for all calculations
* EGS3 non-standard step size algorithm, ESTEPE = 0.5%

Tab. 6: Summary of numbers used in the HERMES predictions for various test set-ups in the course of the ZEUS detector development.
Standard cuts and the default stepsize algorithm from EGS3 have been used, except the column Z103*.
A kB-parameter of $0.85 \cdot 10^{-2}$ g/cm²·MeV was taken for all tests, except WA78-HERA, where NE110 scintillator material [58] with kB = $0.90 \cdot 10^{-2}$ g/cm²·MeV was used.

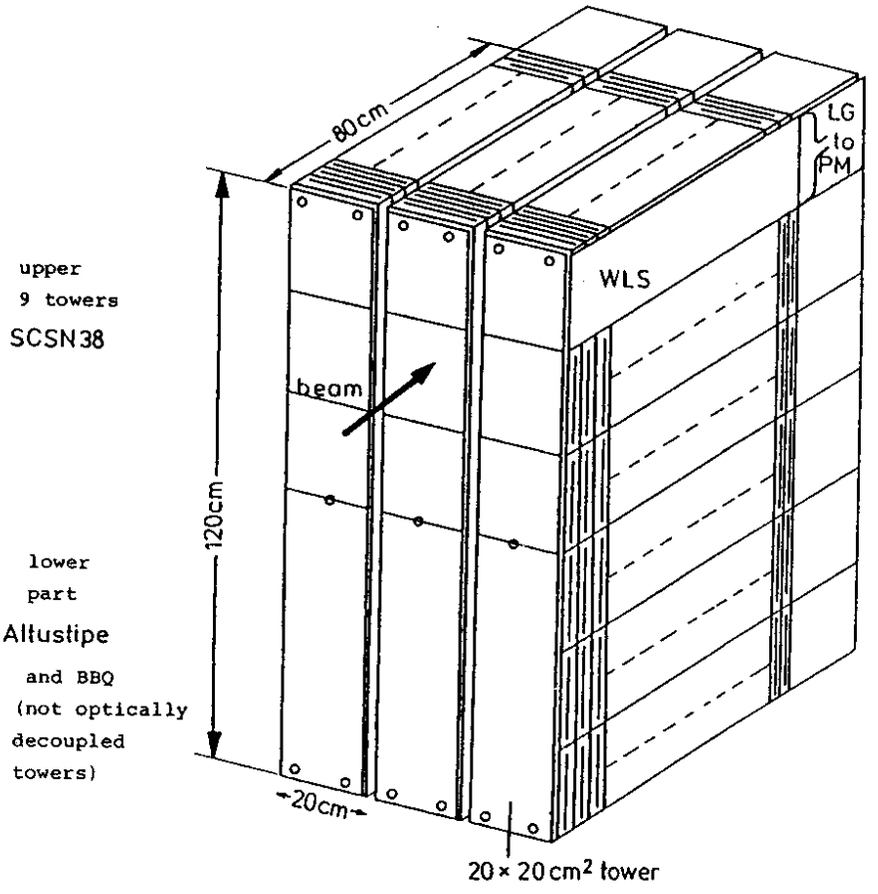


Fig. 35: The three modules of the test setup T35 are shown schematically. Only the experimental results from the upper 9 towers, equipped with the scintillator type SCSN 38 [57], are discussed here together with our M.C. predictions.

## II.2. Hadronic Energy Resolution

To investigate the hadronic energy resolution, a MC calculation has been performed for the T35 sampling calorimeter [11]. Fig. 35 gives an overview of the three test modules schematically. They were formed by 20 cm wide, 120 cm high and 3 mm thick DU plates interleaved with 2.5 mm thick plastic scintillator sheets. The upper half of the modules was equipped with SCSN 38 [58] and consisted of 9 optically decoupled towers. The optical readout was performed with 20 cm high and 80 cm

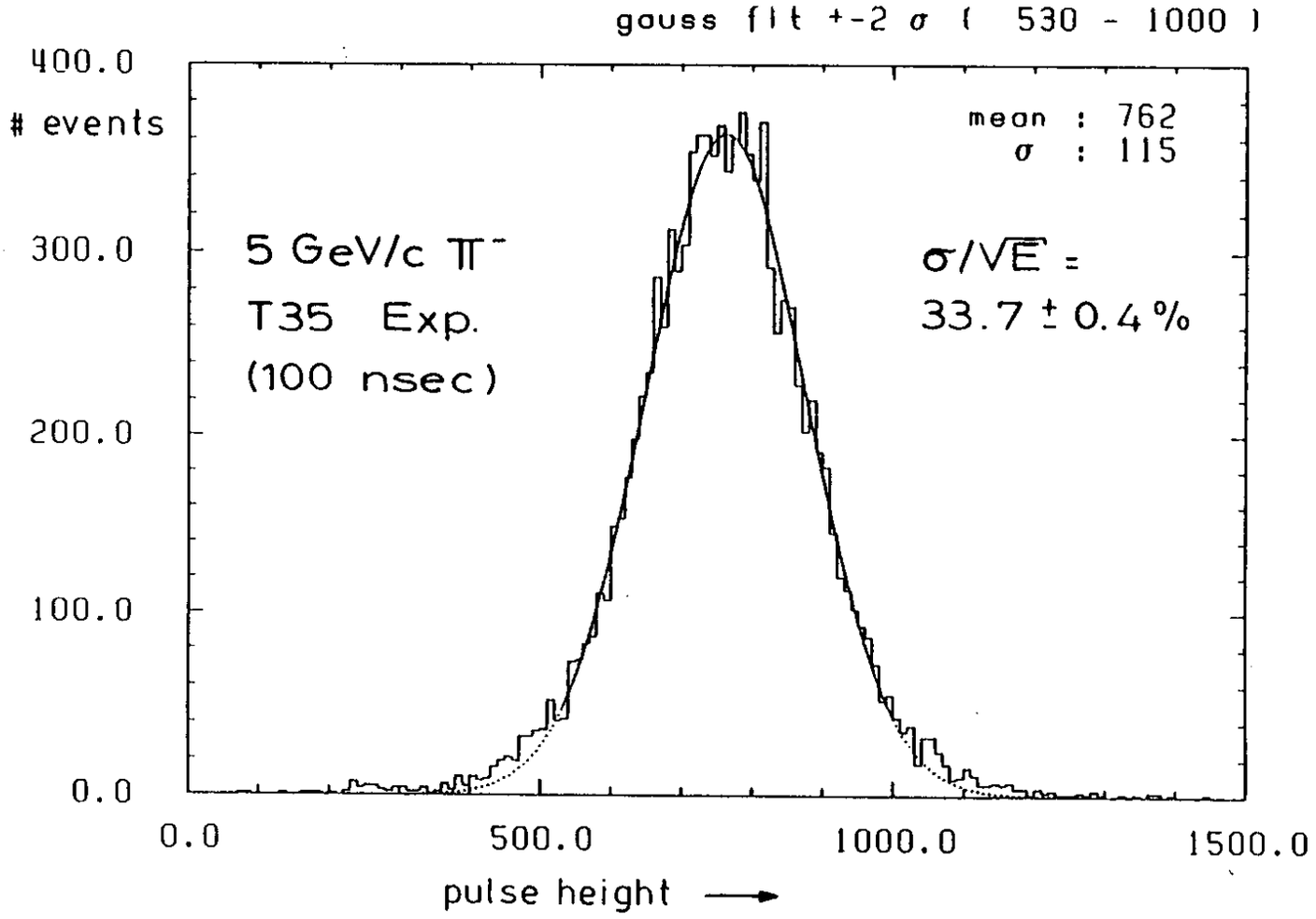


Fig. 36: Experimental pulse height distribution for hadrons ($\pi^-$) observed at 5 GeV/c (using 100 nsec gate time) for the T35 experiment [11]. For this gate time, an uncorrected e/h = 1.08 was obtained. The number quoted as 1.06 in [3] is actually the experimental value for 200 nsec.

long wave length shifter bars (WLS) followed by light guides (LG) and phototubes (PM) mounted on two sides of a calorimeter module. The total depth of a module was 4.2 absorption length and was readout as a whole without longitudinal subdivision.

The pulse height spectra measured at 5 GeV/c for 100 nsec gate time is given in Fig. 36. A Gaussian fit within $\pm 2\sigma$ yielded for the energy resolution $\sigma/E = 34\%/\sqrt{E(GeV)}$.

A detailed analysis and understanding of the effects of the fluctuations has to study, how the energy is distributed within single events. Although some aspects to this question have been discussed very recently [ 5,6 ], we study here how these fluctuations can be calculated without assumptions.

Fig. 37 shows schematically the various possibilities for distributing energy. Since for the kinetic energy of neutrons the normalized sampling fraction is rather high (see Fig. 32) if hydrogenous material is used as a detector, the main emphasize has to be the correct calculational treatment of this neutron component. By using the HERMES scheme for evaluating event-to-event fluctuations, one is able to arrive at predictions for absolute values of hadronic resolutions in sampling calorimeters. This can only be achieved by an enormous amount of CPU computer time (f.i. 11 h on an IBM 3081 for the analog MC neutron transport of the ≈ 150.000 neutrons created by 1000 incident $\pi^-$ source particles of 5 GeV) or the use of more powerful vector machines, like the CRAY-computer.

HERMES [50] is an improved MC simulation system for calorimeter design. Formerly a package CALOR [ 56], developed at ORNL, has been used mainly there. To entangle the physics of calorimeter resolution, which is governed by the fluctuations between the different shower components and also by the differences of the corresponding sampling fractions, a correlation plot (scatter plot) is used, see Fig. 38. A discussion of the main features of such a scatter plot has been already given in [3].

The mean energy of the projected spectrum from Fig. 38 is given by $(E_o \cdot mip) \cdot h_i/mip$. Thus $h_i$, which is a non-measurable quantity, can be evaluated. The result depends of course on the MC code used [9]. The scatter plot for the quantity $h_i$

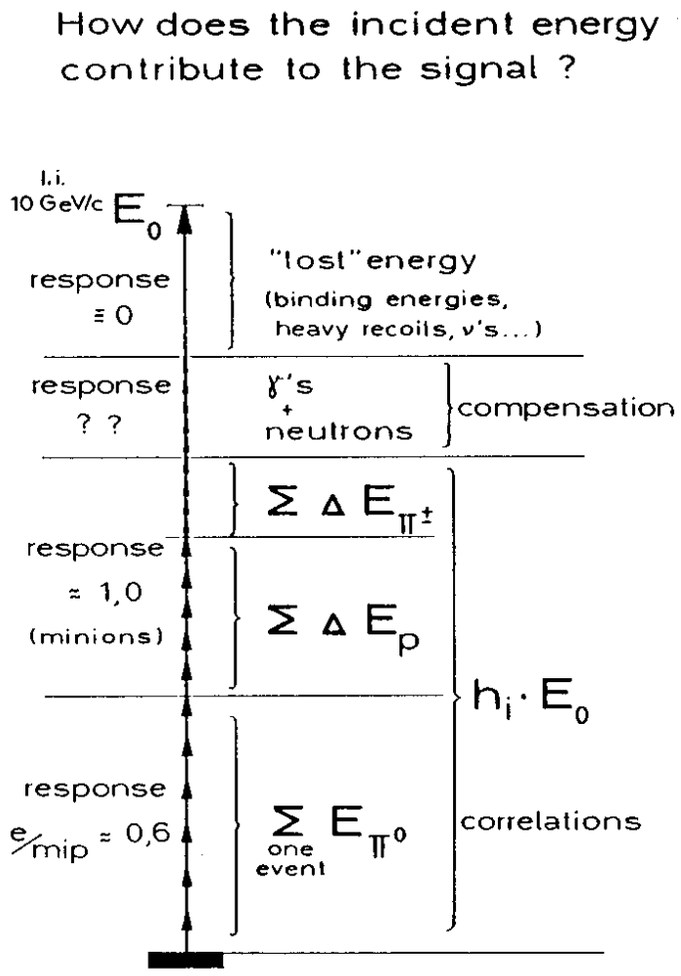


Fig. 37: The main components of event-to-event fluctuations in hadron sampling calorimetry. Each component exhibits its own characteristics and has its own sampling fraction.

offers the unique possibility to compare different codes basically. Up to this stage it is not necessary to consider all the neutron and gamma components.

In the scatter plot of Fig. 38, full compensation would be achieved if the events would group symmetrically around the line labelled C=1. If such a grouping around the C=1 line would be achieved, then the projection on to the pulse height axis would also have the smallest spread resulting in optimum resolution. Clearly one needs substantial contributions from

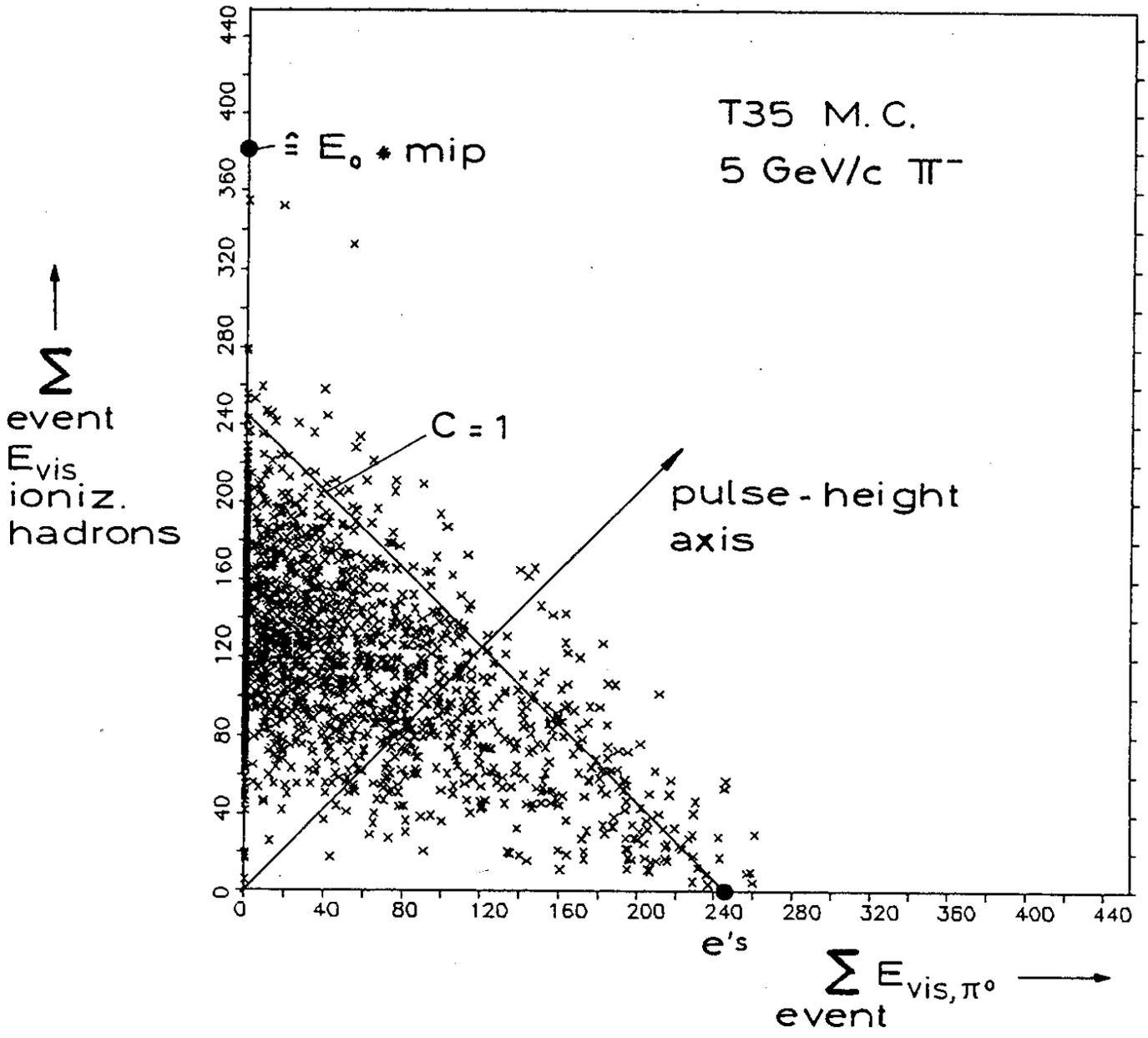


Fig. 38: An event-by-event (in total 2000) scatter plot of the sum of ionization energy of all the charged hadrons versus the sum of the π°-energy per event. About 60% contribution comes from the high energetic protons in the shower. The T35 sampling calorimeter [11] has been simulated with the HERMES code for incident 5 GeV/c $\pi^-$ particles. The line of equal response to electromagnetic as well as hadronic signals - full compensation - is indicated by C=1. From the center line of gravity, one concludes that without additional compensation signals the line C=1 can by far not be reached.

neutrons and gammas to achieve full compensation. Since one has to preserve the correlation on an event-to-event basis through several big MC codes, the task gets very time consuming.

One could think to speed up these calculations by introducing appropriate parameters from the mean value calculations, given in chap. I. But this is very dangerous, if one does not know, how these (mean) parameters influence the correlations; thus such a speed-up procedure will reduce the predictive power of the whole calculations.

As can be seen in Fig. 38, a correlated amount of energy has to be lost. The compensation is not necessary to be achieved for the energy $E_o \times$ mip, but only for $(E_o \times \text{mip}) \cdot \frac{e}{\text{mip}}$. This loss comes mostly from nuclear binding energy, which is necessary for the release of hadrons and/or light ions. Clearly the loss is a function of the number of hadrons produced.

The MC simulation for the test T35 has been performed without the wave length shifters, but took all 9 towers (20 cm × 20 cm) and the sampling structure (3 mm DU/2.5 mm SCSN 38 and 0.5 mm air gap) over the whole depth into account. To achieve a sufficient statistical accuracy, 2000 events of central incoming 5 GeV/c $\pi^-$ particles have been used. An updated HET-KFA version was run with the elastic scattering option for high energies switched on. Electromagnetic energy from $\pi^o$-decay and from nuclear reactions (including fission, nuclear deexcitation and n-capture, calculated with HETC or MORSE) were submitted as energy sources to EGS3, to be made visible in the detector layers (standard option calculation).

The amount of energy from the huge number ($\approx$ 300.000) of low energy neutrons (MORSE cut $E_n \leq 15$ MeV) are submitted to MORSE-KFA, which was operated in an analog fashion with a 100 nsec time-cut on the CRAY-XMP of the KFA-Jülich computing center.

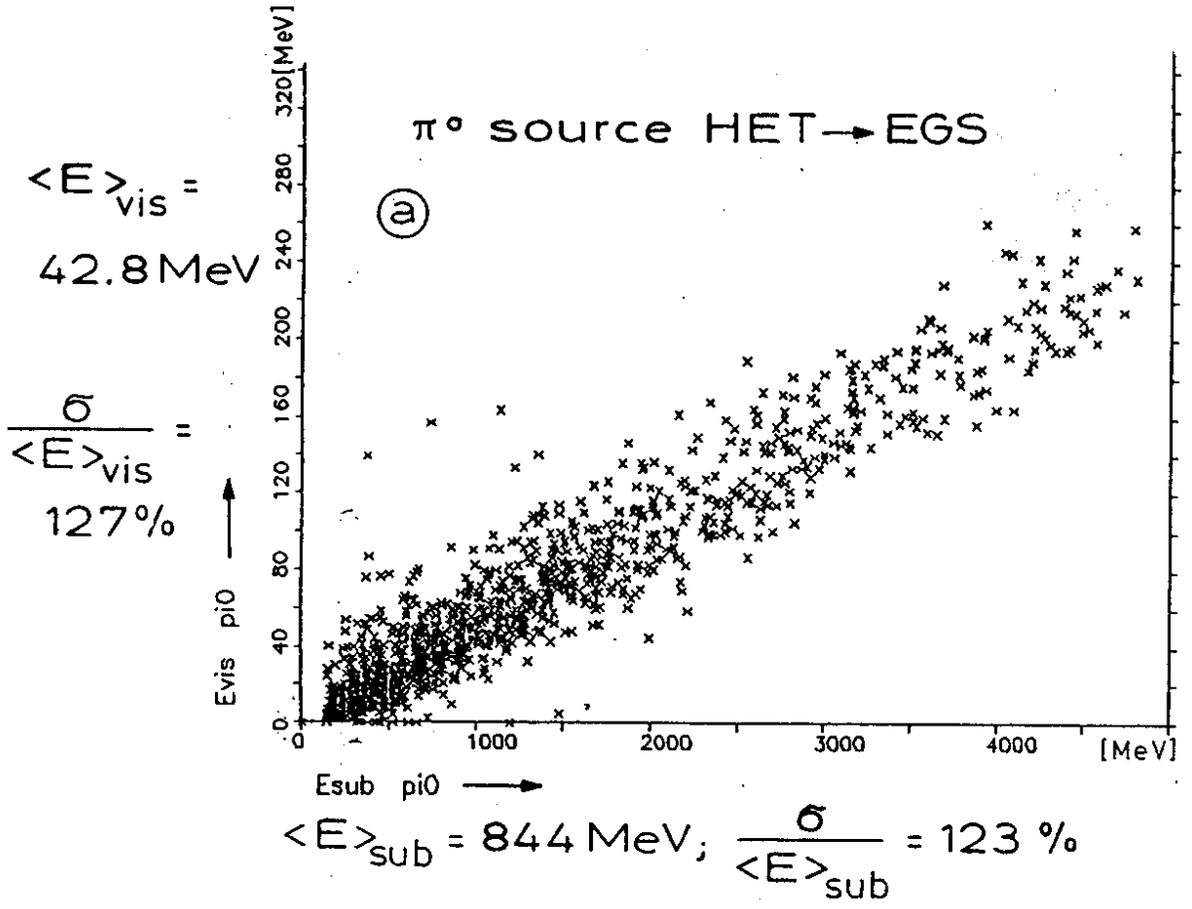


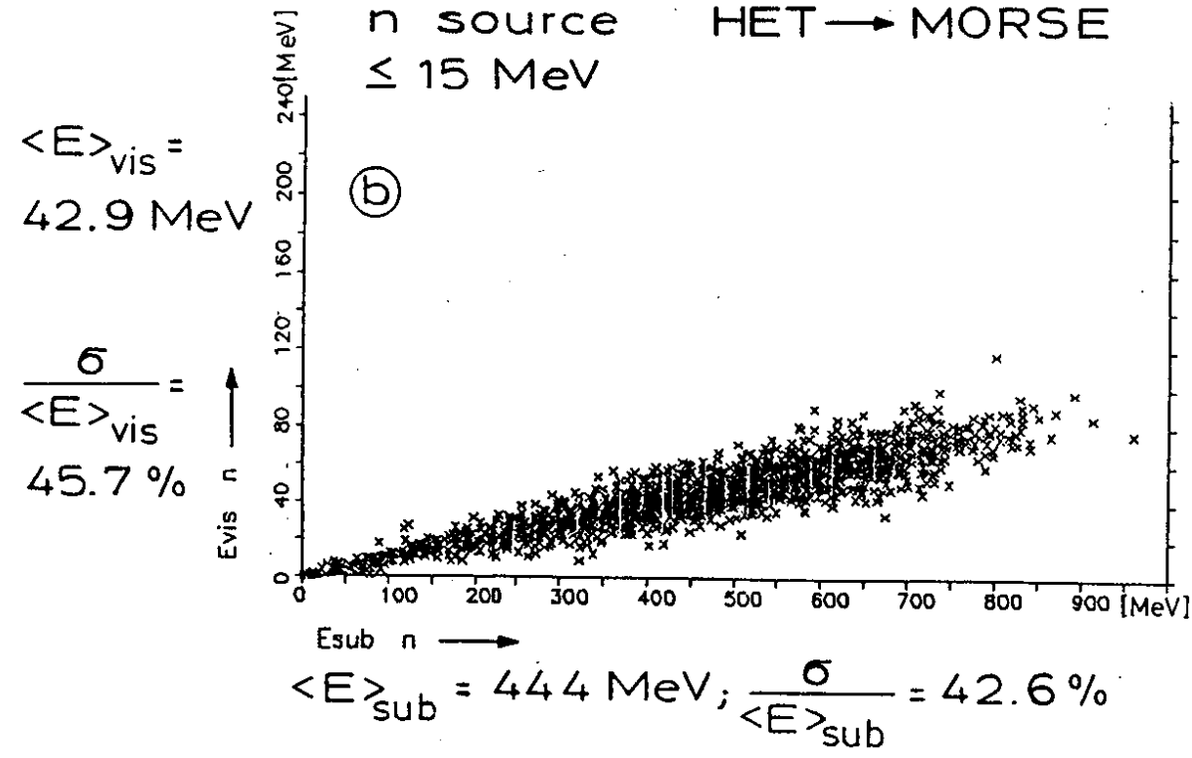


Fig. 39: Two of the source distributions which are produced by the HET-code for 5 GeV/c $\pi^-$ incident on the T35 setup. They are transformed by succeeding EGS (a) and MORSE (b) M.C. calculations. The normalized sampling fractions

still Fig. 39: (mip = 7.6%) can be evaluated: n/mip = 1.27 and e/mip = 0.66 from the ratios $\langle E \rangle_{vis}/\langle E \rangle_{sub}$. N/mip is practically equal to 1.23, calculated with the DYMO code, see Tab.5. E/mip (actually a $\pi^0$/mip from a spatial distributed $\pi^0$-source) is higher than 0.60 (from Tab. 5), obtained by using a simpler geometry with no air gaps and no tower structure.

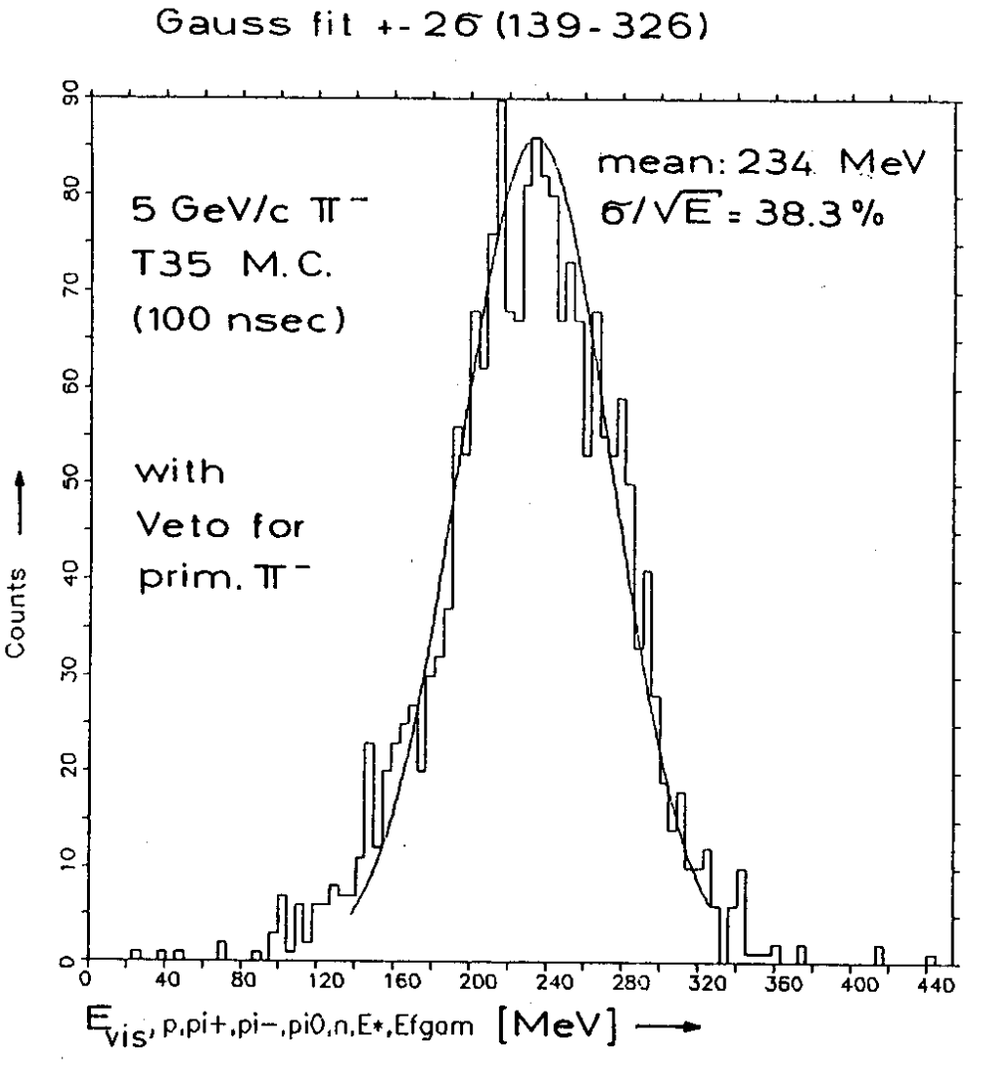


Fig. 40: The M.C. pulse height distribution for hadrons ($\pi^-$), simulated at 5 GeV/c for the setup of the T35 experiment. As in the experiment, punch through particles have been taken out with the help of a M.C. veto detector.

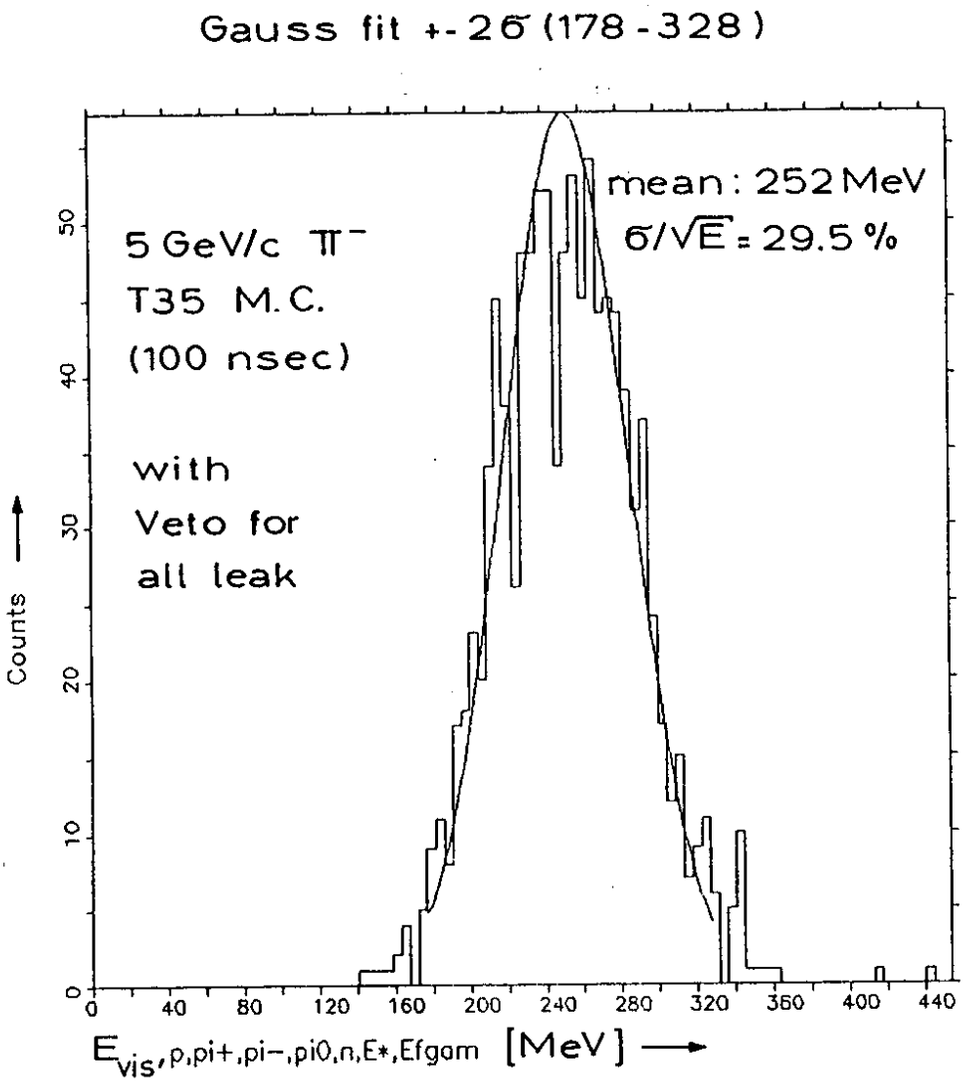


Fig. 41: The M.C. pulse height distribution for 5 GeV/c $\pi^-$, like Fig. 40, but extrapolated to full hermeticity. All M.C. histories belonging to leakage out of the calorimeter structure are taken out of the analysis by M.C. veto detectors, thus leaving only 1060 fully contained showers out of 2000. The resolution is thus drastically improved. This result is shown to illustrate the lowest limit of resolution at infinite geometry (hermetic case).

The event-by-event transformation of deposited energy to visible energy is shown in Fig. 39 for the $\pi^0$- and the n-source. One recognizes a clustering along a band, which reveals that a simple treatment of the visibility transformation by a reduction factor (this would result in a straight line in Fig. 39) is not adequate. One would neglect a certain degradation of the energy resolution by going from the deposited (submitted) distribution (43% for the n-source and 123% for the $\pi^0$-source) to the visible distribution (46% and 127%, respectively), as indicated in the figure.

The MC generated hadronic signal, including all visible contributions, is shown in Fig. 40. It should be compared with the experimental result from Fig. 36. Applying also a $\pm 2\sigma$ Gaussian fit, a resolution of $38\%/\sqrt{E}$ is obtained. Taking 248 MeV for the electromagnetic sampling fraction (which corresponds to e/mip = 0.65 and was taken from an independent EGS calculation using 5 GeV $e^-$ input particles), one finds for e/h = 248/234 = 1.06. These values are in good agreement with the experimental values ($34\%/\sqrt{E}$ and e/h = 1.08, still uncorrected in respect to possible read-out non-uniformities or leakage).

The result depends of course on the leakage out of the simulated calorimeter structure. The calculation gives: 6.6% longitudinal leak, 3.2% transversal (or side) leak and 3.0% leak out of the front, all given in % of the incoming energy. Since leakage can influence the resolution in a second analysis, all events in the simulation were discarded, for which the showers were not fully contained in the structure. This can be performed within HERMES by socalled MC veto detectors. The new result is shown in Fig. 41 and can be interpreted as an extrapolation of T35 to full hermeticity. The resolution has improved to $30\%/\sqrt{E}$

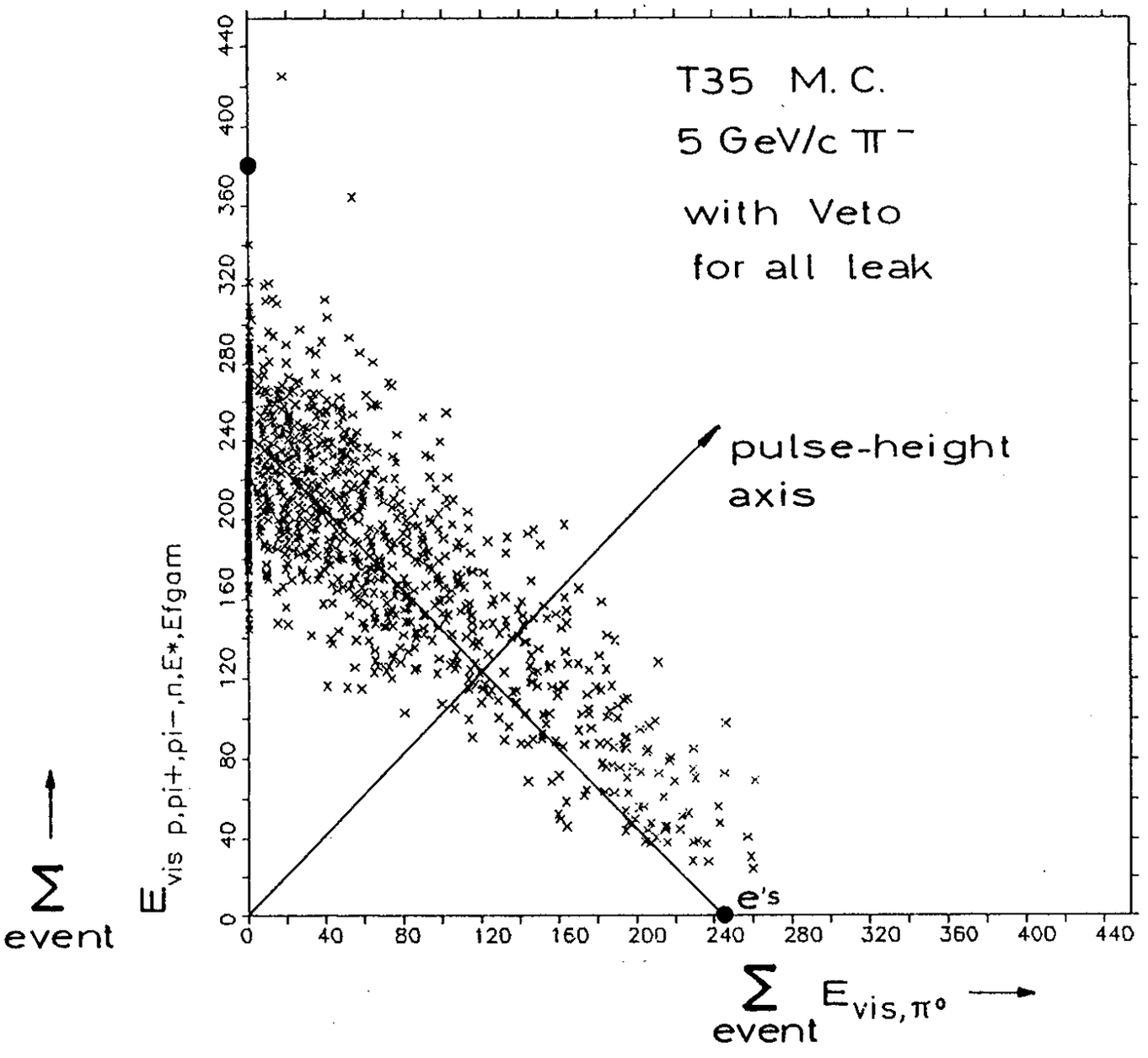


Fig. 42: All visible compensation signals from proton recoils and nuclear gamma sources are included in the correlation plot of Fig. 38 for the leakage corrected simulation. The projected spectrum, shown in Fig. 41, has the best possible resolution: the events group almost symmetrically around the axis for full compensation, C=1.

and the ratio e/h is now 0.984. Judging from the systematic and statistical uncertainties, inherent in the big MC codes used, the prediction is 1.00±0.02.

The scatter plot for the "hermetic" T35 calorimeter shows, as expected, that the broad distribution of events from Fig. 38 is contracting with due to compensation. This is shown clearly by the fact that the events now group around the line marked by C=1. As stated earlier, only then the projection onto the pulse-height axis has its smallest width, corresponding to optimal calorimeter resolution.

## Acknowledgements

We are very much indebted to R. Voss from CERN/DD to provide us with the MUDEX Monte Carlo code and to help us with many hints to convert the code from the CERN version (written for a CDC computer) to the DESY-IBM.

The large efforts of Ch. Reul and G. Sterzenbach (IRE, Kernforschungsanlage Jülich, FRG) in programming and testing the HERMES code are gratefully acknowledged.

We deeply thank G. Wolf for stimulating discussions and many helpful comments for the manuscript.

We are very much indebted to Mrs. M. Berghaus for carefully preparing all the drawings and typing the manuscript.

## References

[1] ZEUS Collaboration, Technical Proposal for the ZEUS Detector, DESY, Hamburg, March 1986

[2] Particle Properties Data Booklet, Particle Data Group, CERN, Tab. Atomic and Nuclear Properties of Materials

[3] H. Brückmann, U. Behrens and B. Anders, Hadron Sampling Calorimetry - A Puzzle of Physics -, Nucl. Instr. & Meth. Phys. Res., to be published, and DESY 86-155, Hamburg, Dec. 1986

[4] R.J. Cashmore, R.C.E. Devenish, P. Grossmann and M.L. Retter, Nucl. Instr. & Meth. Phys. Res. A242(1985)42

[5] R. Wigmans, On the Energy Resolution of Uranium and Other Hadron Calorimeters, CERN/EF 86-18, Geneva, Sept. 86

[6] H. Fesefeldt, The E/H-Ratio and Energy Resolution of Hadron Calorimeters, RWTH Aachen, PITHA 86/05

[7] H. Brückmann, Proc. Workshop on Compensated Calorimetry, Pasadena, Sept. 1985, CALT-68-1305

[8] C.W. Fabjan, Calorimetry in High-Energy Physics, CERN-EP/85-54, Geneva, April 1985

[9] B. Anders, U. Brandenburg, H. Brückmann and P. Schröder, Neutronic Calculations on Hadronic Sampling Calorimeters Concerning e/h-Ratios, ZEUS Int. Note (1987), in preparation

[10] W. Lohmann, R. Kopp and R. Voss, Energy Loss of Muons in the Energy Range 1-10000 GeV, CERN 85-03, Geneva, 1985

[11] B. Anders et al., ZEUS Collab., DESY-Report 86-105, Hamburg, Sept. 1986

[12] W. Lohmann, R. Kopp and R. Voss, MUDEX - Program Description, CERN, private communication

[13] H.J. Bhabha, Proc. Roy. Soc. A164(1938)257

[14] A.A. Petrukhin and V.V. Shestakov, Can. J. Phys. 46(1968)S377

[15] R.P. Kokoulin and A.A. Petrukhin, Acta Phys. Hung. 29, Suppl. 4(1970)277; Proc. 12th Int. Conf. on Cosmic Rays, Hobart, 1971, Vol. 6, p. A2436

[16] C.J. Crannell, H. Crannell, C.R. Gillespie, K. Pinkau and R.R. Whitney, Phys. Rev. 182(1969)1435 and 1441

[17] K. Pinkau, Phys. Rev. B139(1965)1548

[18] H.L. Beck, Nucl. Instr. & Meth. 91(1971)525

[19] W. Flauger, Nucl. Instr. & Meth. A241(1985)72

[20] A.J. Lankford, Thesis Geneva 1978, CERN Internal Report EP-78-3

[21] T. Kondo, H. Iwasaki, Y. Watanabe and T. Yamanaka, 1984 Summer Study on the Design and Utilization of the Super Conducting Super Collider, Snowmass, Colorado, June 1984

[22] T.E. Burlin, Cavity-Chamber Theory in Radiation Dosimetry, 2nd Ed., Vol. 1, Academic Press, 1968

[23] F.H. Attix, Chap. 8 and 10 in: Introduction to Radiological Physics and Radiation Dosimetry, John Wiley & Sons, 1986

[24] J. Brau, Proc. Workshop on Compensated Calorimetry, Pasadena, Sept. 1985, CALT-68-1305

[25] B. Anders, H. Brückmann, $\gamma$-Efficiencies in Calorimeter Stacks, ZEUS-Note, to be published and Jahresbericht I. Institut für Experimentalphysik 1984/85: The Contribution of Prompt Fission Gammas to the Compensation of Uranium/LA Hadron Calorimeters, University of Hamburg, FRG, p.65

[26] W.W. Engle, Jr., A Users Manual for ANISN, ORNL-CCC254, June 1973

[27] Y.S. Horowitz, M. Moscovitch, J.M. Mack, H. Hsu and E. Kearsley, Nucl. Sci. and Eng. 94(1986)233

[28] D.W.O. Rogers, Nucl. Instr. & Meth. 199(1982)531; D.W.O. Rogers, Nucl. Instr. & Meth. A227(1984)535

[29] A.F. Bielajew, D.W.O. Rogers and A.E. Nahum, Phys. Med. Biol. 30(1985)419 and 429

[30] W.R. Nelson, H. Hirayama and D.W.O. Rogers, The EGS4 Code System, SLAC-Report-265, Dec. 1985

[31] A.F. Bialejew and D.W.O. Rogers, Nucl. Instr. & Meth. Phys. Res. B18(1987)165

[32] T.W. Armstrong, P. Cloth, D. Filges and R.D. Neef, An Investigation of Fission Models for High-Energy Radiation Transport Calculations, KFA Jülich report JUEL-1859, Jülich, July 1983, and Nucl. Instr & Meth. Phys. Res. 222(1984)540

[33] T.W. Armstrong and K.C. Chandler, HETC, Monte Carlo High-Energy Nucleon Meson Transport Code, ORNL-4744 (1972) and Nucl. Sci. and Eng. 49(1972)110;
T.A. Gabriel, The High-Energy Transport Code HETC, ORNL/TM-9727, Sept. 1985;
P. Cloth, D. Filges, G. Sterzenbach, T.W. Armstrong and B.L. Colborn, The KFA-Version of the High-Energy Transport Code HETC and the Generalized Evaluation Code SIMPEL, KFA-Report JUEL-Spez-196, Jülich, March 1983

[34] T.A. Gabriel, R.T. Santoro and J. Barish, ORNL-TN-3615, Oak Ridge, 1971

[35] V.S. Barashenkov and V.D. Toneyev, Vzaimodeystviya Vysokoenergeticheskikh Chastits i Atomnykh Yader 5 Yadrami, Moscow (1972)

[36] H.W. Bertini, A.H. Culkowski, O.W. Hermann, N.B. Gove and M.P. Guthrie, Phys. Rev. C17(1978)1382

[37] C. Leroy, Y. Sirois and R. Wigmans, An Experimental Study of the Contribution of Nuclear Fission to the Signal of Uranium Hadron Calorimeters, CERN-EP/86-66, Geneva, June 1986

[38] H. Fesefeldt, The Simulation of Hadronic Showers - Physics and Applications - (GHEISHA), RWTH Aachen, Report PITHA 85/02, Aachen (FRG), 1985

[39] H. Fesefeldt, Proc. Workshop on Compensated Calorimetry, Pasadena, Sept. 1985, CALT-68-1305

[40] P.A. Aarnio, A. Fasso, H.-J. Moehring, J. Ranft and G.R. Stevenson, FLUKA86 Users Guide, CERN TIS-RP/168, Geneva, Jan. 1986

[41] T.W. Armstrong, P. Cloth, D. Filges and R.D. Neef, Theoretical Target Physics Studies for the SNQ Spallation Neutron Source, Report JUEL-SPEZ-120, Jülich, July 1981

[42] P. Cloth, D. Filges, C. Reul, G. Sterzenbach, B. Anders, U. Behrens and H. Brückmann, Monte Carlo Simulation of TEST-35 with HERMES, JUEL-report 1987, Jülich (FRG), to be published

[43] U. Brandenburg, Diploma Thesis, Hamburg 1986;
B. Anders, R. Beckmann, U. Brandenburg and H. Brückmann, in: Jahresbericht I. Institut für Experimentalphysik 1984/85, Universität Hamburg, FRG, p. 67

[44] M.B. Emmett, The MORSE Monte Carlo Radiation Transport Code System, ORNL-4972/R1, Oak Ridge, Feb. 1983

[45] R. Kinsey, Data Formates and Procedures for the Evaluated Nuclear Data File ENDF/B-IV, BNL-NCS-17541, Brookhaven, 1979

[46] RSIC Data Library Collection, FEWG1 (DLC31), ORNL/TM-4840, Oak Ridge, 1977

[47] RSIC Data Library Collection, EPR (DLC37), ORNL/TM-5249, Oak Ridge, 1979

[48] S. Pearlstein, Meeting of the Medium Energy Nuclear Data Working Group, Report BNL-NCS-38404, Brookhaven, USA, May 1986

[49] A.E. Profio, Experimental Reactor Physics, J. Wiley & Sons

[50] P. Cloth, D. Filges, Ch. Reul, G. Sterzenbach, B. Anders and H. Brückmann, HERMES-Release, KFA-Report, to be published

[51] J.B. Birks, Scintillation Counters (McGraw Hill, New York, 1953)

[52] R. Beckmann, U. Brandenburg, H. Brückmann, J.M. Hirschberg, V. Stieber and K. Wick, Nucl. Instr. & Meth. Phys. Res., 1987, to be published

[53] E.S. Troubetzkoy, Phys. Rev. 122(1961)212;
B. Basarragtscha, D. Hermsdorf and D. Seeliger,
Nucl. Sci. Eng. 83(1983)294

[54] R. Klanner, Test Program for the ZEUS Calorimeter.
Proc. Int. Conf. on Advance in Exp. Methods in Coll. Beam Physics, Stanford, Lin. Acc. Center, 9-13 March, 1987

[55] M.G. Catanesi et al., DESY 87-027, Hamburg, April 1987

[56] J. Brau, H.J. Hargis, T.A. Gabriel and B.L. Bishop,
ORNL/TM-9486, Oak Ridge, Jan. 1985 and
Nucl. Instr. & Meth. Phys. Res. A238(1985)489;
T.A. Gabriel et al., Nucl. Instr. & Meth. 195(1982)461
F.S. Alsmiller, T.A. Gabriel and R.G. Alsmiller, Jr.,
ORNL/TM-9153, Oak Ridge, Aug. 1984;
T.A. Gabriel et al., ORNL/TM-9270, Oak Ridge, Jan. 1985;
T.A. Gabriel et al., IEEE Trans. Nucl. Sci. NS-32(1),
Feb. 1985;
T.A. Gabriel, Proc. Workshop on Compensated Calorimetry,
Pasadena, Sept. 1985, CALT-68-1305

[57] Product of Kyowa-Gas, Japan

[58] Product of Nuclear Enterprises, England